Reflection Symmetry Detection in Images : Application to Photography Analysis

Mohamed Elsayed Elawady

▶ **To cite this version:**

Mohamed Elsayed Elawady. Reflection Symmetry Detection in Images : Application to Photography Analysis. Optics [physics.optics]. Université de Lyon, 2019. English. NNT : 2019LYSES006 . tel-02457900

HAL Id: tel-02457900
https://theses.hal.science/tel-02457900

Submitted on 28 Jan 2020

HAL is a multi-disciplinary open access archive for the deposit and dissemination of scientific research documents, whether they are published or not. The documents may come from teaching and research institutions in France or abroad, or from public or private research centers.

L'archive ouverte pluridisciplinaire **HAL**, est destinée au dépôt et à la diffusion de documents scientifiques de niveau recherche, publiés ou non, émanant des établissements d'enseignement et de recherche français ou étrangers, des laboratoires publics ou privés.

N° d'ordre NNT : 2019LYSES006

THESE de DOCTORAT DE L'UNIVERSITE DE LYON

opérée au sein de

Laboratoire Hubert Curien

Ecole Doctorale ED SIS 488

(**Ecole Doctorale Science, Ingénierie et Santé**)

Spécialité de doctorat : Image Vision Optique

Discipline : Computer Vision

Soutenue publiquement le 29/03/2019, par

Mohamed ELSAYED ELAWADY

Reflection Symmetry Detection in Images : Application to Photography Analysis

---

Devant le jury composé de :

M. DEMONCEAUX, Cédric	PU	Université de Bourgogne	Rapporteur
M. LAMBERT, Patrick	PU	Université Savoie Mont Blanc	Rapporteur
M. ROSENBERGER, Christophe	PU	ENSICAEN- GREYC	Examinateur
Mme. BARAT, Cécile	Dr.	ST Microelectronics	Co-encadrante
M. COLANTONI, Philippe	MCF	Université Jean-Monnet	Co-encadrant
M. ALATA, Olivier	PU	Université Jean-Monnet	Co-directeur
M. DUCOTTET, Christophe	PU	Université Jean-Monnet	Directeur de thèse

Acknowledgements

It has been a scientific adventure to finish PhD education in four years, to achieve one of the main life goals since childhood by contributing an useful research to world community. During these years, i gained day-by-day educational and academic experiences through an international environment.

First of all, I would like to thank my advisors. Christophe Ducottet, who helped me patiently with every PhD step and kept his door open for any questions. Olivier Alata, who taught me how to be a good researcher and brainstormed different research ideas through connecting between the mathematical concepts and the programming experiments in very clever way. Cecile Barat, who managed easily for me to find the starting points of different research topics. Philippe Colantoni, who guided me to find the link between computer vision and art fields and provided me generously the historical museum databases. Without these 4 advisors, the thesis will never reach the light to be published.

In Hubert Curien laboratory, I would like to thank all my colleagues and researchers in Image Science and Computer Vision group (Rada Deeb, Mohammad Nawaf, Rahul Mourya, Juan Martinez, Carlos Arango, Md Abul Hasnat, Alain Tremeau, Eric Dinet, Corinne Fournier). Also my friends from other groups (Bobin Varghese, El Mehdi Benhani, Hady Elsahar, Nipun Sharma, Leonor Becerra, Imene Reghioua, Ayoub Ladaci, Valentina Zantedeschi, Kamal Singh, Mohamad Sater, Bilal Benarabi, Jose Gimenez, Dennis Diefenbach, Adriana Morana, Anil Goyal, Cuauhtemoc Mancillas, Joyce Ibrahim, Serena Rizzolo, Anton Rudenko, Ciro D'Amico, Atef Dorai).

Personally, many thanks to my family (Mum, Dad, Ahmed, Farah, Ibtihal), and thanks to my great friends from Egypt and around the world (Jean Christophe, Shabayek, Ibrahim, Luis, Jessica, Noora, Fede, Maher, Arafat, Mostafa, Lili, Shaifali, Abdelkhalik, Jilliam, Dhouha, Laura, Alex, Victor, Viktor, Diana, Zahy, Arif, Dounia, Alberto, Adel, Eldaly, Shady, Hema, Khalid, Hossam, Omar, Elsese, Claudia, Emad). I dedicate this thesis to them.

Abstract

Symmetry is a fundamental principle of the visual perception to feel the equally distributed weights within foreground objects inside an image. It is used as a significant visual feature through various computer vision applications (i.e. object detection and segmentation), plus as an important composition measure in art domain (i.e. aesthetic analysis). The development of symmetry detection has been improved rapidly since last century. In this thesis, we mainly aim to propose new approaches to detect reflection symmetry inside real-world images in a global scale. In particular, our main contributions concern feature extraction and global representation of symmetry axes. First, we propose a novel approach that detects global salient edges inside an image using Log-Gabor filter banks, and defines symmetry oriented similarity through textural and color around these edges. This method wins a recent symmetry competition worldwide in single and multiple cases. Second, we introduce a weighted kernel density estimator to represent linear and directional symmetrical candidates in a continuous way, then propose a joint Gaussian-vonMises distance inside the mean-shift algorithm, to select the relevant symmetry axis candidates along side with their symmetrical densities. In addition, we introduce a new challenging dataset of single symmetry axes inside artistic photographies extracted from the large-scale Aesthetic Visual Analysis (AVA) dataset. The proposed contributions obtain superior results against state-of-art algorithms among all public datasets, especially multiple cases in a global scale. We conclude that the spatial and context information of each candidate axis inside an image can be used as a local or global symmetry measure for further image analysis and scene understanding purposes.

Résumé

La symétrie est une propriété géométrique importante en perception visuelle qui traduit notre perception des correspondances entre les différents objets ou formes présents dans une scène. Elle est utilisée comme élément caractéristique dans de nombreuses applications de la vision par ordinateur (comme par exemple la détection, la segmentation ou la reconnaissance d'objets) mais également comme une caractéristique formelle en sciences de l'art (ou en analyse esthétique). D'importants progrès ont été réalisés ces dernières décennies pour la détection de la symétrie dans les images mais il reste encore de nombreux verrous à lever. Dans cette thèse, nous nous intéressons à la détection des symétries de réflexion, dans des images réelles, à l'échelle globale. Nos principales contributions concernent les étapes d'extraction de caractéristiques et de représentation globale des axes de symétrie. Nous proposons d'abord une nouvelle méthode d'extraction de segments de contours à l'aide de bancs de filtres de Gabor logarithmiques et une mesure de symétrie inter-segments basée sur des caractéristiques locales de forme, de texture et de couleur. Cette méthode a remporté la première place à la dernière compétition internationale de symétrie pour la détection mono- et multi-axes. Notre deuxième contribution concerne une nouvelle méthode de représentation des axes de symétrie dans un espace linéaire-directionnel. Les propriétés de symétrie sont représentées sous la forme d'une densité de probabilité qui peut être estimée, de manière non-paramétrique, par une méthode à noyaux basée sur la distribution de Von Mises-Fisher. Nous montrons que la détection des axes dominants peut ensuite être réalisée à partir d'un algorithme de type "mean-shift" associé à une distance adaptée. Nous introduisons également une nouvelle base d'images pour la détection de symétrie mono-axe dans des photographies professionnelles issue de la base à grande échelle AVA (Aestetic Visual Analysis). Nos différentes contributions obtiennent des résultats meilleurs que les algorithmes de l'état de l'art, évalués sur toutes les bases disponibles publiquement, spécialement dans le cas multi-axes. Nous concluons que les propriétés de symétrie peuvent être utilisées comme des caractéristiques visuelles de niveau sémantique intermédiaire pour l'analyse et la compréhension de photographies.

Contents

Table des matières

List of Figures

List of Tables

List of Algorithms

Abbreviations

PR Precision Evaluation Measure

RC Recall Evaluation Measure

SIFT Scale Invariant Feature Transform

vMF von Mises–Fisher Distribution

vM von Mises Distribution

GvM Mixuture of Gaussian von Mises Distributions

KDE Kernel Density Estimation

GvM-KDE Kernel Density Estimation using Gaussian kernel for linear data and von Mises kernel for directional data

MS Mean-Shift Technique

NMS Non-Maximal Supression Method

SC Symmetry Candidate

GT Ground Truth

TP True Positive

FP False Positive

FN False Negative

HSV Color Model of Hue, Saturation and Value

MIL Multiple Instance Learning

KNN K-Nearest Neighbors Algorithm

DOPM Diagonals of Orthogonal Projection Matrices

LD Linear-Directional Data

DC Direct Current Component

AVA Aesthetic Visual Analysis

CNN Convolutional Neural Networks

RANSAC Random Sample Consensus Method

MSER Maximally Stable Extremal Regions Detector

Pb Probability-of-Boundary Detector

FT 2D Fourier Transform

Symbols

$I(.)$ Input Image in Spatial Domain

$\ddot{I}(.)$ Input Image in Fourier Domain

$\psi(.)$ Mother Wavelet

$\psi_{s,o}(.)$ Gabor Wavelet Family of Scale s and Orientation o

$\ddot{G}_{s,o}(.)$ Log-Gabor Wavelet Family of Scale s and Orientation o in Fourier Domain

$I_{s,o}(.)$ Wavelet Response on Input Image $I(.)$

$J(.)$ Amplitude of Maximum Wavelet Response $I_{s,o}(.)$ across Scales and Orientations

$\phi(.)$ Orientation of Maximum Wavelet Response $I_{s,o}(.)$ across Scales and Orientations

$S_E(.)$ Mirror Symmetry Coefficient based on Edge Information

$S_T(.)$ Similarity Measure between Textural Histograms

$S_C(.)$ Similarity Measure between Color Histograms

$R(.)$ Reflection Matrix

$\Omega(.)$ Clockwise Rotation Matrix

$G_\varepsilon(.)$ Gaussian Kernel

$G_\vartheta(.)$ von-Mises Fisher Kernel

$A(\kappa)$ Normalization Constant of von-Mises Fisher Kernel

$B(.)$ Modified Bessel Function

$B'(.)$ First Derivative of Modified Bessel Function $B(0,\kappa)$

$U(.)$ Transfer Function of Low-pass Butterworth Filter

$d(.)$ Joint Distance Function

$h(.)$ Textural Histogram

$g(.)$ Color Histogram in HSV Color Space

$f(.)$ Voting Histogram using Hough Scheme

$f_{\varepsilon,\vartheta}(.)$ Voting Histogram using KDE

$\hat{f}_{\varepsilon,\vartheta}(.)$ Weighted Voting Histogram using KDE

W Width of Input Image $I(.)$

H Height of Input Image $I(.)$

S Number of Wavelet Scales

O Number of Wavelet Orientations

P Number of Feature Points

N Number of Feature Pairs

L Number of Bins of Each Textural Histogram

C Number of Bins of Each Color Histogram

D_i Non-interleaved Cell of Feature Point p^i along a Regular 2D Grid

D_i^* Non-interleaved Cell centered by Feature Point p^i

κ Concentration Parameter of von-Mises Fisher Kernel

σ Bandwidth Parameter of Gaussian Kernel

s Wavelet Scale

o Wavelet Orientation Index

α_o Wavelet Orientation using Gabor Filter

β_o Wavelet Orientation using Log-Gabor Filter

μ Radial Component of Log-Gabor Wavelet in Log-polar Coordinate System

α Angular Component of Log-Gabor Wavelet in Log-polar Coordinate System

μ_s Radial Frequency Center of Log-Gabor Wavelet in Log-polar Coordinate System

α_o Angular Frequency Center of Log-Gabor Wavelet in Log-polar Coordinate System

λ_μ Radial Bandwidth of Log-Gabor Wavelet

λ_α Angular Bandwidth of Log-Gabor Wavelet

ω_n Symmetry Weight

c Image Origin

p^i Feature Point

q_n Feature Pair

τ^i Direction of Feature Point p^i

ρ_n Displacement of Feature Pair q_n

θ_n Orientation of Feature Pair q_n

$\boldsymbol{\theta}_n$ Orientation of Feature Pair q_n in Unit Vector Form

x Continuous Displacement Term

y Continuous Orientation Term

$\mathbf{y}$ Continuous Orientation Term in Unit Vector Form

$\bar{x}$ Discretized Displacement Term

$\bar{y}$ Discretized Orientation Term

$\tilde{x}$ Merged Displacement Term

$\tilde{y}$ Merged Orientation Term

Δ_C Convergence Threshold for MS Algorithm

Δ_M Merging Threshold for MS Algorithm

γ Angular Constraint for Evaluation Metrics

ζ Distance Constraint for Evaluation Metrics

Chapter 1

Introduction

1.1 Background

1.1.1 What is symmetry?

Symmetry is one of the significant visual properties inside an image plane, to identify the geometrically balanced structures through real-world objects. In Mathematics [99], an object is defined of being symmetric if this object can be divided into two or more similar pieces that are arranged in an organized way. In modern photography [168], It is also defined as the process of organizing image-parts that balances the general viewpoint of the human mind regarding an image. As in figure 1.1, the interior design of Westminster Abbey has shown different symmetries inside this artistic photo (the circular details in the ceilings, the mirror organization of the glass windows, and finally the centered column).

1.1.2 Why symmetry?

In the past years, art scientists manually interpret paintings and photographs for cultural heritage projects. We aim to help these scientists to use a art principle (balance) based on a visual cue (symmetry) through an automated detection system, through finding a geometrical correlation between low-level primitives and symmetry cues, in order to refine the understanding of semantic details inside an artistic image.

1.1.3 Types of symmetry

The contextual understanding of symmetry can be categorized, as shown in figures (1.2, 1.4), into the following:

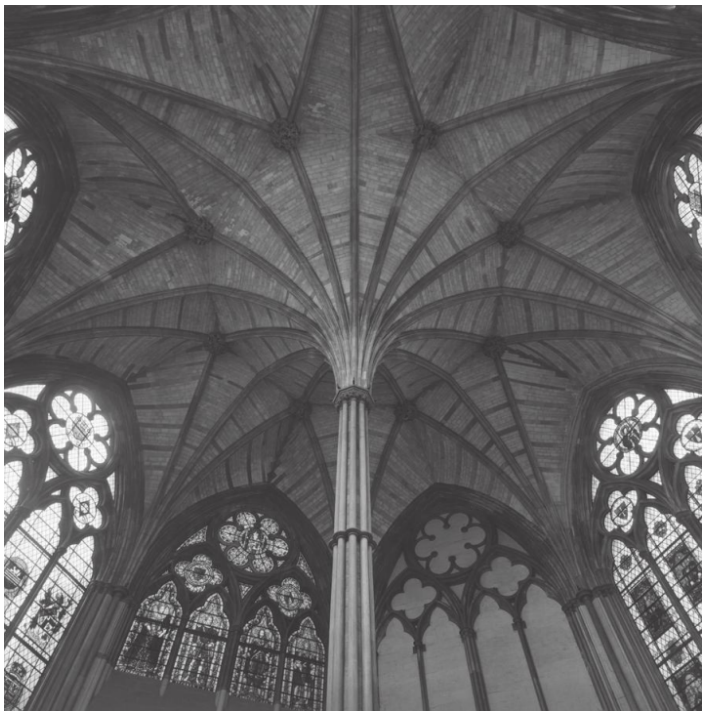

Figure 1.1 Symmetry example of ceiling view in Westminster Abbey, UK. Source: [51].

— Reflection: (aka mirror, or bilateral) Balanced region where local patterns are nearly matching on each side of a straight axis. Sub-figure 1.2a shows a focused object (Eiffel tower in Paris) in the middle with dark street and blueish sky views. The steel structure of the middle object forms symmetric shapes outputting a single reflection example. Another sub-figure 1.2b presented two focused object (monkey and dog toys) with clear background of indoor scene. The correct multiple symmetries define the intra-structural details of both toys.
— Rotation: Similar objects are radially recognized around an angular center. Sub-figure 1.2c describes the radial details of the entertainment wheel to result a rotation symmetry respect to the wheel center.
— Translation: Focused details are visually repeated within linear fashion. In other words, the same objects appear more than once in different locations within the same image. Sub-figures 1.2d,e demonstrate the repetition of the street stones and the building windows along x-axis, y-axis or both coordinates.
— Skeleton: (aka medial) Inner curved axes are locally explored by thinning the objects. Sub-figure 1.2f highlights the intra-object connections of medial centers inside different scene objects (tree, stones).

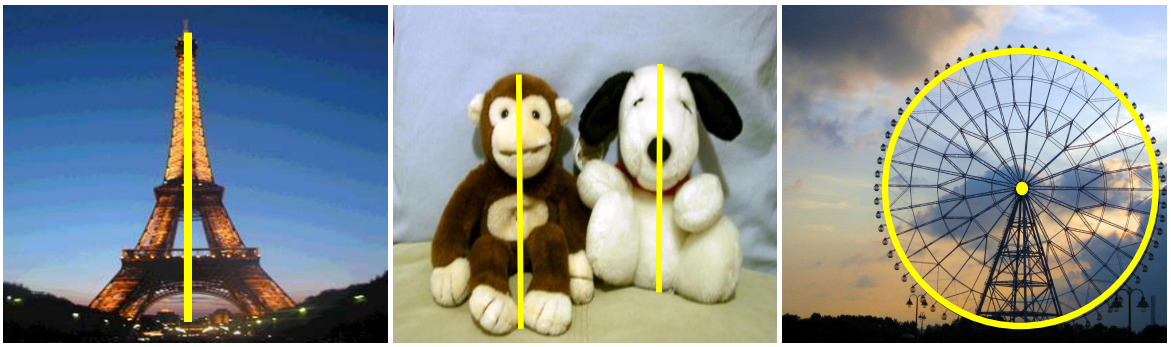

(a) Reflection - Single (b) Reflection - Multiple (c) Rotation

(d) Translation - Frieze (e) Translation - Wallpaper (f) Medial

Figure 1.2 Real-world examples with primitive symmetries (highlighted in yellow color) in 2D image coordinates from published symmetry datasets. Source: (a-e) [95], (f) [152]

.

A book about symmetry (published by Liu et al. [97] in 2010) stated the first definitions of global and local symmetries. As shown in fig 1.3, the global symmetry can be determined through contribution of the main basic elements (i.e. points, lines, etc . . .) inside different scene shapes. This kind of symmetry can be modeled as mirror straight lines with a lot of efforts to spot such these lines in terms of time. Besides that, these lines are sensitive to any changes in shape transformations. While the local symmetry can be locally supported by object sub-parts or shape contours. It can express not only by reflection symmetrical segments, but also with skeleton and rotational symmetries.

This work focuses on detecting global reflection symmetries (as in figure 1.5) inside an image plane. Note that we consider real world images with approximate symmetry. For example, pattern located on both sides of the axis may not be perfectly symmetric but must be similar enough. Furthermore, we deal with global symmetry which means that a significant area around the symmetry axis must be concerned by the symmetry (see section 3.2). Two different situations will finally be considered: the single and the multiple case. In the single

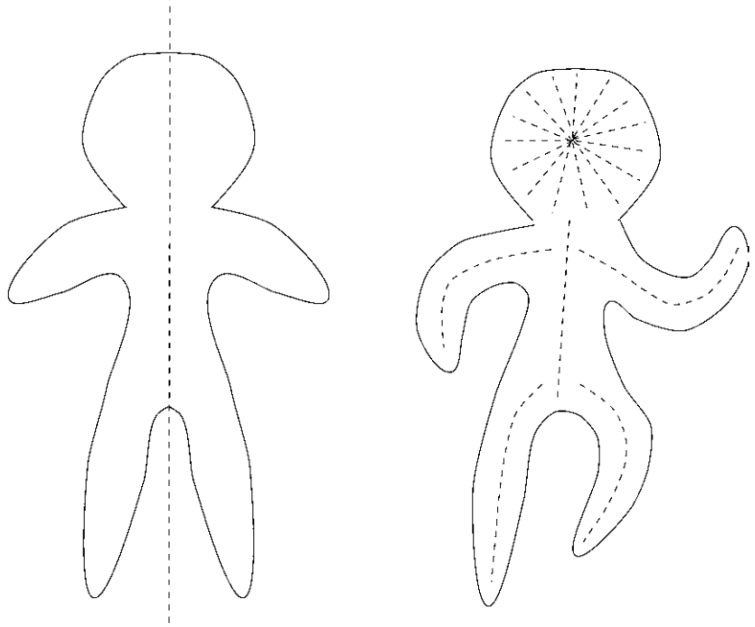

(a) Global (b) Local

Figure 1.3 Difference between global and local symmetries. Source: [97]

case, only the main symmetry axis is searched for. In the multiple case, every significant axis must be detected.

1.1.4 Symmetry in art

In early ages, the most ancient civilizations (i.e in Egypt, China) define a symmetrical balance between visual elements based on stone sculpturing and natural color painting inside different types of artwork (wallpaper paintings, statues, temple architectures, etc...). Figure 1.6 show different symmetry examples during ancient Egyptian era, in which mirror details are arranged around vertical axis in the center of each image.

In the last two centuries, the human kind; since Louis-Jacques-Mandé Daguerre and Nicéphore Niépce invited a camera obscura system for preliminary image recording; can capture different environments by composing the involved components in such way to feel the symmetry in front of location and angle of the camera view. Figure 1.7 shows two professional photos which defines symmetry: (a) the photographer's positioning to capture the rotational symmetry in the circular stony ground plus reflection one in the facade and surrounding green area. (b) the discussion grouping of old women reflecting the vertical axis in the photo center.

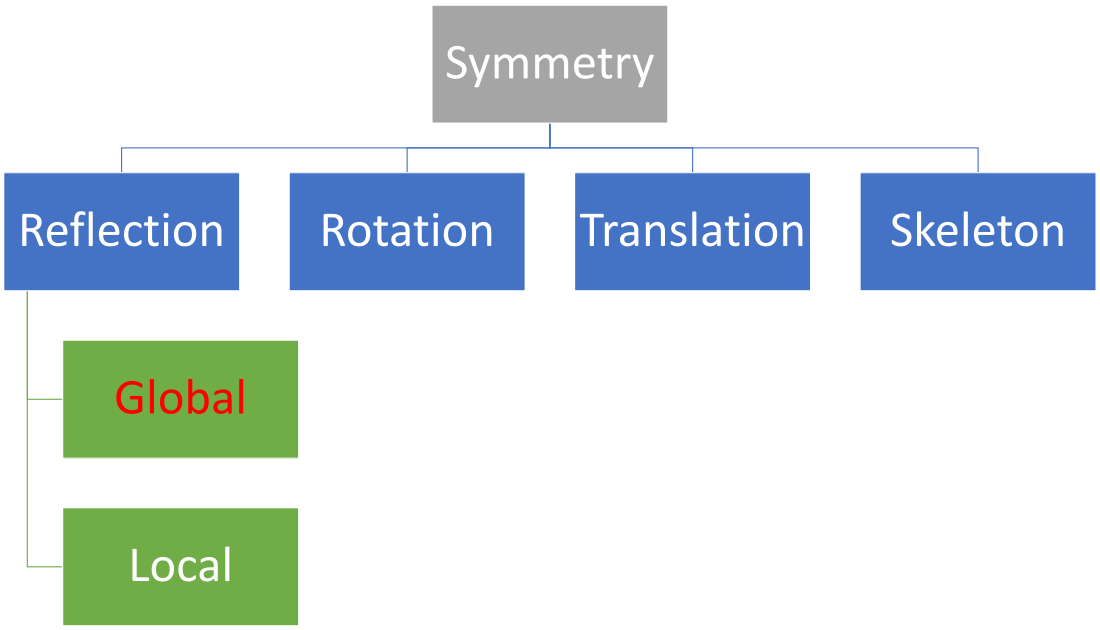

Figure 1.4 Symmetry tree.

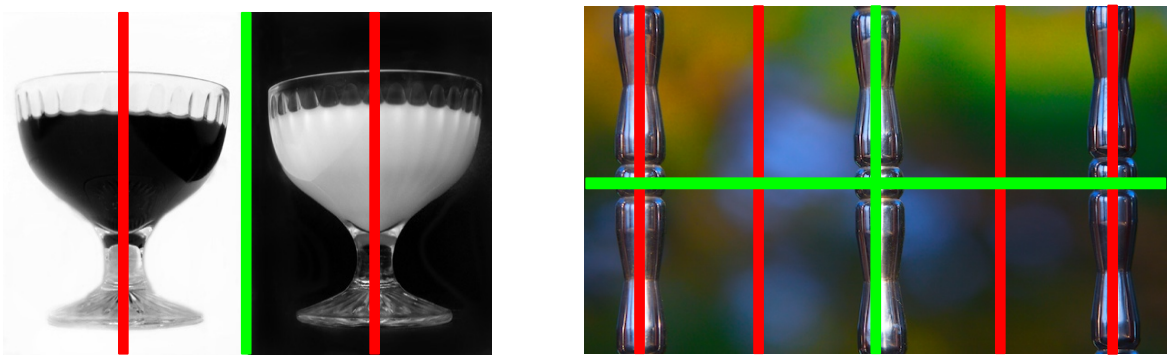

(a) (b)

Figure 1.5 Two photographic examples with major (in red) and minor (in green) symmetry axes. Source: AVA dataset [119]

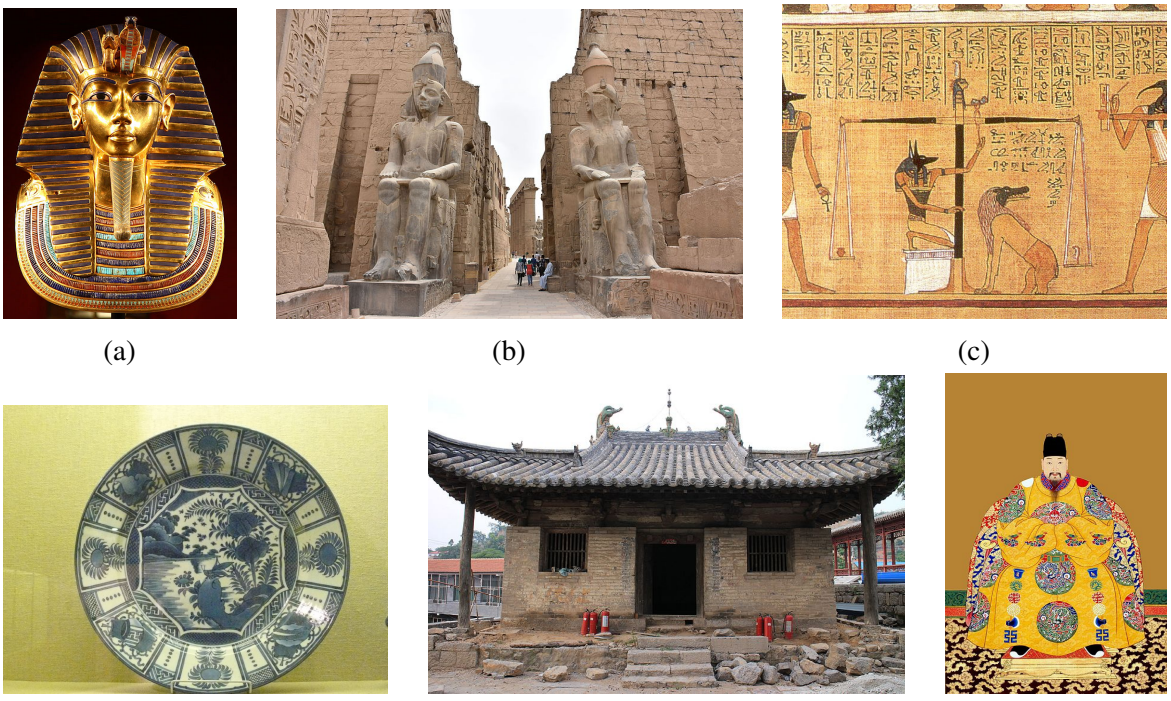

(a) (b) (c)

(d) (e) (f)

Figure 1.6 Symmetry in ancient Egyptian and Chinese civilizations: (a) Golden mask of Tutankhamun in the Egyptian museum, Egypt. (b) Entrance of Luxor temple, Egypt. (c) Book of the Dead in British museum, UK. (d) Qinghuaci plate in Brooklyn museum, USA. (e) Prince Zhu Youyuan in the Palace Museum, China. (f) Wooden relic from the tang dynasty, China. Source: Wikipedia

Art principles [75] are the visual concepts that the artist does for putting basic art elements (line, color, shape, etc.) together and analyzing the relationships between those elements to create composition of an artwork. Balance is one of the main art principles, in which the basic elements are arranged symmetrically generating a weighted similarities. Zhao et al. [171] used the statistical information of the rotational and reflectional symmetry as a balance measure for emotion recognition.

1.1.5 Symmetry in computer vision

A lot of computer vision tasks requires some kind of symmetry detection: pattern recognition, object detection (person, face,...), character recognition, traffic sign detection, 3D reconstruction. Atallah [10] defined a first algorithm in 1980's to detect reflection symmetry axes inside a figure, respect to the geometrical properties involved. Some symmetry contributions were introduced for decades until the production of the baseline algorithm by Loy and Eklundh [101] in 2006. Different symmetry competitions were held in the major

(a) (b)

Figure 1.7 Two symmetry examples of symmetric photography in the following locations: (a) Canada, and (b) Turkey. Source: [168].

computer vision conferences during 2010's (CVPR'11 [134], CVPR'13 [95], ICCV'17 [53]) to refine the proposed algorithms among synthetic and real-world images. After the stability of symmetry detection methods, they are recently involved in different computer vision applications related to the art domain (Aesthetic assessment [77, 102, 135, 137, 104, 146, 20, 139, 153], Photo quality assessment [40, 41, 56, 147], Aesthetic rating [2]). A lot of modern computer vision tasks require the symmetry detection as a middleware process to refine the results of pattern recognition and object detection purposes.

1.2 Objectives

Figure 1.8 defines the hierarchical connections between art and computer vision domains defining symmetry scenery to understand the involved environment context. From art domain, the basic elements (i.e. lines, color and texture) are combined together into define art principles (i.e. balance, contrast and pattern). Such that these principles are arranged together to artistically interpret the involved scene. From computer vision domain, the low-level features (i.e. edges and curves) are merged together describing the major visual cues (i.e. existence of symmetry, repetition of patterns and localization of vanishing points), leading to the high-level cues to estimate the involved environment based on the aesthetic measure or scene analysis. In this thesis, we aimed (red arrow in figure 1.8) to define precisely the transformation between low-level features and symmetry. In the beginning, we collaborated with art scientists at CIREC Lab [1], Jean Monnet university to make a symmetrical study on

1. https://www.univ-st-etienne.fr/fr/cierec.html

different historic photo collections [2] (Siemens, Paul Martial) of Saint-Etienne city during the industrial era (1900-1950). Figure 1.9 shows some of these photo collections that are actively used for public audience at museum of Modern-Art of Saint-Etienne. Then, we set the main objective of this thesis in developing a robust algorithm to detect global symmetry axes for single and multiple cases. In addition, we introduced a public symmetry dataset of professional and artistic images with aesthetically details, which can be used as benchmark to find global symmetries semantically.

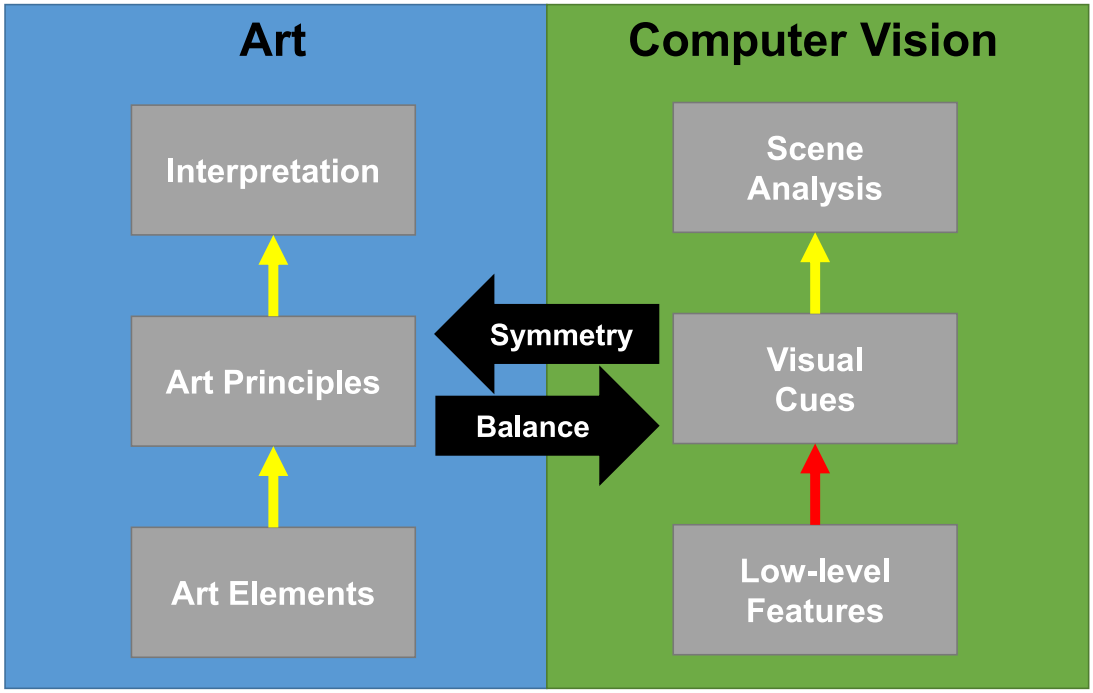

Figure 1.8 Relationship between art and computer vision domains. The red arrow defines our proposed work.

1.3 Problem definition

We firstly define a symmetry detection by matching similar but non-identical elements along the regional sides of an image, then categorize symmetry into local and global with focusing on the major ones respect to corresponding scores, and finally describe a symmetry measure for art retrieval systems. We are aware about the fact that finding out global symmetries has limited functionality in real-world images [101, 28]. For this reason, we developed different innovative methods in retrieving the salient features and analyzing the

2. https://viva-arts.univ-st-etienne.fr/

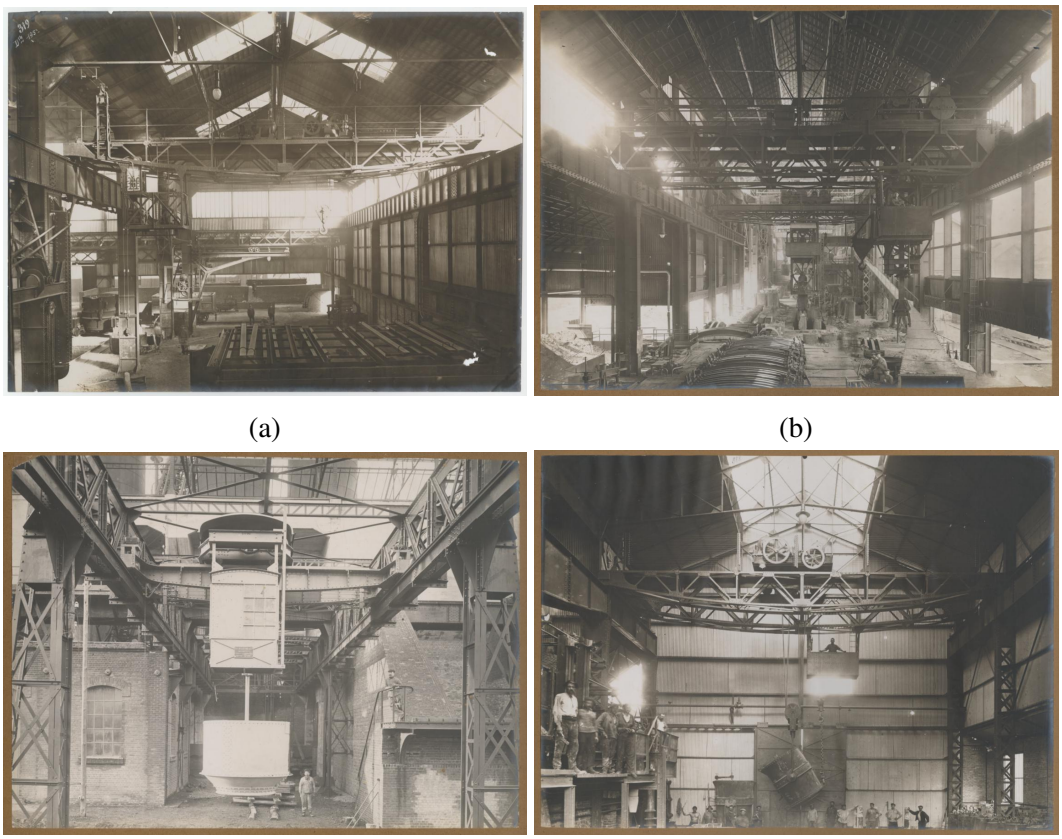

(a) (b)

(c) (d)

Figure 1.9 Some symmetrical historical examples of indoor industrial scenes used for artistic analysis and digital visualization. Source: VIVA-ARTS project, UJM.

corresponding descriptors' matching in symmetric way. We employed standard benchmark [95, 53] to evaluate the proposed algorithm w.r.t. the state of the art.

1.4 Contribution

The following research papers have been accepted during this thesis:

W1 Elawady, M., Ducottet, C., Alata, O., Barat, C., & Colantoni, P. (2017). Wavelet-Based Reflection Symmetry Detection via Textural and Color Histograms: Algorithm and Results. ICCV 2017 Workshop A Challenge: Detecting Symmetry in the Wild. **Competition Winner** [45, 46]

C1 Elawady, M., Alata, O., Ducottet, C., Barat, C., & Colantoni, P. (2017). Multiple Reflection Symmetry Detection via Linear-Directional Kernel Density Estimation. In

International Conference on Computer Analysis of Images and Patterns. **Core Rank B** [43]

C2 Elawady, M., Barat, C., Ducottet, C., & Colantoni, P. (2016). Global Bilateral Symmetry Detection Using Multiscale Mirror Histograms. In International Conference on Advanced Concepts for Intelligent Vision Systems. **Core Rank B** [44]

We can summarize our contribution in this thesis as follows:

— A novel symmetry detection algorithm to find global axes based on Log-Gabor feature extraction, plus textural and color neighboring information, published in the research papers $W1$ and $C2$.

— A weighted kernel density estimation to handle both linear and directional data to refine the accuracy of the symmetry peaks and the selection of corresponding voting features, published in the research paper $C1$.

— A continuous maxima-seeking technique using mean-shift scheme to find the symmetrical axes from a polar-based voting representation in a continuous way.

— A groundtruth of single symmetry axes inside artistic photographs extracted from the large-scale Aesthetic Visual Analysis (AVA) dataset [119], published in the research paper $C2$.

The proposed methods in this thesis are dataset and domain independent. We validated those methods among all public symmetry datasets and also experiment them in the disciplines of image processing. In summary, we believe that these methods could be utilized for different purposes, for example to detect natural objects and man-made structures in real-world and art images, to segment color and depth information, and to cluster linear and directional data.

1.5 Outline

The outline of this thesis is as follows:

— **Chapter 2** presents the background to detect global reflection symmetries. First, we performed a review study about the state-of-art algorithms. Secondly, we defined the previous symmetry competitions and explained the evaluation metrics used for the comparison of detection methods across these competitions. Finally, we describe the public datasets and the introduction of our proposed dataset 'AvaSym'.

— **Chapter 3** presents the proposed symmetry features and weights developed during this thesis to detect the global symmetries inside real-world images. Firstly, we provide the background related to feature extraction for symmetry detection. Secondly, we present the methodologies to compute semi-dense Log-Gabor features plus the textural and color metrics for introducing the symmetrical weights. Finally, we

provide the experimental results with the public datasets, then we compare the detailed results with state-of-art symmetry methods.

— **Chapter 4** presents the symmetry voting and selection using a weighted kernel density estimation for mixed data types and their continuous extension based on the mean-shift algorithm, to find maxima in the linear-directional space and find its corresponding voting feature points. We also provide a single and multiple symmetry benchmark using the recent dataset (ICCV 2017) w.r.t. state-of-art methods.

— **Chapter 5** summarizes conclusions and possible future work of the proposed framework for global symmetry detection in different computer vision and art domains.

Chapter 2

Literature Review

Résumé: La détection de la symétrie de réflexion est une étape intermédiaire crutiale dans certaines applications récentes de vision par ordinateur. En effet, les symétries globales correspondent souvent à des caractéristiques visuelles saillantes de niveau sémantique élevé. Dans ce chapitre, nous proposons d'abord une classification des approches existantes, puis nous examinons les algorithmes de référence correspondants. Dans un deuxième temps, nous mettons en évidence les principales compétitions de détection de symétrie, et enfin nous présentons les bases publiques d'images existantes et les mesures d'évaluation que nous utiliserons tout au long de la thèse pour comparer nos contributions à l'état de l'art.

Abstract: Detection of reflection symmetry is a crucial intermediate step in some recent computer vision applications. Indeed, global symmetries often act as high semantic level salient visual features. In this chapter, we will propose a classification of existing approaches and review the corresponding key baseline algorithms. We will highlight specifically the major competitions for symmetry detection, plus will present the public datasets and evaluation metrics that we will use throughout the thesis to compare our contributions against state-of-the-art.

2.1 State of the art

In this section, we will outline the most important work in reflection symmetry detection, and will structure them on the basis of symmetrical extraction and selection into the following categories: intensity, feature, segmentation, and learning. Intensity-based methods induce the symmetrical hypothesis from pixel-wise image calculations, but feature-based approaches use local keypoints as input for symmetry discovery. Segmentation-based methods look for object patterns inside an image, in order to separate them from the background and explore the similarity inside these patterns. Learning-based algorithms use the supervised neural

networks to find symmetries inside an image. The underlined methods in table 2.1 are state-of-art which we will compare our contributions against. Other works of reflection symmetry detection are not involved in the literature review due to out-of-scope objectives (graphical shapes [162, 91], image segmentation [145], feature extraction [68], image matching [73], image saliency [32], water reflection [169], object detection [63], motion estimation [64], and object tracking [93]).

2.1.1 Intensity-based detection

In the eighties, Atallah [10] proposed the first symmetry detection method based on the geometrical characterization of predefined primary objects (i.e. point, segment, and circle). He defined a planar algorithm to find reflective similarities between these simple geometrical objects in an optimal condition (very sensitive to any type of transformation). Figure 2.1 shows symmetrical results of Atallah's method for points, lines and circles in a binary environment. Marola [108] improved the planar symmetry detection through finding the maximum likelihood using pixel-wise auto-correlation transform. This method lacks fast computation time to compute over nowadays images with high resolution. Sun and Si [143, 144] used the distribution of gradient orientation based on Fast Fourier Transform (FFT), to define multiple axes of a single object inside a 2D image. Symmetry axes are then detected by computing the auto-convolution of the distribution of gradient orientation. However, it requires first that the image objects have clear edges with a quite uniform background and second that the symmetry is distributed over the whole image. Figure 2.2 shows Sun's work in addressing the symmetrical cases where the images only contain one single object in gray-scale environment. Keller and Shkolnisky [82, 83] defined an algebraic approach using Fourier transform to detect symmetry peaks inside an image. They firstly used polar-based Fast Fourier Transform (FFT) to generate frequency-based representation of an image (translation invariance), and secondly apply peak selection algorithm called MUSIC [133] estimating high-order symmetries. The proposed work needs global periodic patterns in order to discover the existence of significant symmetry axes. Figure 2.3 shows the single and multiple symmetrical cases (red lines) of natural images with central objects.

In recent years, Cicconet et al. [29, 31, 30] enlightened back the intensity-based methods, using RANSAC [50] in selecting candidate features and Normalized Cross-Correlation [89] technique in symmetry finding. They validated the proposed work against different public datasets. The result gives competitive accuracy but still lacks an efficient performance of the time complexity. Figure 2.4 shows some symmetrical results (yellow lines) of Cicconet's work for different scenes: 1) landscape across main building and its towers, 2) mirror reflection of standing people over water, 3) macro view of an animal. Nagar and Raman [120]

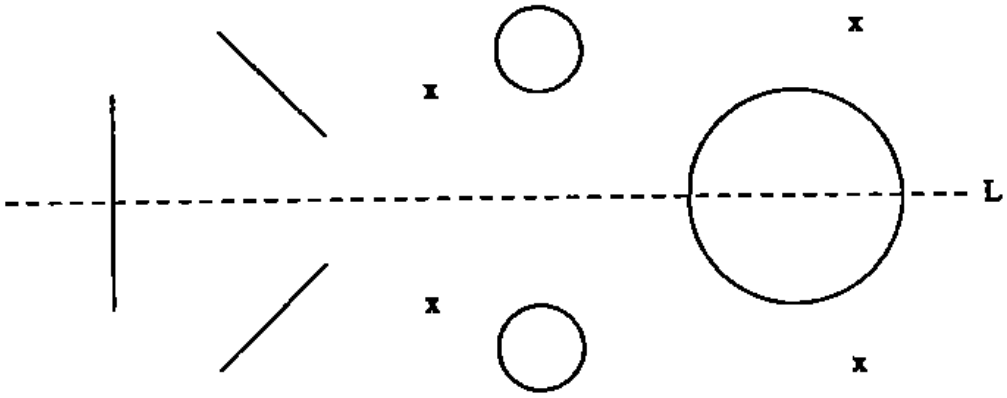

Figure 2.1 Illustration of the first symmetry detection method. Source: [10]

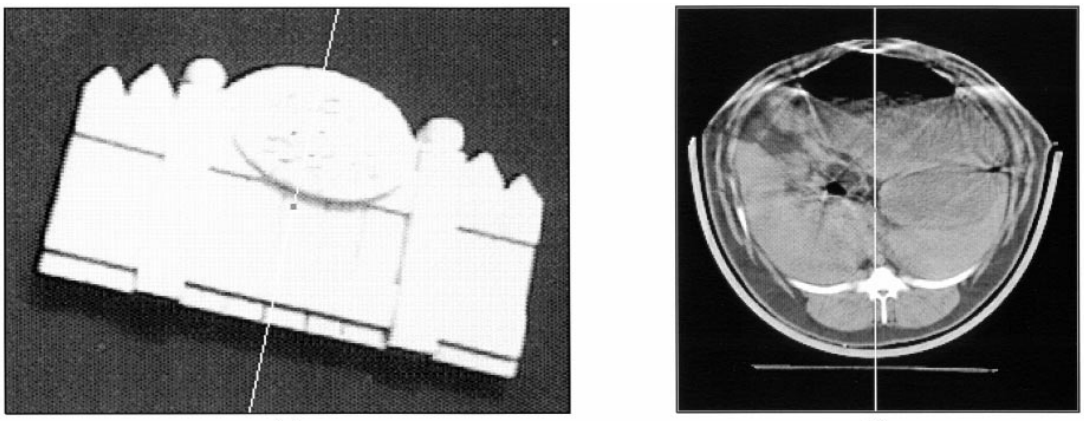

Figure 2.2 Results of Sun's detection method using gradient histograms in Fourier domain. Source: [144]

Figure 2.3 Results of Keller and Shkolnisky's approach in single and multiple symmetry detection. Source: [83]

determined the reflection symmetries inside an image through solving a linear correspondence problem using Riemannian Manifold Optimization algorithm. This work lacks a proper sampling method to downsize the image size into a reasonable symmetry representation. Figure 2.5 shows real-world and synthetic cases of Nagar's approach in extracting the feature points (green dots) and matching them (blue lines) in such way to find the major symmetry axis (red line). Gnutti et al. [61, 62, 67] decomposed the image into even and odd fundamental parts by analyzing their perspective energy, to investigate 2D spatial correlation properties inside an image, and use a saliency map identifying the major symmetries axes. In the end, Gnutti et al. [67] divided the detection process into three stages: (1) compute symmetry value for each position and direction of the input image using similar PRST symmetry measure [132], in such way that patch-based auto-convolution of an image is applied in direction perpendicular to the reflection axis with changes in the patching orientation, (2) store these symmetry values in a 3D stack in order to identify the candidate axes, (3) refine and reorder these candidates in descending order. This recent work of Gnutti lacks the proper way to measure the correct symmetries over the false segments. Figure 2.6 shows top axis candidates (red, blue and green lines) for Gnutti's detection method to detect symmetries in local and global scale.

In summary, all proposed work conducted pixel-wise analysis to find mirror similarities among 2D image space, but this deep analysis needs a huge computation time for proper symmetrical results. In addition, this type of detection is too sensitive to any degree of textural background resulting false positive symmetries.

Figure 2.4 Some examples of Cicconet's approach using Normalized Cross-Correlation. Source: [30]

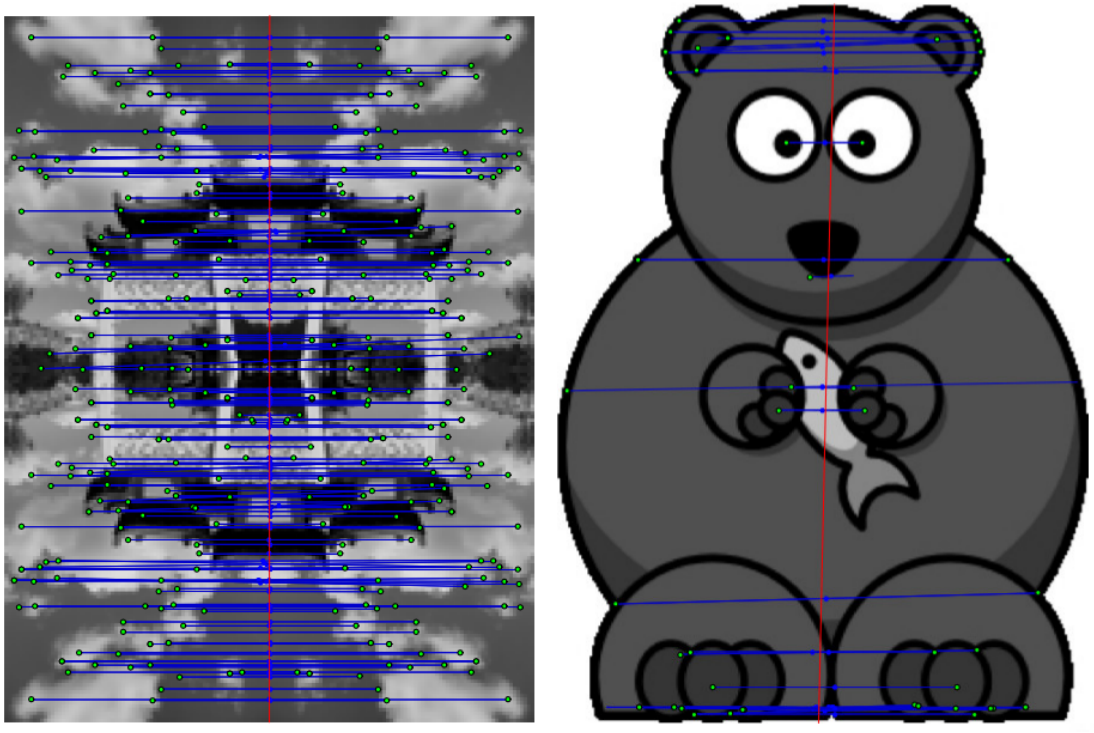

Figure 2.5 Explanation of Nagar and Raman' work in finding symmetrical correspondences inside images. Source: [120]

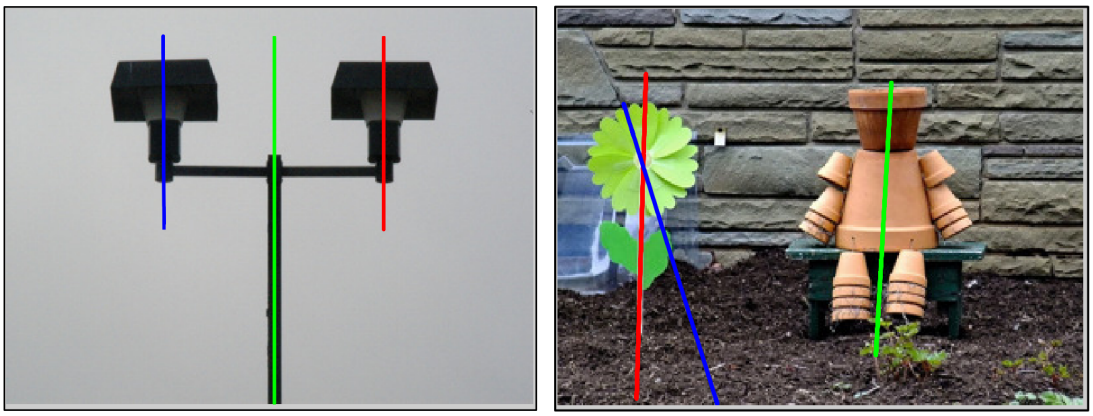

Figure 2.6 Some results of Gnutti approach in detecting multiple symmetry axes. Source: [62]

2.1.2 Feature-based detection

In 1993, Masuda et al. [110] extracted feature keypoints upon the application of the convolution process on the gradient information resulting from the Gaussian filter over an image, and selected the best similarities using the correlation process between the original and rotated versions. This work was a first attempt to use local features in detecting symmetrical axes, but still too sensitive to any background clutter noise. Figure 2.7 shows symmetrical cases where a single object exists on a quasi uniform background. Kirayati and Gofman [84] tired to combine intensity-level features as in Marola [108] plus local-features using circular Gaussian functions parameterized by its spatial coordinates, scale and orientation. They apply a genetic algorithm on these features to detect multiple symmetries. Figure 2.8 shows the symmetrical examples of Kirayati and Gofman method in closeup natural scenes, in which the symmetry axis corresponds to the white line delimited by the white circle defining the symmetrical area.

The first baseline algorithm was firstly proposed in mid 2000's by Loy and Eklundh [101]. They analyzed the bilateral symmetry from image features' constellation by introducing the general scheme (as shown in figure 2.9): (1) detection of local feature points using well-known SIFT [100] algorithm, associated with local geometrical properties (location, orientation, scale) and descriptor vectors. (2) pairwise matching and evaluation of a local symmetry magnitude of their descriptors, to generate axis candidates. (3) accumulation of their symmetry magnitude in a Hough-like voting space parameterized with orientation and displacement, to identify the dominant reflection axes inside an image. It lacks finding enough feature points leading to lose the meaningful symmetry axes of natural scenes with smooth objects with noisy background (see figure 2.11), due to mainly dependence on the

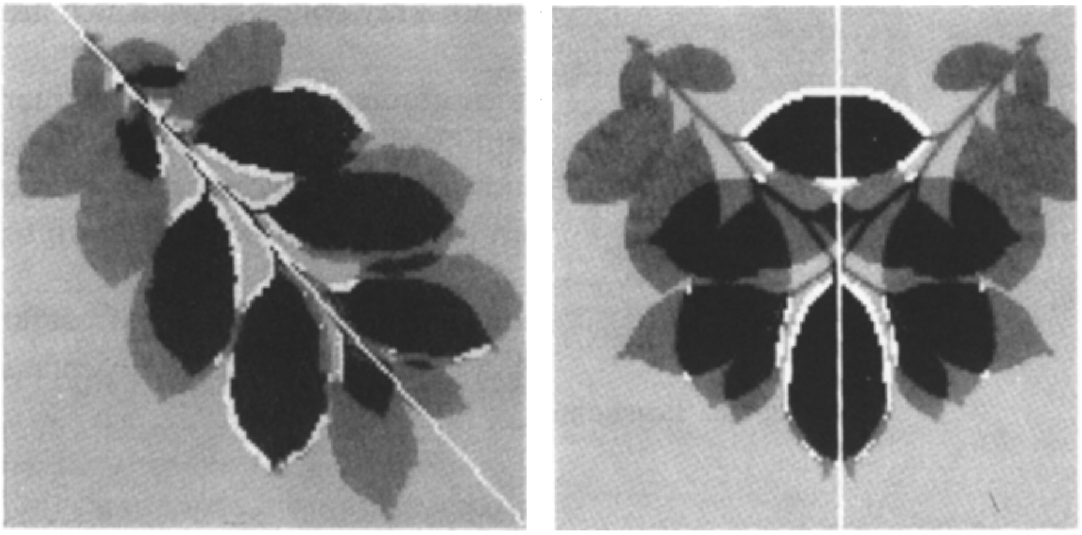

Figure 2.7 Orientation cases of Masuda approach in detecting single symmetries. Source: [110]

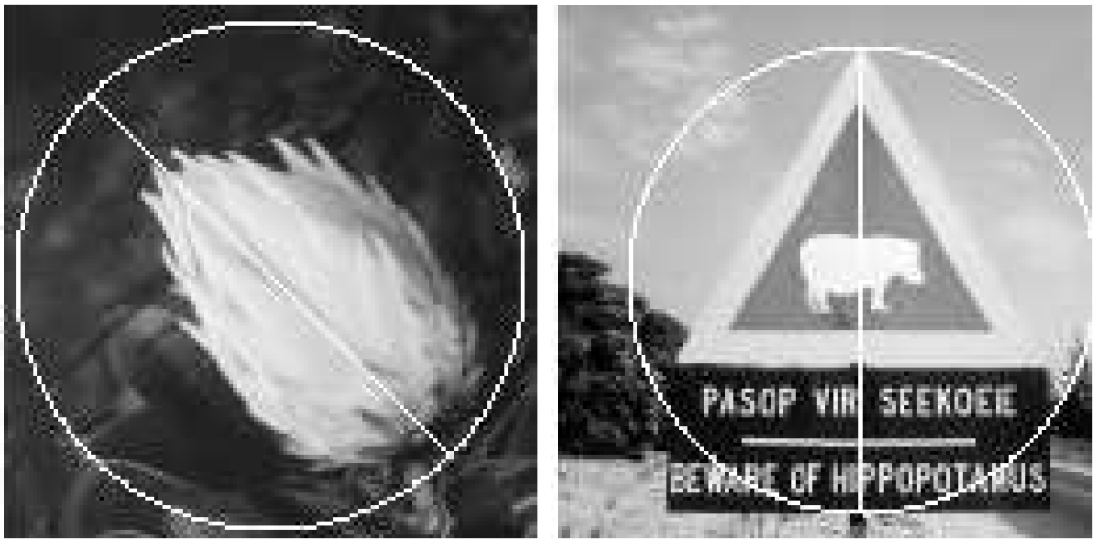

Figure 2.8 Symmetry examples of Kirayati and Gofman approach in selection of single symmetries with endpoints alignment. Source: [84]

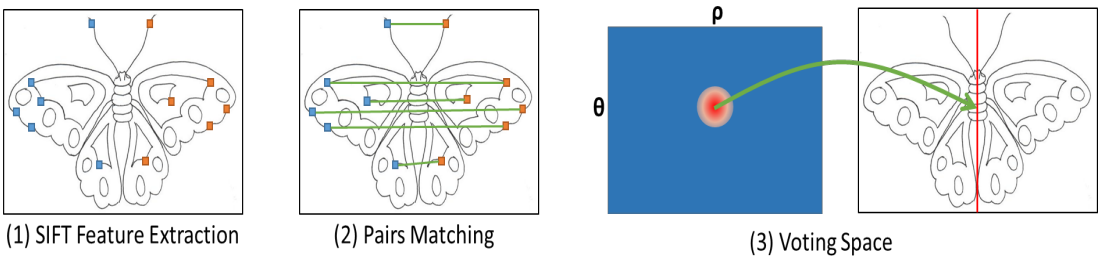

Figure 2.9 Loy's symmetry framework.

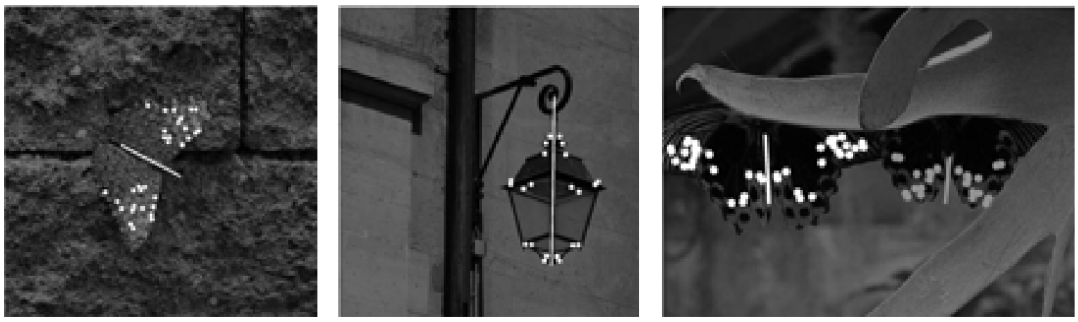

Figure 2.10 Loy's symmetry results. Source: [101]

hand-crafted properties of SIFT features. Figure 2.10 shows the symmetrical results of the baseline algorithm (Loy) in single and multiple cases in natural scenes. Symmetry axes are highlighted in white & grey lines, and their corresponding involved feature key-points in white & grey dots.

Table 2.1 A summary of the proposed methods for reflection symmetry detection

Category	First Author (*Year*)	Extraction	Selection	Dataset(s) / Competition(s)
Intensity	Atallah (*1985*) [10]	Pattern finding	Planar object matching	-
	Marola (*1989*) [108]	Planar autocorrelation		-
	Sun (*1995,1999*) [143, 144]	Intensity and gradient map	Orientation histogram	-
	Keller (*2004,2006*) [82, 83]	Pseudo Polar Fourier Transform (PPFT)	MUltiple SIgnal Classification (MUSIC) [133]	-
	Cicconet (*2016,2017*) [29, 31, 30]	RANSAC [50]	Normalized Cross-Correlation [89]	PSU2013[d] [95], NY[i] [27], ICCV2017[h] [53]
	Nagar (*2017*) [120]	Riemannian Manifold Optimization		PSU2011[c] [134], PSU2013[d] [95], NY[i] [27]
	Gnutti (*2017*) [62, 61, 66]	Even-odd Decomposition	Stacking Map	PSU2013[d] [95]
	Gnutti (*2017*) [67]	Planar Reflective Symmetry Transform [132]	Stacking Map	ICCV2017[h] [53]
Feature	Masuda (*1993*) [110]	Gradient over Gaussian	Rotational Correlation	-
	Kirayati (*1998*) [84]	Circular Gaussian Window	Genetic Algorithm	-
	Loy (*2006*) [101]	SIFT [100]	Weighted Hough	BioID[a]
	Cho (*2009*) [26]	MSER [111], Hessian [115] + SIFT [100]	Region Growing	PSU2008[b] [128]
	Mo (*2011*) [118]	SIFT [100]	Spectral Clustering	PSU2011[c] [134]
	Kondra (*2013*) [86]	SIFT [100]	Maximum Correlation	PSU2013[d] [95]
	Patraucean (*2013*) [130]	SIFT [100]	Contrario Theory	PSU2013[d] [95]
	Michaelsen (*2013,2017*) [114, 113]	SIFT [100]	Gestalt Algebra	PSU2013[d] [95], ICCV2017[h] [53]
	Cai (*2014*) [17]	SIFT [100]	RANSAC [50]	PSU2013[d] [95]
	Ming (*2013*) [116]	Pb [5] / Trapezoid [142]	Star Graph	PSU2012[e], BSDS[f]
	Cicconet (*2014,2016*) [28, 27]	Morlet	Weighted Hough	PSU2011[c] [134]
	Wang (*2015*) [161]	Canny [18] / DOPM	KNN	PSU2011[c] [134]
	Atadjanov (*2015,2016*) [7, 8]	Appearance of Structure	4-Dimensional Histogram	PSU2011[c] [134], PSU2013[d] [95]
	Nagar (*2017*) [121]	SIFT [100]	K-plane Clustering [16]	PSU2011[c] [134], PSU2013[d] [95]
	Nagar (*2017*) [122]	SIFT [100]	Symmetric PatchMatch [14]	PSU2011[c] [134], ICCV2017[h] [53]
Segmentation	Zabrodsky (*1992,1995*) [166, 167]	Symmetry Measure with Active Contour Algorithm		-
	Widynski (*2014*) [163]	Particle Filter for Ribbon & Contour Detection		BSDS300[f]
	Nagar (*2017*) [123]	Structure Edge detector [39]	SLIC [1]	BSDS300[f]
Learning	Tsogkas (*2012*) [152]	Multiple Instance Learning [11]		BSDS300[f]
	Funk (*2017*) [54]	Dense CNN Regression [24]		PSU2013[d] [95], COCO[g]

a. http://www.bioid.com/downloads/facedb
b. link doesn't exist anymore.
c. http://vision.cse.psu.edu/research/symmComp/index.shtml
d. http://vision.cse.psu.edu/research/symComp13/content.html
e. link doesn't exist anymore.
f. https://www2.eecs.berkeley.edu/Research/Projects/CS/vision/bsds/
g. http://mscoco.org/
h. http://sites.google.com/view/symcomp17/
i. https://symmetry.cs.nyu.edu/

Figure 2.11 Loy's fail cases.

Since then, the following algorithms proposed some improvements and refinements of Loy's method. Cho and Lee [26] split and merged local symmetry regions of an image by investigating both photometric and geometrical properties using multi-layer Region Growing (RG) algorithm. This work can't determine the precise angle of symmetry axes. Figure 2.12 explains how RG algorithm leads in having feature blobs (the key-points in colored dots and the blob boundaries in colored convex-hulls), which allows Cho and Lee method to identify the different symmetrical axes (colored lines) inside the sample image. Mo and Draper [118] presented simple improvements to Loy algorithm [101] by pairing all feature points instead top closest matches for each point, and using a non-weighted frequency-based voting space for symmetrical peak selection. These improvements produced more particles for the symmetry axis, to elongate the output axis defining the global texture information of an image, but at the same time they introduced some matching noise resulting in detecting wrong symmetry axes. Kondra et al. [86] defined multi-scale correlation measures between SIFT feature points to identify the symmetrical regions based on orientation-based matches. Patraucean et al. [130] validated the mirror-symmetric candidates using statistical procedure called Contario Theory. Michaelsen et al. [114] used the SIFT descriptors to describe high-detailed symmetric patterns of the image plane using Gestalt Algebra concept. Cai et al. [17] focused on introducing an adaptive SIFT feature detection over Loy2006 method [101] to refine the total number of keypoints required to guarantee well-defined symmetry results. Figure 2.13 shows top 3 symmetrical candidates (red lines with red font order numbers) for focused objects inside outdoor scenes.

Since 2013, the following methods deployed the local edge information instead of SIFT, to redefine the localization of symmetry axes inside an image. Ming et al. [116] extracted the symmetric pairs of edgelets based on the contour information, and then established star-shaped graph using these pairs, to estimate the symmetric axes. Figure 2.14 shows multiple symmetry candidates over natural images (in such decreasing order: red, yellow

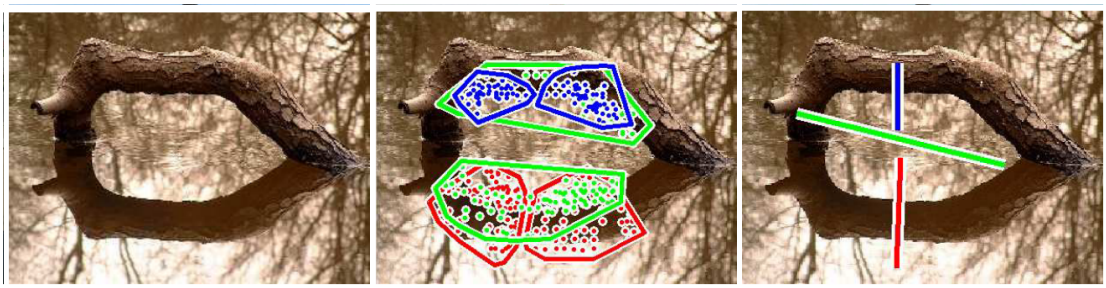

Figure 2.12 Illustration of obtaining symmetry axes using Cho and Lee approach, based on Region Growing algorithm. Source: [26]

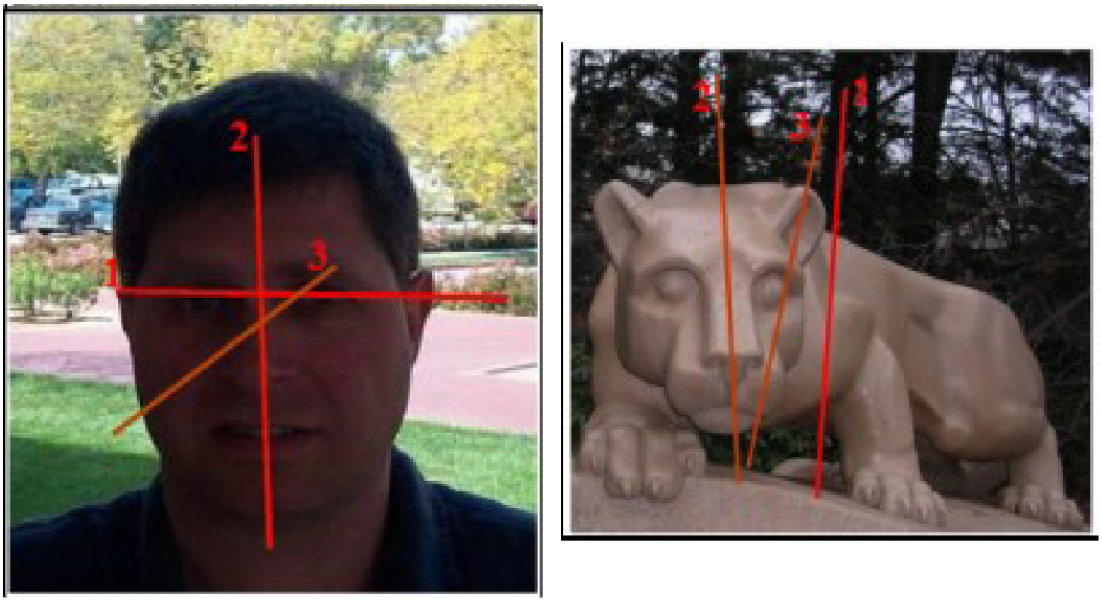

Figure 2.13 Symmetry examples of obtaining multiple axes and their importance order using Cai approach. Source: [17]

and green). Cicconet et al. [28] introduced the second baseline framework (as shown in figure 2.15) in 2014, it consists of: (1) Extraction of a regular set of wavelet-based feature points with local edge amplitude and orientation. (2) given any pair of points, definition of an axis candidate within symmetry coefficients. (3) construction of a voting histogram as the sum of the contribution of all pairs of the feature points for a given axis. (4) extraction of the best candidates representing the voting maxima over the mirror symmetry histogram. This framework misses the neighborhood's information inside the feature representation, plus it depends mainly on the scale parameter of the wavelet-based edge detector. Any photographic environment with highly-detailed texture objects with non-blurred background results incorrect global symmetry. The same authors [27] presented a new parameter-based algorithm based on direct product of complex wavelet filtering outputs, plus they developed a convolution-based technique to find precisely the endpoints of symmetry axes instead of using the traditional convex hull method [101]. This proposed algorithm is computationally expensive and outputs incorrect symmetry according to the definition of the wrong properties of the image shapes as in figure 2.16. Wang et. al [161] defined an edge descriptor with respect to the diagonals of the orthogonal projection matrices (DOPM) after Canny detector to define locally affine invariant features, to use them in a matching step based on K-Nearest Neighbor (KNN) clustering method. This work lacks a standard dataset validation to understand its deficiencies. Figure 2.17 displays the symmetrical results of Wang's algorithm in detecting multiple axes (red lines) among the scenes of different objects or a single object. Atadjanov and Lee firstly proposed scale-invariant curvature-based histograms [7] for symmetry computation, and refined the feature detection and extraction scheme [8] for high-dimensional histogram comparison. Figure 2.18 presents the axis candidates in colored lines defining symmetry inside single object scenes, in which the results has to be clustered and aligned together in order to strength up the major axis candidates. Finally, Nagar and Raman [122, 121] used SIFT features to compute a symmetrical map using an energy minimization approach firstly and then after a randomized algorithm called Patch Match [14].

In summary, feature-based methods are very fast to extract important keypoints around an image, in order to easily find reflective symmetries among them. They are mainly concentrated to find local symmetry axes instead of global ones.

2.1.3 Segmentation-based detection

In mid 1990's, Zabrodsky et al. [166, 167] defined a symmetrical measure to find a similar objects inside an image, but it needs the symmetry centers as initial points for the correct segmentation process. Figure 2.19 presents the symmetrical examples of similar

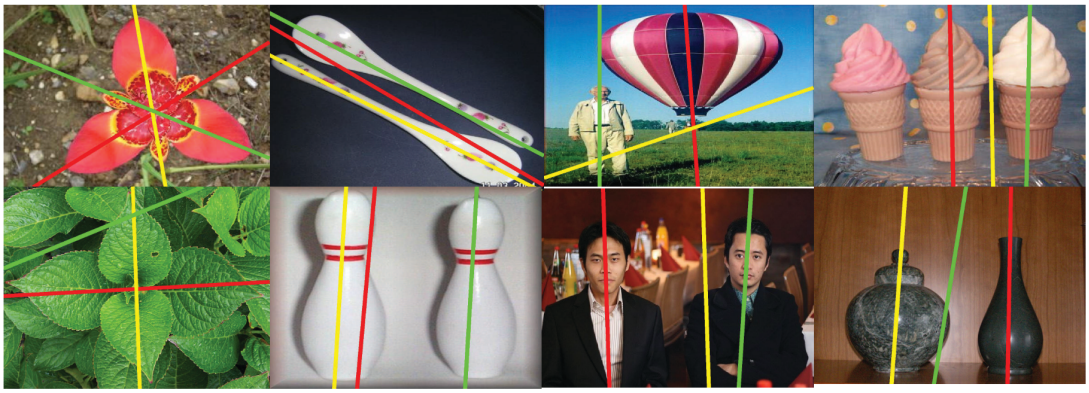

Figure 2.14 Some symmetry results of Ming's detection work based on contour key-points. Source: [116]

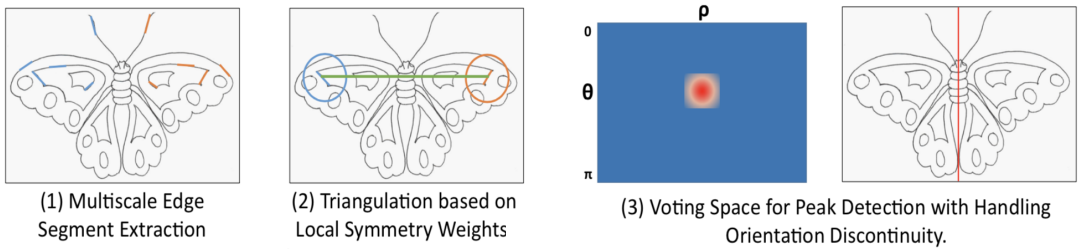

Figure 2.15 General framework of Cicconet's symmetry detection approach [28].

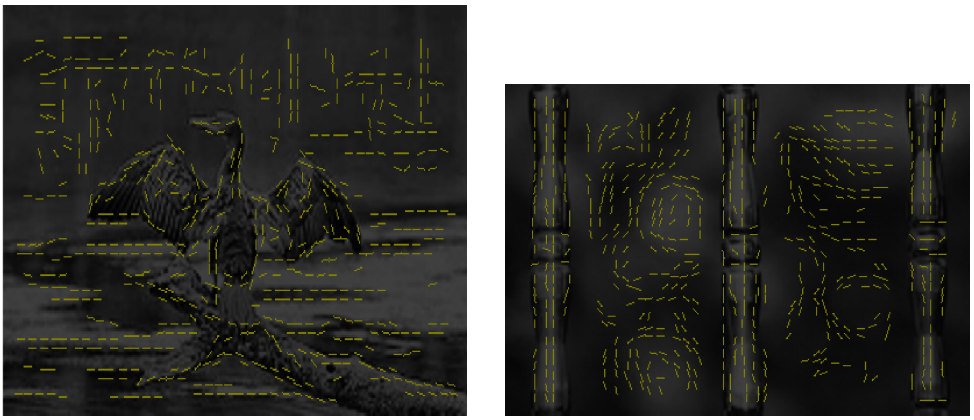

Figure 2.16 Ambiguous distribution of the edge segments, from Cicconet et al. [28].

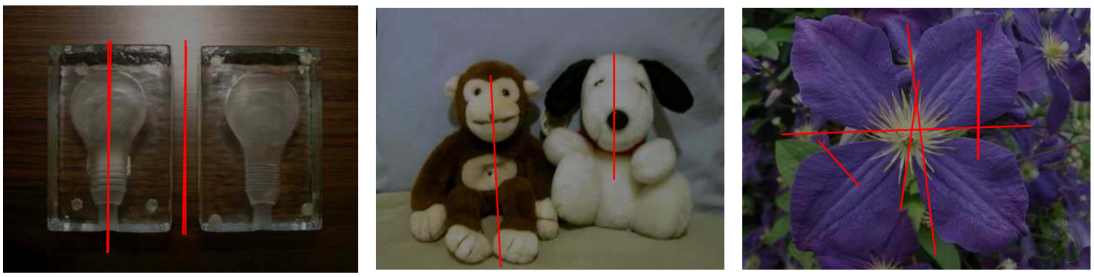

Figure 2.17 Results of Wang's symmetry detection algorithm, presenting possible multiple axis candidates. Source: [161]

Figure 2.18 Symmetrical results of Atadjanov's detection method in finding multiple axes inside images. Source: [8]

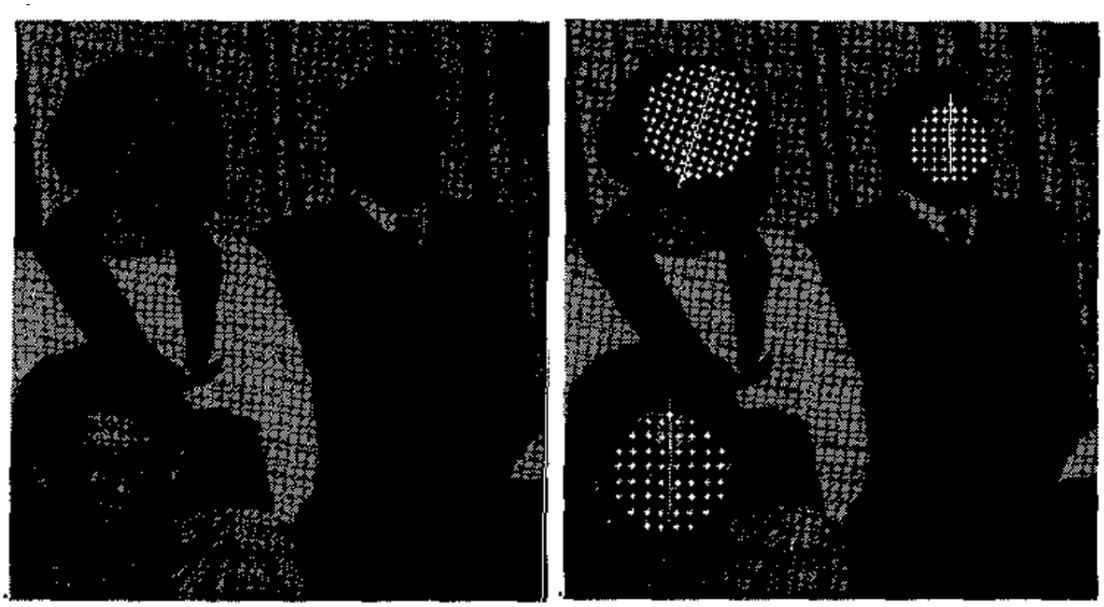

Figure 2.19 A segmentation example of human faces through obtaining multiple symmetry axes using Zabrodsky approach. Source: [167]

circular regions (defined by white dots with middle axes in white lines) helping in segmenting the human faces out of the scene. After long years, Widynski et al. [163] proposed a ribbon detection algorithm using Particle filter method to find skeleton symmetries inside local objects. This methods needs to work with predefined structures, in order to detect the correct centroids inside. Figure 2.20 shows semi-reflection and discontinued symmetries (in red irregular lines) of scenes' elements (i.e. humans, statues, houses) along side with some dual symmetrical axes between the similar objects. Recently Nagar and Raman [123] simply computed a feature map using a recent edge detection [39] and then apply SLIC algorithm [1] based on the maximum likelihood of the edge map as initial centers. This work mainly depends on the magnitude values of detection method and lacks neighborhood information. In summary, this type of methods targets segmenting the important objects inside an image, and then find symmetries within. Figure 2.21 defines the symmetry detection pipeline of Nagar's method in which the butterfly image is segmented using the SLIC technique into super-pixel regions (defined by red boundaries), followed by selection of symmetrical keypoints (color dots) in these regions and matching them (color lines connecting color dots) in such way to find proper symmetry axes.

Figure 2.20 Examples of inner symmetries inside image's objects using Widynski approach. Source: [163]

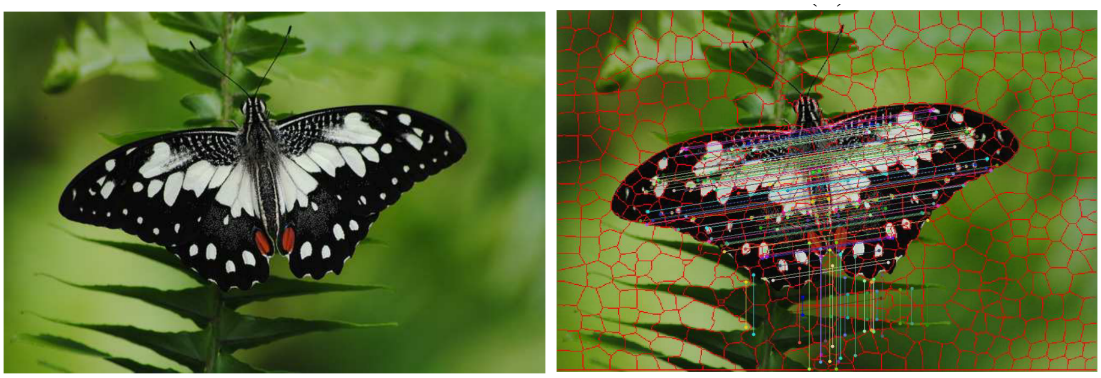

Figure 2.21 Explanation of object symmetry extraction using Nagar approach based on super-pixel segmentation technique. Source: [123]

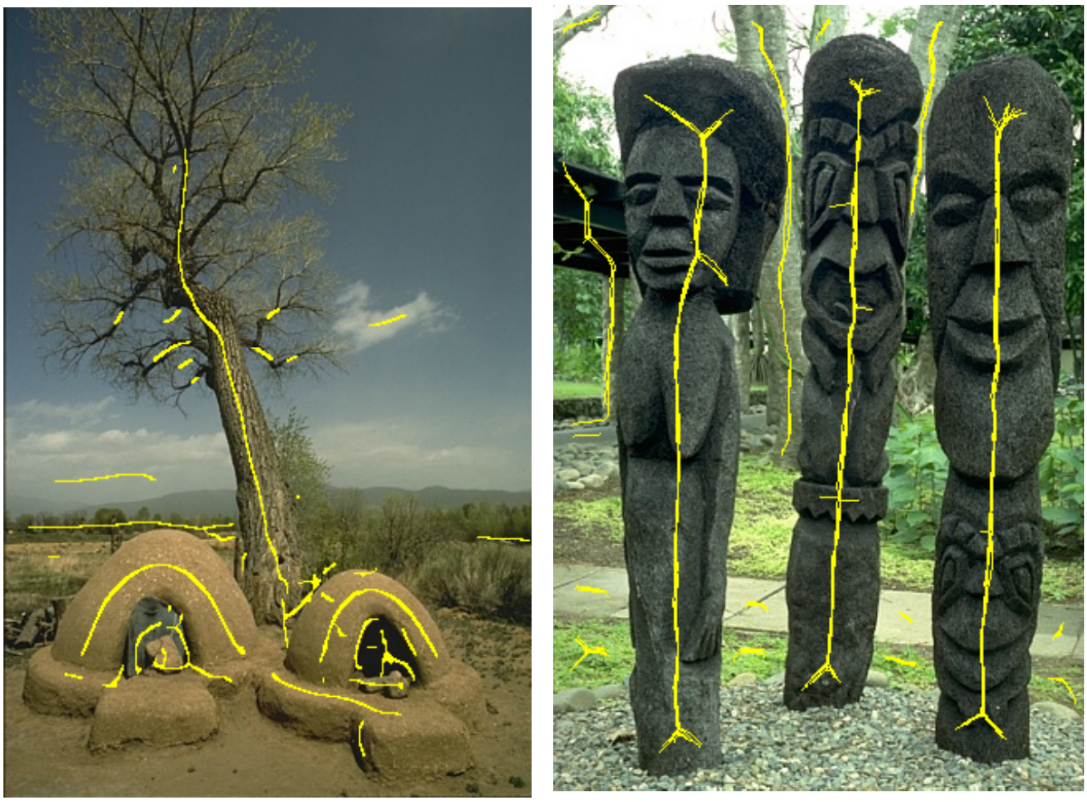

Figure 2.22 Examples of finding local symmetries inside image's objects using Tsogkas approach. Source: [152]

2.1.4 Learning-based detection

In early 2010's, Tsogkas and Kokkinos [152] firstly introduced the learning-based detection method based on the brightness, color and textural information. They used histogram-based region discrepancy, and spectral clustering features as latent variables for Multiple Instance Learning (MIL), in order to output symmetry probability maps. Figure 2.22 shows detection of reflection and skewed symmetries (yellow lines) defining the skeleton version of scenes' objects. Funk and Liu [54] recently developed the first deep neural network to detect local and global reflection symmetries according to the human perception system. In summary, the supervised learning methods implicitly find symmetrical information inside images for image segmentation applications including the medial axes of the focused objects, but they couldn't retrieve the main symmetrical axes based on the global mirror contribution of the image parts. Figure 2.23 shows the heat maps (gradient colors from maximum in red into minimum in blue) where the possible symmetries should exist (i.e. cat face in left image, tower in right one).

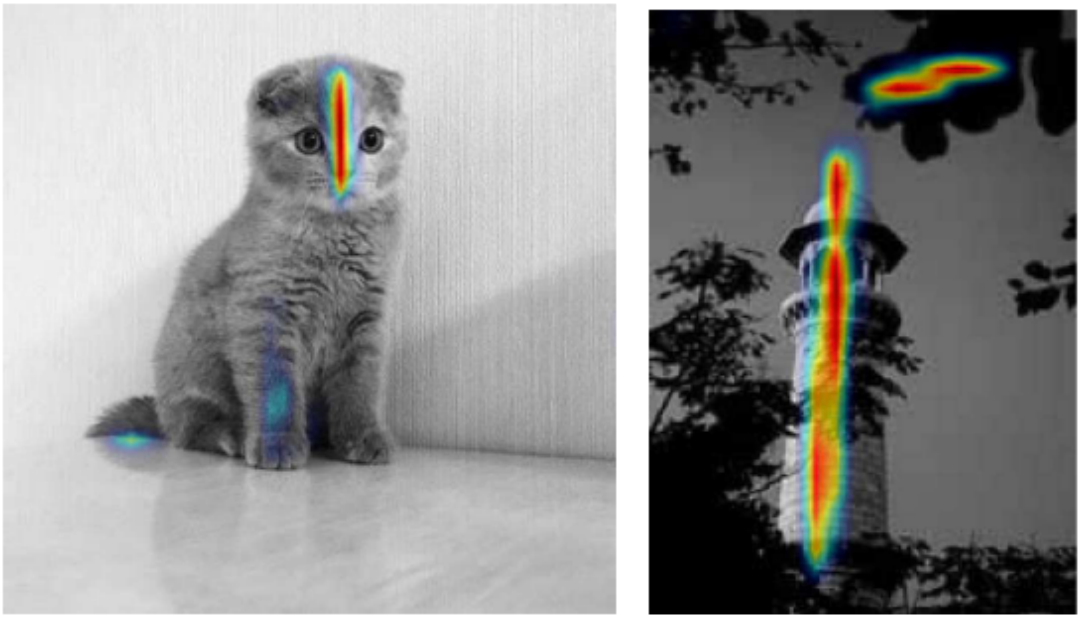

Figure 2.23 Results of multiple symmetry detection using Funk approach based on Deep CNN models. Source: [54]

2.2 Symmetry competitions

Three different competitions were organized by PSU vision group at major computer conferences:

— First symmetry competition [134] conducted in CVPR workshop 2011 with following participants (Mo and Draper [118], Kondra et al. [86]) with Loy and Eklundh [101] as a baseline. As shown in figure 2.24, the competition categorized preliminary results in two groups (single/multiple, synthetic/real) and output the results in terms of the best recall and precision values among each participant. In nutshell, the baseline outperformed all participants with strong competence from Kondra in the real/multiple cases.

— Second symmetry competition [95] conducted in CVPR workshop 2013 with following participants (Patraucean et al. [130], Michaelsen et al. [114], Petrosino et al.) with the same baseline algorithm (Loy and Eklundh [101]). The baseline algorithm [101] outperforms all participants of both competitions to find well-defined symmetry axes inside synthetic and real-world images. Figure 2.25 shows the competition results in terms of precision-recall curves with varying the symmetry scores among the axis candidates of each participating algorithm. In single case, the baseline algorithm [101] has better recall rates at lower precision levels but in general has overall best

performance over precision and recall rates. Patraucean et al. [130] has small recall advantage at some precision levels. In multiple case, the baseline algorithm [101] has the best recall results among all precision performance except at middle rates where Patraucean et al. [130] gives better results at minor scale. In general, Michaelsen et al. [114] has the worst performance among single and multiple cases.

— Third symmetry competition [53] conducted in ICCV workshop 2017 with following participants (Nagar and Raman [122], Guerrini et al. [67], Cicconet et al. [31], Michaelsen and Arens [113], Elawady et al. [46]) with two baseline algorithms (Loy and Eklundh [101], Atadjanov and Lee [8]). The classic algorithm [101] outperforms all participants of both competitions for single and multiple symmetry, plus the extra performance of the modern baseline [8] among the single symmetry competition. Figure 2.26 represents the competition results as in the previous competition (precision-recall curves) along side with a evaluation metric value (maximum $F1$ score). In single case, Guerrini et al. [67] has the worst performance without having the score threshold to vary, which results only one candidate to compare with. A new benchmark algorithm (Atadjanov and Lee [8]) overcomes the well-known baseline algorithm (Loy and Eklundh [101]). In multiple case, the baseline algorithm still has the best performance results over the new competent (Elawady et al. [46] as 2nd, and new benchmark algorithm [8] as 3rd).

In summary, these competitions lacks clarity about evaluation metrics to measure each detection method in the aspect of single and multiple cases. The following subsection will explain in-details how to evaluate all candidate axes for each method with respect to their corresponding symmetry scores.

2.2.1 Evaluation metrics

Assuming a symmetry line defined by two endpoints ($a = [a_x, b_y]^T$, $b = [b_x, b_y]^T$), quantitative comparisons are fundamentally performed by considering a detected symmetry candidate $SC = [a^{SC}, b^{SC}]^T$ as a true positive (TP) respect to the corresponding groundtruth $GT = [a^{GT}, b^{GT}]^T$ if satisfying the following two conditions: the angle between the two axes γ must be lower than some threshold γ_T, and the distance between axis centers ζ must be lower than other threshold ζ_T. The computation of γ and ζ is as follows:

$$\gamma = E(atan(\frac{abs(\begin{vmatrix} v_x^{SC} & v_x^{GT} \\ v_y^{SC} & v_y^{GT} \end{vmatrix})}{< v^{SC}, v^{GT} >})); \gamma < \gamma_T \,, \tag{2.1}$$

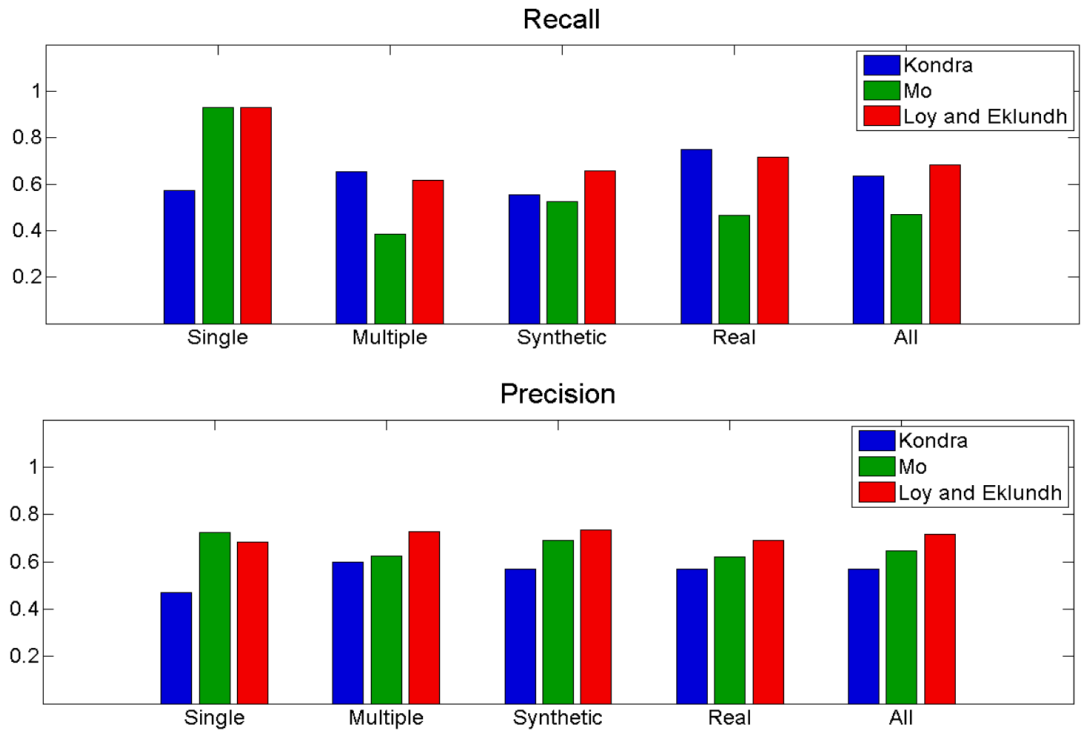

Figure 2.24 Results of 1st symmetry competition 2011. Source: [134]

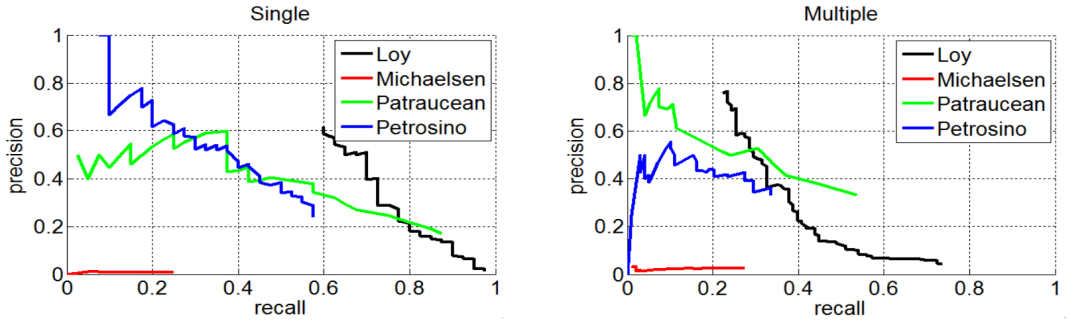

Figure 2.25 Results of 2nd symmetry competition 2013. Source: [95]

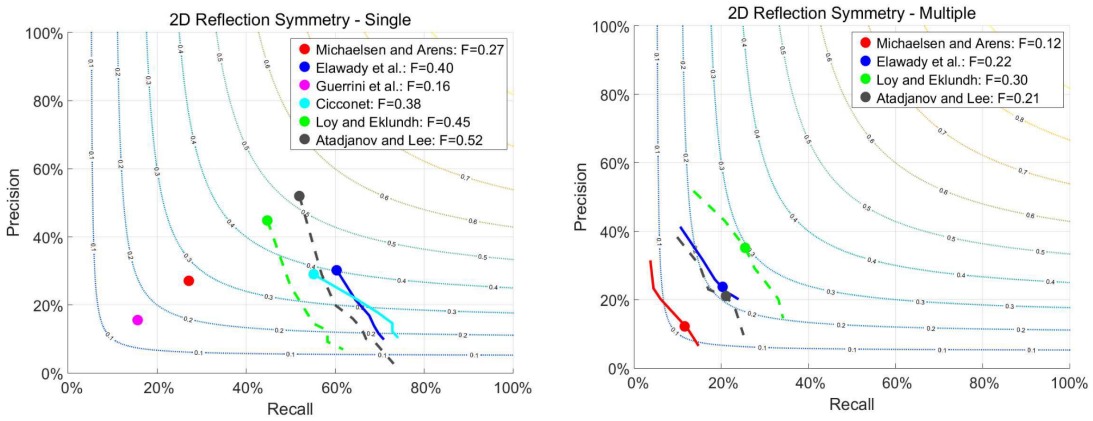

Figure 2.26 Results of 3rd symmetry competition 2017. Source: [54]

$$\zeta = \sqrt{(t_x^{SC} - t_x^{GT})^2 + (t_y^{SC} - t_y^{GT})^2};\ \zeta < \zeta_T\,, \tag{2.2}$$

$$v^{SC} = (a^{SC} - b^{SC}),\ v^{GT} = (a^{GT} - b^{GT})\,,$$

$$t^{SC} = \frac{(a^{SC} + b^{SC})}{2},\ t^{GT} = \frac{(a^{GT} + b^{GT})}{2},$$

$$E(\Gamma) = \begin{cases} \pi - \Gamma, & \text{if } \Gamma > \frac{\pi}{2} \\ \Gamma, & \text{otherwise} \end{cases}$$

Figure 2.27 represents visually angular and distance constraints between the detected and groundtruth axes, in which these constraints are upper-bounded by the corresponding thresholds γ_T and ζ_T. The values of these thresholds are defined in table 2.2 across different symmetry competitions. Given, each algorithm outputs multiple detection results representing the axis candidates ranked by their corresponding confidence scores. Furthermore, the precision PR and recall RC rates are defined by selecting the symmetry peaks according to the candidates' symmetrical scores, which are normalized by the highest detection score, to show the performance curve over all dataset images for each algorithm:

$$PR = \frac{TP}{TP + FP},\ RC = \frac{TP}{TP + FN} \tag{2.3}$$

where FP is a false positive (non-matched detection), and FN is a false negative (non-matched groundtruth). In case of single symmetries, one axis candidate can be only matched with a single groundtruth. While in case of multiple symmetries, a region containing axis candidates can be be grouped to match one groundtruth. Plus the false positive detection should be eliminated for correct performance computation.

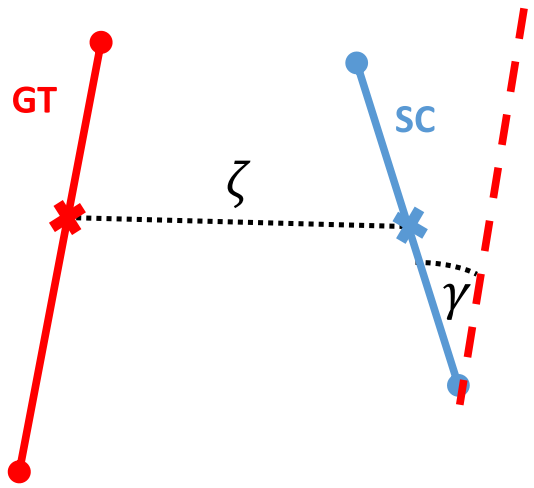

Figure 2.27 Evaluation metrics: A comparison between the groundtruth *GT* (red) the detected reflection symmetry candidates *SC* (blue) by measuring the distance ζ between the axes' centers and the angle γ between them.

$$max\{F_1\} = max\{2\frac{PR \times RC}{PR + RC}\} \tag{2.4}$$

Table 2.2 Threshold values of evaluation metrics across different reflection symmetry competitions.

Competition	γ_T	ζ_T
CVPR2011 [134]	10°	$20\% \times len(GT)$
CVPR2013 [95]	10°	$20\% \times min\{len(MT), len(GT)\}$
ICCV2017 - Training [6]	3°	$2.5\% \times min\{W, H\}$
ICCV2017 - Testing [53]	10°	$20\% \times min\{len(MT), len(GT)\}$

Toy example

Figure 2.28, table 2.3 show a dummy evaluation example for multiple symmetrical case. In the beginning, false positive should be ignored as in case of candidates (SC5, SC6) with considering only the high-ranked one (SC5) if the the following conditions both met: $\gamma^{SC_5,SC_6} < \gamma_T$ and $\zeta^{SC_5,SC_6} < \zeta_T$. The matching process between groundtruth and candidates is defined as follows:

— GT1 <–> SC1 as $\gamma^{GT_1,SC_1} < \gamma_T$ and $\zeta^{GT_1,SC_1} < \zeta_T$

6. https://sites.google.com/view/symcomp17/challenges/2d-symmetry

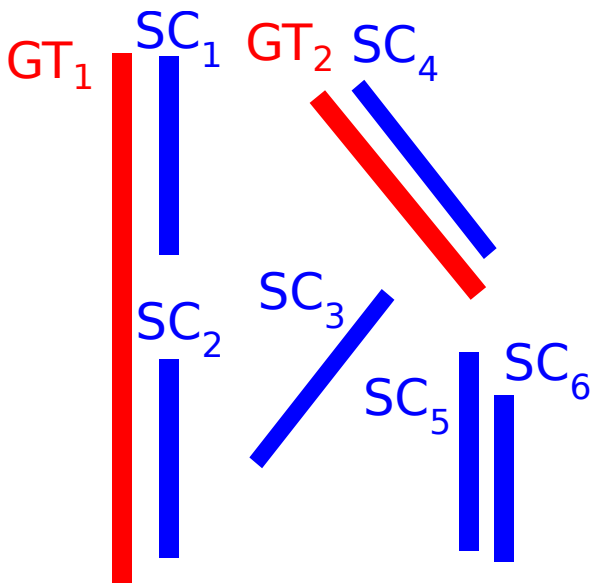

Figure 2.28 Toy example of multiple symmetry evaluation with two groundtruth (highlighted in red lines) and six axis candidates (highlighted in blue lines) produced and ranked by dummy detection algorithm.

— GT1 <–> SC2 as $\gamma^{GT_1,SC_2} < \gamma_T$ and $\zeta^{GT_1,SC_2} < \zeta_T$
— GT2 <–> SC4 as $\gamma^{GT_2,SC_4} < \gamma_T$ and $\zeta^{GT_2,SC_4} < \zeta_T$

As the performance measure of a candidate is defined (as defined in right-side of table 2.3) through the precision (index of true positive / rank index) and recall (index of true positive / number of groundtruth) rates. The precision-recall curves can be drawn through the values of the computed precision and recall rates, and we easily derive the value of $max\{F_1\}$ which is a excellent global measure to qualify a detection method.

Table 2.3 Numerical information of axis candidates for toy example.

Candidate	Score	Normalized Score	Rank	precision	recall	F1
SC1	0.8	1	1	1/1	1/2	0.667
SC2	0.7	0.875	2	1/2	1/2	0.5
SC3	0.6	0.749	3	-	-	-
SC4	0.3	0.375	4	2/4	2/2	0.667
SC5	0.1	0.125	5	-	-	-
SC6	0.05	0.063	6	x	x	x

2.3 Datasets

Public datasets of reflection symmetry detection are:

1. PSU (single, multiple): Liu's vision group [134, 95]proposed symmetry groundtruth for Flickr images (# images = # symmetries = 157 for single case, # images = 142 and # symmetries = 479 for multiple case) in ECCV2010 [1], CVPR2011 [2] and CVPR2013 [3]. Figure 2.29 shows different images of symmetrical cases with legend (r, c) representing row and column indexes. (1,4) case represents real and multiple example with similar objects defining inter and intra symmetries. (2,6) and (3,5) cases display real and single example with non-centered objects. (3,2) case shows multiple and real example defining inter symmetries. (5,2) case displays rotated and non-color example. (5,3) case shows an example of repetition of patterns with intra-symmetries. (6,5) case shows real and multiple example with non-similar objects.
2. NY datasets (single, multiple): Cicconet et al. [27] introduced a symmetry database (# images = # symmetries = 176 for single case, # images = 63 and # symmetries = 188 for multiple case) in 2016 [4], providing more stable groundtruth. Figure 2.30 shows single symmetrical cases (highlighting in white lines) under illumination conditions.
3. ICCV17 training datasets (single, multiple): Seungkyu Lee [53] delivered a challenge database associated with reflection groundtruth [5] (# images = # symmetries = 100 for single case, # images = 100 and # symmetries = 384 for multiple case). Figure 2.31 shows single and multiple symmetries (highlighted in blue lines) with indoor and close-up views.

Table 2.4 A summary of the proposed datasets for symmetry detection

Dataset	Single	Multiple
PSU	157	142 (479)
NY	176	63 (188)
ICCV17	100	100 (384)

All these public datasets have synthetic and natural images with focused and centered objects along side with clear background. There are other public datasets used by some works in limited way (BioID [78] for face detection, BSDS [109] for image segmentation, and

1. http://vision.cse.psu.edu/research/symmetryCompetition/index.shtml
2. http://vision.cse.psu.edu/research/symmComp/index.shtml
3. http://vision.cse.psu.edu/research/symComp13/content.html
4. http://symmetry.cs.nyu.edu/
5. https://sites.google.com/view/symcomp17/challenges/2d-symmetry

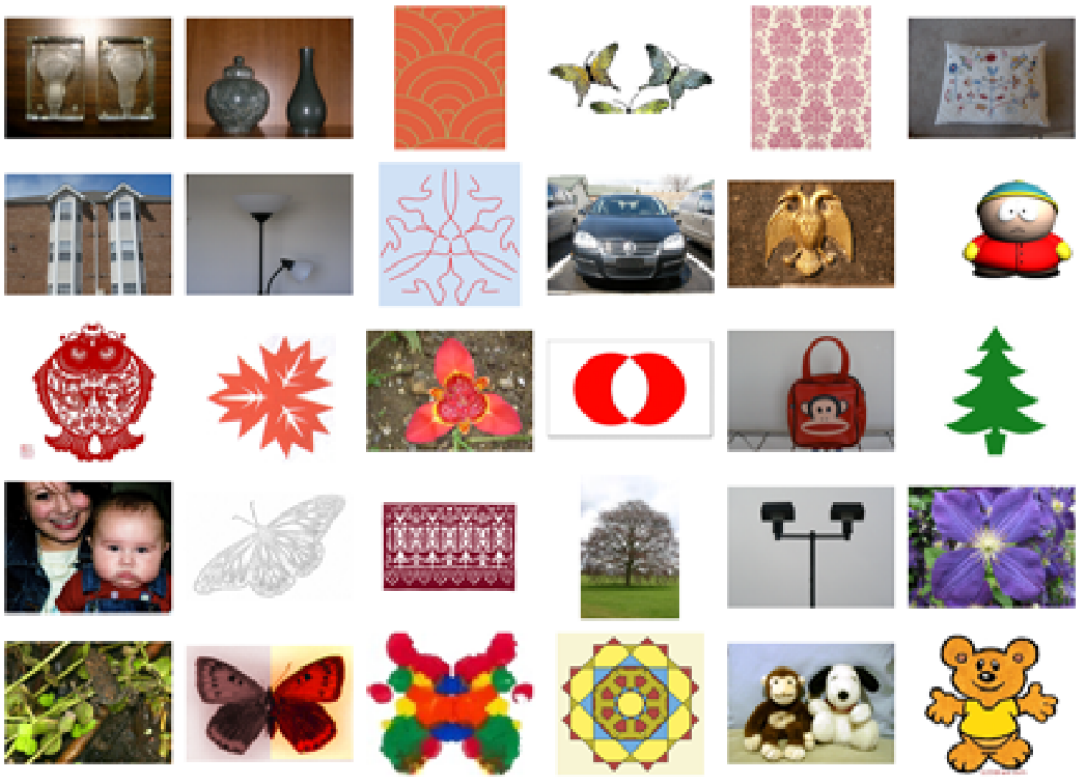

Figure 2.29 Sample images of PSU dataset. source: [134]

Figure 2.30 Sample groundtruth outputs from NY dataset. source: [27]

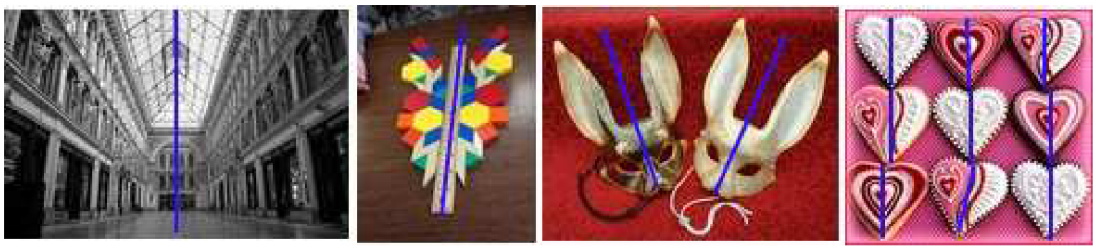

Figure 2.31 Sample groundtruth outputs from ICCV2017 dataset. source: [53]

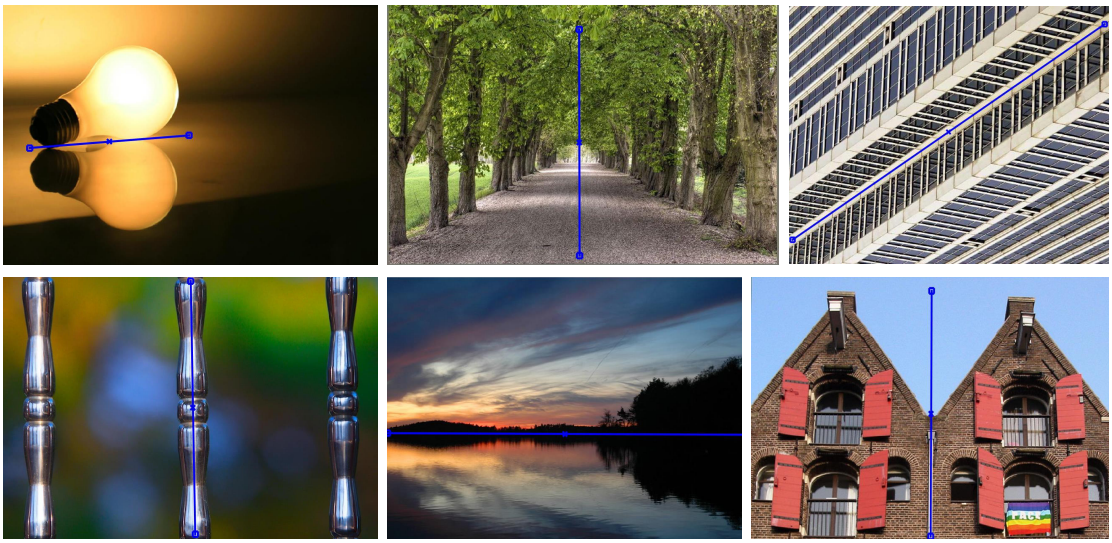

Figure 2.32 Examples of AvaSym images with single symmetry groundtruth.

COCO [94] for object detection). In the following subsection, we propose more challenging images with complex scenes, captured by amateur and professional photographers.

2.3.1 AvaSym dataset

From DPChallenge photo contest website, Murray et al. [119] introduced different annotations (aesthetic, semantic and photographic style) for more than 250,000 images for Aesthetic Visual Analysis "AVA". From the following photography challenges, we labeled global-axis symmetry groundtruth 'AvaSym' for 253 out of 878 images: (1) five challenges of "Reflections Without Mirrors": images containing bilateral representation without using mirror, (2) three challenges of "Symmetry": photographs composing symmetrical balance. These images are selected to neglect unclear instances of ambiguity symmetry, and to represent many comparison cases (non-centering viewpoint, perspective view, blurring reflection, etc.) for detection algorithms. Figure 2.32 shows some examples of single symmetries inside the proposed dataset (for more details, see appendix A).

2.4 Summary

In this chapter, we reviewed different categories of reflection symmetry detection (intensity, feature, segmentation and learning). Intensity-based needs a lot of time to compute mirror similarities in pixel-wise domain, plus prior knowledge about image objects. Feature-based is focusing on local keypoints instead of pixels for symmetry matching. Segmentation-based

splits an images into well-separated regions in order to define symmetries inside, this category provides skeletonized and non-connected axis candidates. Learning-based uses the advantages of recent machine learning algorithms (i.e. SVM, CNN) to implicitly discover symmetries inside well-annotated predefined scenes, which leads long training time to adapt the algorithms for desired outcome. In photographic analysis, our constraints are: (1) detection of the main symmetry axis and detection of several secondary ones. (2) address images encountered in photography (i.e. human made and natural scenes). (3) propose an efficient algorithm without requiring large annotated datasets. So we tackled these constraints through defining a detection pipeline combining local feature extraction and unsupervised learning. Moreover, the evaluation metrics of all previous competitions are unclear in the detailed evaluation of true and false positives and negative and how to compute the corresponding precision recall curves. The proposed work contains more challenging dataset (AvaSym) with global-wise symmetries to deduce among the participating algorithms through comparing the axis candidates with groundtruth in a single case.

Chapter 3

Symmetry Features and Metrics

Résumé: Dans ce chapitre, nous proposons une méthode pour détecter les axes globaux de symétrie par réflexion qui améliore la sélection des points-clés à partir des caractéristiques considérées ainsi que le calcul de leur pondération. Les ondelettes de Log-Gabor ont été introduites afin de détecter et extraire des caractéristiques d'image globales et efficaces. Nous combinons des histogrammes de couleurs et des histogrammes texturaux calculés dans un voisinage d'un point afin d'extraire des informations pertinentes de l'image permettant par la suite d'obtenir les axes de symétrie par réflexion. Nous montrons expérimentalement que la méthode proposée permet d'obtenir des résultats pertinents par rapport à l'état de l'art pour identifier les axes de symétries globaux dans des images comportant différentes scènes naturelles, que ce soit pour la recherche de l'axe de symétrie principal ou pour la recherche de plusieurs axes de symétries.

Abstract: We propose a method to detect reflection symmetries inside natural images in a global scale, through a novel selection of feature-of-interest keypoints and an enhanced computation of symmetric weights. We propose the use of Log-Gabor wavelets to detect and extract global and efficient image features. Moreover, combination of color and textural neighboring histograms exploits advantageous information regarding the image content, that can be used for an effective exploration of reflection axes inside an image. We show experimentally that the proposed work significantly recognize the global symmetries inside various image scenes of single and multiple cases.

3.1 Introduction

To detect symmetry inside an image, we need to explore objects' details which are symmetrically involved and evaluate how similar their structural information are in mirror way. For these reasons, we have to study the geometrical, textural, color properties

of distinguishable feature-of-interest patterns (i.e. edges, corners) that define the locally symmetric components. After that, we need to determine the balanced region based on symmetric metrics to match these patterns locally on each side of a symmetry axis candidate. In this chapter, we present the grid-based feature extraction using Log-Gabor wavelets in comparison with Gabor edge filters as in [28]. Then, we propose the application of these features to evaluate the symmetry contribution upon the construction of textural and color histograms, within computation of reflection symmetry axes. The provided evaluations confirm that the proposed work performs significantly better than the state-of-the-art methods [101, 28]. Moreover, on natural images it can detect global symmetries for better context analysis.

The rest of the chapter is organized as follows: the next section discuss the background of current symmetry detection methods and their limitations, plus defines the general steps of the proposed the framework. Section 3.3 describes our method to enhance the feature detection and extraction using Log-Gabor wavelets. Section 3.4 presents how to incorporate spatial and color representation into symmetrical weights using local textural and color histograms. Section 3.5 describes the implementation details and the results on different benchmark datasets along side with comparisons with state-of-the-art to be corrected alongside the document. Section 3.6 summarizes the proposed work with highlighting the future works.

3.2 Background and limitations of existing symmetry detection methods

State of the art symmetry detection methods use an approach based on the triptych: local feature extraction, symmetry measure, symmetry voting. The purpose of this section is to present the general algorithm used by theses methods together with their limitations.

3.2.1 General framework for symmetry detection

The main steps of general framework to detect globally the symmetry axes inside an image plane are:

1. Feature extraction: visual-based significant points p are detected and selected using some window-based derivative operation G from an image I, presenting consistent region-of-interest points over variant images of the same environment scene, plus invariant toward certain transformation and insensitive to noise.

$$p^i \leftarrow I * G \tag{3.1}$$
$$p^i = [p^i_x, p^i_y]^T,\ i = 1 \dots P \tag{3.2}$$

2. Feature triangulation: each pair of extracted points q_n are matched based on its feature characteristics, producing polar-based axis candidates (ρ for displacement,θ for angle) with respect to image origin O^I with reflection-based symmetrical weights ω_n.

$$q_n = (p^i, p^j, O^I),\ i \neq j,\ n = 1 \dots \frac{P(P-1)}{2} \tag{3.3}$$
$$q_n \rightarrow (\rho_n, \theta_n, \omega_n) \tag{3.4}$$

3. Symmetry representation: polar-based axis candidates (ρ, θ) are accumulated with respect the corresponding symmetrical weights ω_n, to construct a voting-based space with local maxima representing the best symmetrical axis candidates:

$$H(\rho, \theta, \omega) \leftarrow (\rho_n, \theta_n, \omega_n); \forall n \tag{3.5}$$

4. Symmetry selection: given the Hough-like voting space $H(\rho, \theta, \omega)$, the local maxima peaks SC^m are selected defining the major symmetry axes with well-defined endpoints (a^{SC^m}, b^{SC^m})

$$SC^m \leftarrow H(\rho, \theta, \omega) \tag{3.6}$$
$$SC^m = [a^{SC^m}, b^{SC^m}]^T,\ m = 1 \dots M \tag{3.7}$$

3.2.2 Limitations of current methods

In feature extraction, the baseline (Loy and Eklundh [101]) used sparse features based on SIFT methodology [100], while the state-of-art (Cicconet et al. [28]) used semi-dense features within the application of Gabor wavelet filters over grid-based image patches [55] and their applications in edge/contour extraction [74, 65, 79]. In section 3.3, we propose to use Log-Gabor function instead of Gabor ones, to extracts more accurate feature (edge/corner) information from an image, plus ensuring the robustness of these features with respect to linear illumination variations. In feature triangulation, the first baseline [101] uses SIFT

[100] descriptors as symmetrical weights, while the recent state-of-art [28] uses only the edge information for feature representation. In section 3.4, we propose to combine an edge based descriptors with color and textural information of local neighborhood. In voting-based symmetrical selection, both works [101, 28] use sparse-based voting scheme for hough-like weighting representation and conventional peak selection using classical non-maximal suppression method. In chapter 4 , we propose a continuous kernel estimation to represent the density of candidate pairs in polar coordinates of the symmetrical weights, and adapt mean-shift algorithm to find precisely the candidate axis.

3.3 Log-Gabor based feature detection and extraction

In this section, we present our feature detection method based on Log-Gabor filters. Log-Gabor filter was introduced by Field [49] in late 1980's, as an alternative to the Gabor filter, to suppress the effect of DC component through the computation of the multi-scale logarithmic function in the frequency domain. Feature extraction methods based on Log-Gabor filters have been successfully used in different computer vision applications (biometric authentication [81, 3], image retrieval [156], face recognition [92], image enhancement [160], vehicle detection [6], character segmentation [105], and edge detection [57]).

The reason of selecting Log-Gabor wavelets over Gabor ones is shown inside figure 3.1, in which Log-Gabor minimizes the DC component (enhancing the contrast ridges and edges of images) through the natural behavior of logarithmic function, and separates the frequency bands through splitting the common coverage areas between them at cut-off frequency $10\log_{10}(\frac{1}{2}) \simeq -3dB$. While the Gabor over-represents the high frequencies components and under-represents the low frequencies. In addition, figure 3.2 presents that even scales in Log-Gabor are rotated by half distance between the filter centers of the prior odd scales, to cover the Fourier space better than Gabor. Figure 3.3 shows Gabor and Log-Gabor wavelet filter bank with 4 scales and 5 orientations, which the elongation scheme of Log-Gabor wavelets appears in the real and imaginary components in the spatial domain. Figure 3.4 shows the difference in wavelet response between Gabor and Log-Gabor on some natural image with a different illuminated foreground leaf along side with a blurring background. The amplitude maps illustrate that Log-Gabor filters are not sensitive to linear background variations by highlighting the details of the focused object only, unlike Gabor filters. We can summerize that the Log-Gabor functions are better analyzed in natural images than Gabor ones.

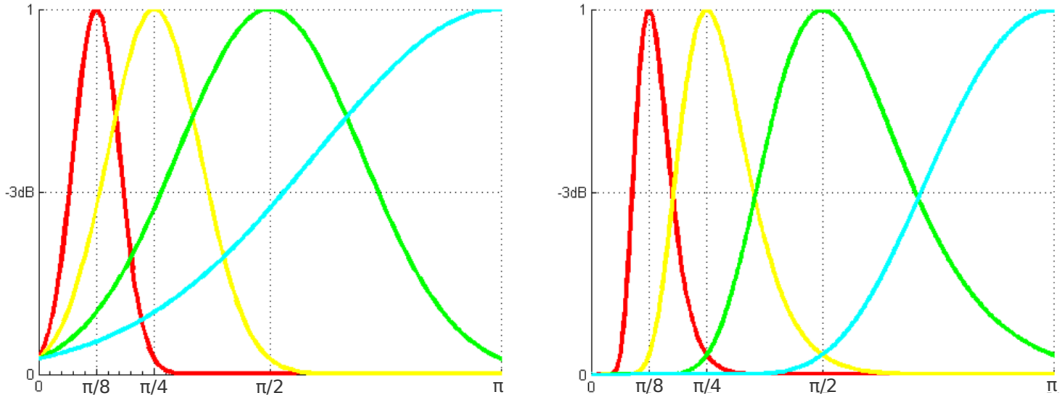

(a) Gabor (b) Log-Gabor

Figure 3.1 Frequency responses of (a) Gabor and (b) Log-Gabor wavelets at 4 angular frequency bands. Source: [124].

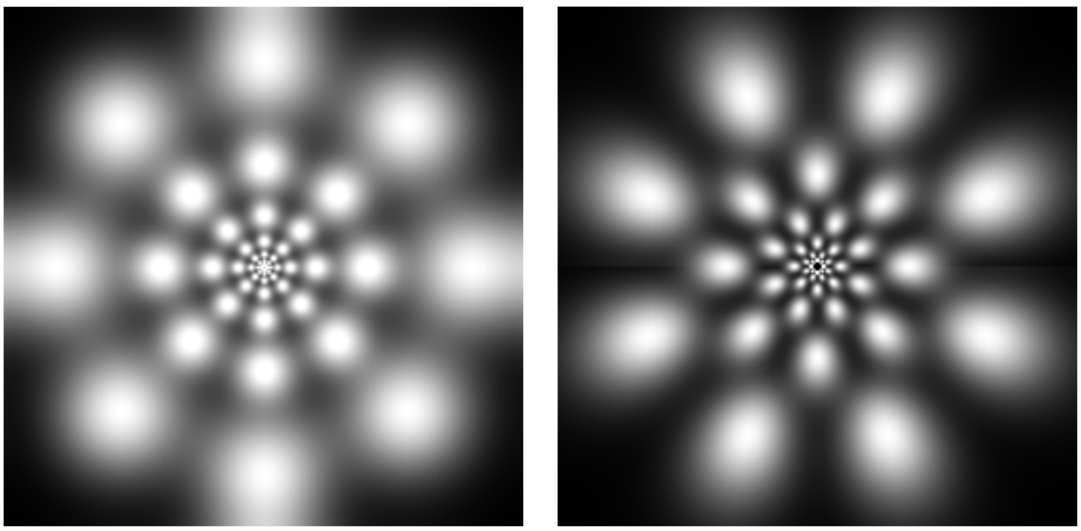

(a) Gabor (b) Log-Gabor

Figure 3.2 Multiscale complex filter banks of (a) Gabor and (b) Log-Gabor with 8 orientations and 6 scales. Note that Log-Gabor covers the response space in better way by rotating half distance between filter centers at each scale, see equation 3.17. Source: [124].

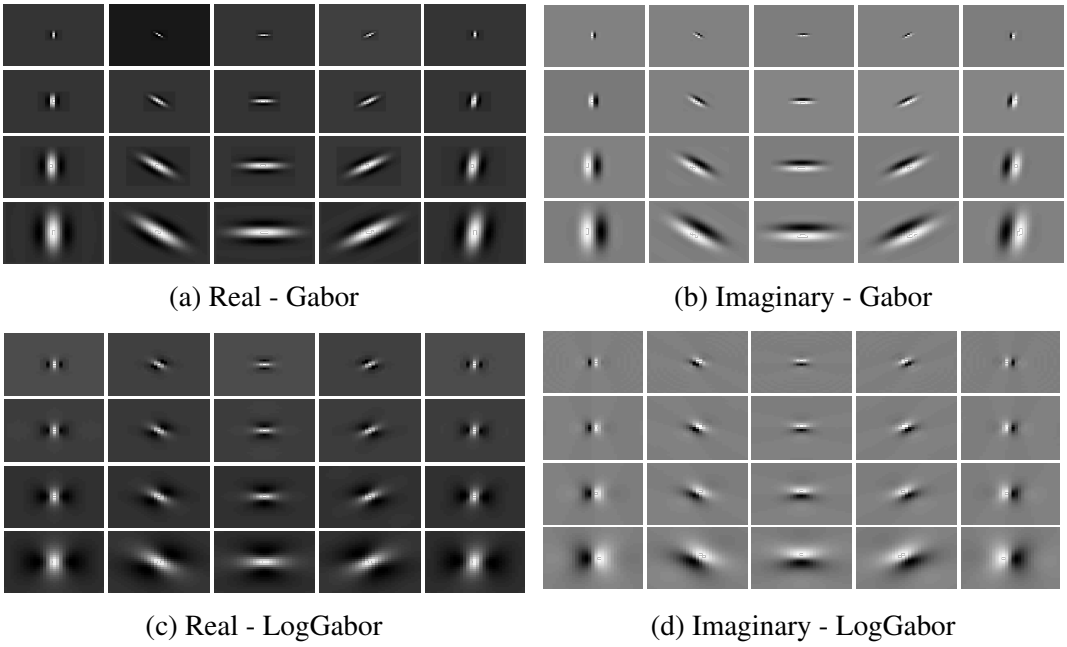

(a) Real - Gabor (b) Imaginary - Gabor

(c) Real - LogGabor (d) Imaginary - LogGabor

Figure 3.3 Multi-resolution Gabor and Log-Gabor arrangements with $S = 4$ scales (in rows) and $O = 5$ orientations (in columns). Real (a,c) and imaginary (b,d) components are displayed in the spatial domain.

Gabor filters

The Gabor (as known as Morlet) wavelet parameters can be specifically tunned to detect edges. For that, the reference angular frequency is $\omega_0 = \pi/2$, and the elongation along the main orientation is half value of its orthogonal. Formally, the mother wavelet $\psi(x,y)$ is defined as:

$$\psi(x,y) = \exp(\omega_0 jx) \;\; \exp(-\frac{1}{2}|diag(1,\frac{1}{2}) \times [x,y]^T|^2) \tag{3.8}$$

where $\times$ denotes the matrix product operator, and its Fourier transform is given by:

$$\hat{\psi}(\omega_x,\omega_y) = \frac{1}{\sqrt{2\pi}} \exp\left(-\frac{|[\omega_x,\omega_y] - \omega_0|^2}{2}\right) \tag{3.9}$$

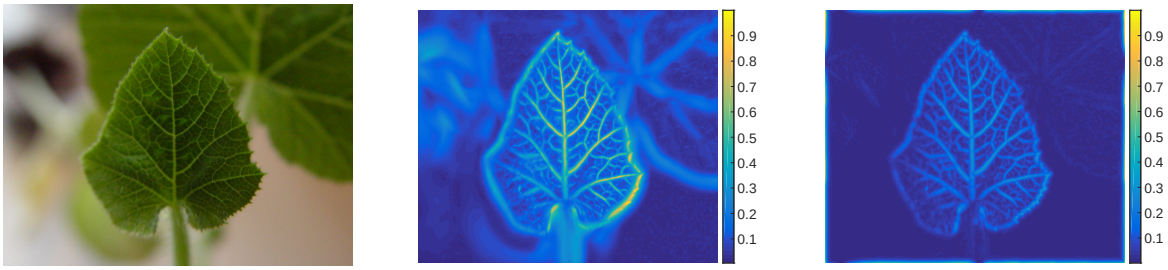

(a) Input (b) Amplitude - Gabor (c) Amplitude - LogGabor

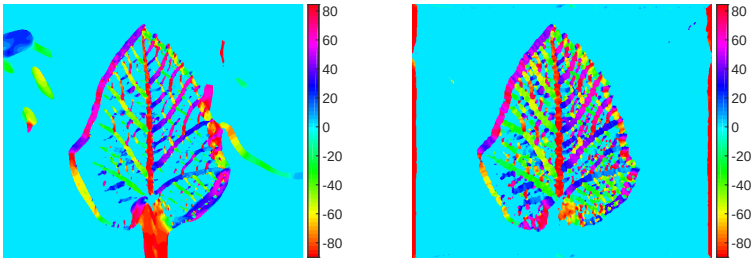

(d) Orientation - Gabor (e) Orientation - LogGabor

Figure 3.4 Comparison of amplitude and its corresponding orientation responses between Gabor (b,d) and Log-Gabor (c,e) filters for some input (a). Note that Log-Gabor is less sensitive to linear background variations.

The Gabor wavelet family of functions $\psi_{s,o}(x,y)$ of scale $s \in \{1,\ldots,S\}$ and orientation $\alpha_o = \frac{o\pi}{O}$ with $o \in \{0,\ldots,O-1\}$ is:

$$\psi_{s,o}(x,y) = \frac{1}{s}\psi\left(\frac{\Omega_o \times [x,y]^T}{s}\right) \tag{3.10}$$

$$\Omega_o = \begin{bmatrix} \cos(\alpha_o) & \sin(\alpha_o) \\ -\sin(\alpha_o) & \cos(\alpha_o) \end{bmatrix} \tag{3.11}$$

The corresponding Fourier transform of $\psi_{s,o}$ is given by:

$$\hat{\psi}_{s,o}(\omega_x,\omega_y) = s\frac{1}{\sqrt{2\pi}}\exp\left(-\frac{s^2|\Omega_o \times [\omega_x,\omega_y]^T - \omega_0/s|^2}{2}\right) \tag{3.12}$$

In this last equation, the two properties of Gabor wavelets are expressed in the frequency domain as in figures (3.1 and 3.2). At first, for $\alpha_o = 0$, the Fourier transform of wavelets have a Gaussian shape whose center is located at ω_0/s and their bandwidth are proportional to $1/s$ which explains figure3.1. Second, at a fixed scale s, the Gaussian centers are located on a circle whose size is inversely proportional to s and they are radially located over angles α_o as seen on figure 3.2.

The response of wavelet coefficients $I_{s,o}(x,y)$ are computed on an image I (width W and height H), up on application of Gabor filters $\psi_{s,o}$ in the spatial domain over multiple scales and orientations as follows:

$$I_{s,o}(x,y) = |I \circledast \psi_{s,o}| \tag{3.13}$$

where $\circledast$ denotes the 2D convolution operation.

Log-Gabor filters

Inspired from Kovesi's work [87, 88] in computing phase congruency, the key idea of Log-Gabor filters is to define them in the Fourier space. The 2D frequency vector $[\omega_x, \omega_y]$ is represented in polar coordinates by a radial variable denoted μ and an angle denoted β. The Fourier transform of this filter is then the product of a radial component which is a Gaussian function of the logarithm of the radial frequency μ and an angular term which is a Gaussian function of the angle frequency β. Formally, given the scales $s \in \{1,\ldots,S\}$ and orientations β_o with $o \in \{0,\ldots,O-1\}$, the Fourier transform of Log-Gabor filters is given by:

$$\ddot{G}(\mu,\beta;s,o) = \ddot{G}_s(\mu)\, \ddot{G}_o(\beta) \tag{3.14}$$

$$\ddot{G}_s(\mu) = \exp(-\frac{(log(\frac{\mu}{\mu_s}))^2}{2(log(\lambda_\mu))^2})\, U(\mu) \tag{3.15}$$

$$\ddot{G}_o(\beta) = \exp(-\frac{|\beta-\beta_o|^2}{2\lambda_\beta^2}) \tag{3.16}$$

$$\beta_o = \begin{cases} \frac{o\pi}{O} + \frac{\pi}{2O}, & S = odd \\ \frac{o\pi}{O}, & S = even \end{cases} \tag{3.17}$$

$$\mu_s = \frac{1}{\Gamma \Lambda^{s-1}} \tag{3.18}$$

where Γ is the wavelength of the smallest scale filter, and Λ is the scaling factor between successive filters. (μ_s, β_o) are the frequency centers and their bandwidths $(\lambda_\mu, \lambda_\beta)$. $\ddot{G}_s(\mu)$ is multiplied by low-pass Butterworth filter $U(\mu)$ [126] (order 15, and radial frequency $0.45 \times 2\pi$), to eliminate any extra frequencies at Fourier corners.

The modulus of complex wavelet coefficients $I_{s,o}(x,y)$ are computed on an image I (width W and height H) as follows:

$$I \underset{GS}{\rightarrow} I_{GS} \overset{FT}{\rightarrow} \ddot{I}_{GS} \rightarrow \ |\ddot{I}_{GS}\, \ddot{G})|^{FT^{-1}}_{\rightarrow}\ I_{s,o} \tag{3.19}$$

$$I_{s,o}(x,y) = |(I_{GS} \circledast G)\ (x,y)| \tag{3.20}$$

where I_{GS} is the gray-scale version of the image I in frequency domain, and $FT(.)$, $FT^{-1}(.)$ are the Fourier transform and its inverse.

Edge characteristics

At each image location, amplitude $J(x,y)$ and its corresponding orientation $\phi(x,y)$ maps are deduced by seeking for the maximum response $I_{s,o}(x,y)$ across scales and orientations:

$$J(x,y) = \max_{s,o} I_{s,o}(x,y) \tag{3.21}$$

$$\phi(x,y) = \arg(\max_{s,o} I_{s,o}(x,y)) \tag{3.22}$$

Either using Gabor or Log-Gabor filters in figure 3.4, these maps highlight the edge details of the foreground object in a sharp way.

Feature extraction

Upon a spatial sampling of the input image I (see figure 3.5) using non-interleaved cells along a regular grid (stride and cell size are proportional to the maximum image dimension $\max(W,H)$). Each feature point p^i is extracted (as presented in figure 3.6) within each cell D_i as the point in that cell where the wavelet response is maximum. The maximum wavelet response is denoted $J_i = J(p^i)$ along side with the corresponding orientation ϕ_i and color information υ_i in HSV color space.

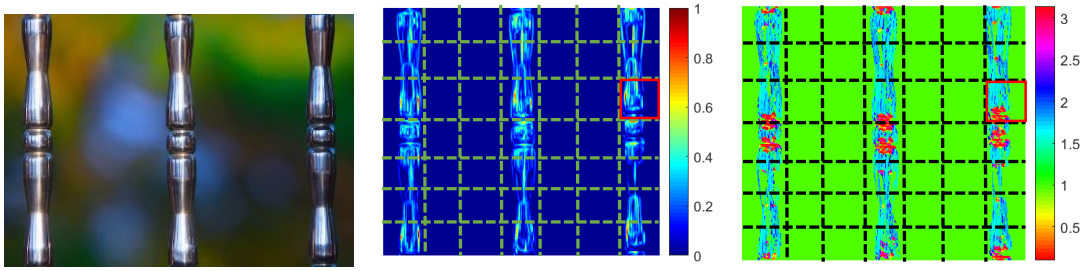

(a) Input (b) Amplitude with Cell D_i (c) Orientation ϕ with Cell D_i

Figure 3.5 An illustration of grid-based sampling process. (a) input image I. (b,c) amplitude J and orientation ϕ maps with non-interleaved griding presentation (using green dashed lines) plus highlighted cell D_i (inside red square).

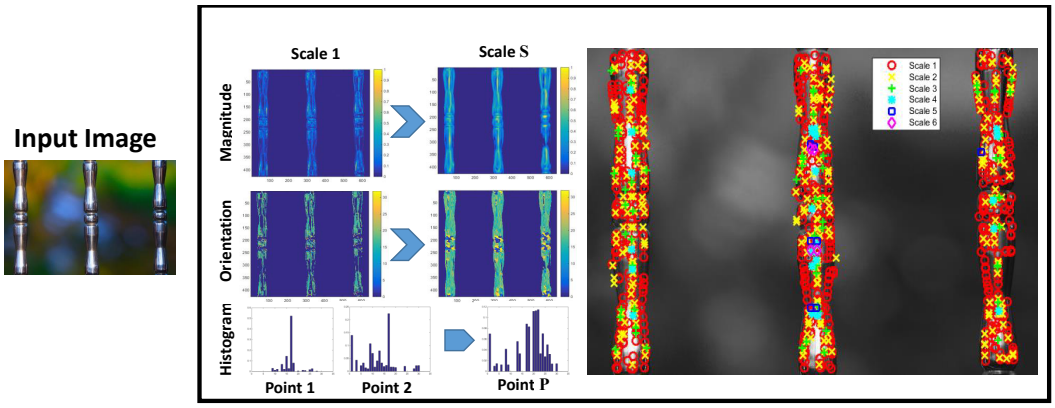

Figure 3.6 An example of feature extraction with different scales, accompanied with edge and textural characteristics (for better display, only features with high magnitude are displayed over the gray-scale version of the input image).

3.4 Local symmetry measure

Once the local features are extracted, we need to define descriptors for each feature and combine them in such way to have well-defined symmetrical representation. The first baseline [101] used the neighboring information through SIFT [100] descriptors, while the recent state-of-art [28] used the magnitudes of the edge segments only for feature representation. Our idea is combining edge magnitudes along side with local neighborhood information. The principle of the proposed symmetrical representation relies in the following three steps:

1. Local description of textural and color information around each feature points.
2. Computation of symmetry similarity to find out how the given pairs of the feature points are mirror matched.
3. The voting comprises the accumulation of the contribution of each pair to a given axis in a Hough-like space, to select the symmetrical peaks. It will be explained in details in section 4.2 of the next chapter.

Local description

Textural and color descriptors are one of the most significant visual features, and have been used efficiently in different applications of computer vision (object recognition [154], and image retrieval [131, 106]). The textural and color information around an edge segment are prominent similarity characteristics for natural images, describing the symmetrical behavior of local edge orientation, and the balanced distribution of luminance and chrominance components. Hence, we introduce two histograms: Firstly as shown in figure 3.7, neighboring

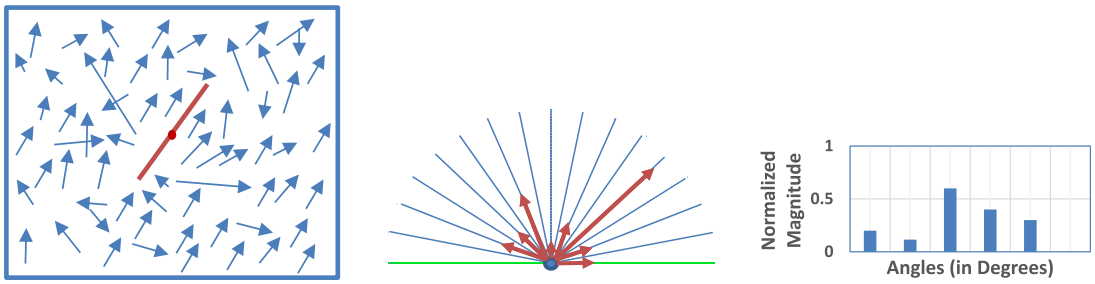

(a) (b) (c)

Figure 3.7 The process of computing local orientation histogram: (a) Edge segments arrangement within a cell, (b) angular distribution of edge segments for 16 main orientations over 180 degrees, (c) normalized neighboring orientation histogram.

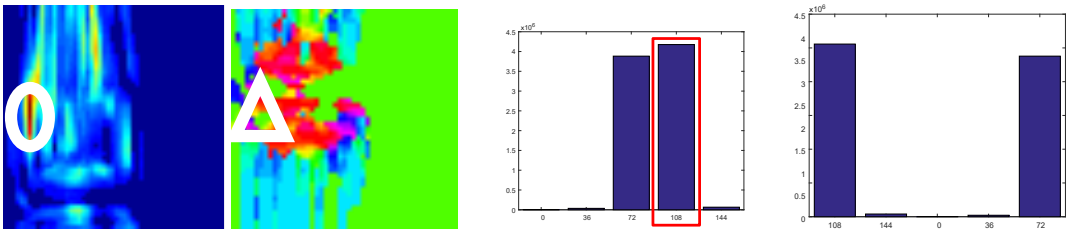

(a) Amplitude and Orientation Cells (b) Histogram (c) Shifted Histogram

Figure 3.8 An illustration of histogram circular shift process. (a) Zoom-in details of amplitude and orientation information of cell D_i from sub-figure 3.5c, highlighting the maximum magnitude J_i with white circle in the left map (amplitude) and its corresponding angle ϕ_i with white triangle in the right map (orientation). (b,c) textural histogram h^i is circular shifted respect to the orientation ϕ_i of the maximum magnitude J_i, highlighting this orientation as red rectangular box.

textural histogram h^i of size L:

$$h^i(l) = \sum_{r \in D_i} J_r \, \mathbb{1}_{\Phi_l}(\phi_r), \tag{3.23}$$

$$\Phi_l = [\frac{l\pi}{L}, \frac{(l+1)\pi}{L}[, \; l = 0, \ldots, L-1$$

where $\mathbb{1}$ is the indicator function. For the sake of a rotation-invariant representation, h^i is circular shifted with respect to the orientation ϕ_i of the maximum magnitude J_i among the neighborhood cell D_i, as shown in figure 3.8. The proposed textural histogram h^i is similar to HOG method [37] giving edge amplitude over each orientation bin Φ_l.

Secondly, the local HSV histogram g^i of size C with sub-sampling rate ($C^{hu} : C^{sa} : C^{va}$) is computed based on the previous work in MPEG-7 standard [106]. The HSV color space is a well-known choice for color descriptors to represent color details in an image, by simulating how humans perceive color information. The HSV histogram g^i is as follows:

$$g^i(c) = \sum_{r \in D_i^*} \mathbb{1}_{\Upsilon_c}(\upsilon_r), \tag{3.24}$$

$$\begin{aligned} c &= (c^{hu}, c^{sa}, c^{va}), \\ c^{hu} &\in \{0, \ldots, C^{hu} - 1\}, \\ c^{sa} &\in \{0, \ldots, C^{sa} - 1\}, \\ c^{va} &\in \{0, \ldots, C^{va} - 1\}, \end{aligned}$$

$$\Upsilon_c = [\frac{2c^{hu}\pi}{C^{hu}}, \frac{2(c^{hu}+1)\pi}{C^{hu}}[\times [\frac{c^{sa}}{C^{sa}}, \frac{c^{sa}+1}{C^{sa}}[\times [\frac{c^{va}}{C^{va}}, \frac{c^{va}+1}{C^{va}}[$$

where D_i^* is the neighborhood window around feature point p^i, υ_c is a sub-sampled set of HSV space, in terms of three components: hue (hu), saturation (sa) and value (va). $l1$ normalization is applied to $g^i(.)$ and $h^i(.)$, to prevent the effect of contrast and illumination variations in bin-wise histogram comparisons.

Symmetry similarity

As shown in figure 3.9, a set of feature pairs $\{q_n = (p^i, p^j) \mid n = 1, \ldots, N\}$ are elected such that $i \neq j$, P is the number of feature points, $N = \frac{P(P-1)}{2}$ is the number of feature pairs, T_{ij} is the line passing through p^i and p^j, $c^{ij} = (c_x^{ij}, c_y^{ij})$ denotes the center of (p^i, p^j) segment, and $\overrightarrow{o}$ is the reference unit vector of x-axis of the Cartesian plane. Then, we compute the symmetry candidate axis $T_{ij}^{\perp}$ (line perpendicular to (p^i, p^j) segment passing through c^{ij}) based on a triangulation process with respect to the image origin $c_{W,H} = (\frac{W}{2}, \frac{H}{2})$. This candidate axis is parametrized by angle $\theta_{i,j}$ (orientation of the bisector of the pair segment (p^i, p^j)), and displacement $\rho_{i,j} = c_x^{ij} cos(\theta_{i,j}) + c_y^{ij} sin(\theta_{i,j})$ (distance of the image origin to this bisector) and has a symmetry weight $\omega_n = \omega_{i,j}$ defined as follows:

$$\omega_{i,j} = \omega(p^i, p^j) = S_E(i,j)\, S_T(i,j)\, S_C(i,j) \tag{3.25}$$

$$S_E(i,j) = J_i J_j |\tau^i R(T_{ij}^{\perp}) \tau^j| \tag{3.26}$$

$$S_T(i,j) = \sum_{n=1}^{N} min(h^i(n), \tilde{h}^j(n)) \tag{3.27}$$

$$S_C(i,j) = \sum_{c=1}^{C} min(g^i(c), g^j(c)) \tag{3.28}$$

$$R(T_{ij}^{\perp}) = \begin{pmatrix} -\cos(2\theta_{i,j}) & -\sin(2\theta_{i,j}) \\ -\sin(2\theta_{i,j}) & \cos(2\theta_{i,j}) \end{pmatrix}$$

where $\tau^i = [cos(\phi_i), sin(\phi_i)]^T$, $R(T_{ij}^{\perp})$ is the reflection matrix with respect to the perpendicular of the line connecting (p^i, p^j) [28, 44], and $\tilde{h}^j$ is the mirror version of h^j histogram for element-wise orientation-based comparison. $l1$ normalization is applied to symmetry weights ω. $S_E(i,j)$ is firstly defined in [28] and represents mirror symmetry coefficient based on how close are the global orientations of the pair edges, multiplied by the magnitudes of these edges. While we preserve the neighborhood contents around the pair edges by defining $S_T(i,j)$ and $S_C(i,j)$ to be similarity measures between local texture and color histograms respectively.

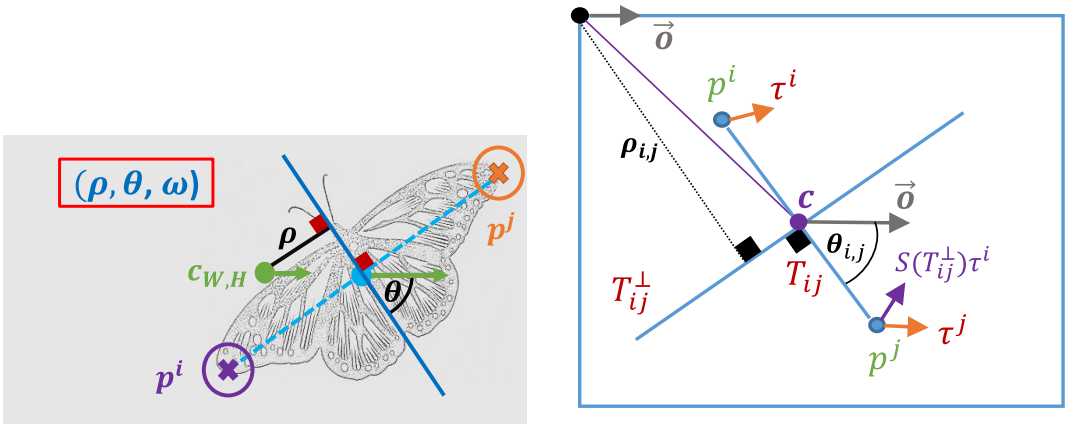

(a) (b)

Figure 3.9 Pairwise symmetry triangulation: (a) Simplified illustration within an image, (b) geometrical explanation.

Symmetry voting

Up on the computation of symmetrical similarity for each axis candidate, the major symmetry peaks are selected through a weighted accumulation of the involved candidates,

followed by a refinement process of the spatial boundaries of each symmetry axis. The next chapter will discuss this step in details.

3.5 Results

In this section, we will explain the configuration settings and parameters selection to conduct the detection experiments, followed by the performance study (visually and statistically) of the proposed work against state-of-art algorithms.

3.5.1 Experimental settings

State-of-the-art approaches: Loy and Eklundh (*Loy*) [101] and Cicconet et al. (*Cic*) [28] are compared in table 3.1, against the different variants of the proposed work: *GbT*, *LgT*, and *LgTC*. *GbT* uses Gabor filters for feature extraction and the global orientation information along side with textural similarity measure to represent the symmetrical weights. *LgT* updates only feature extraction by using Log-Gabor filters instead of Gabor ones. *LgTC* enhances *LgT* by adding the color similarity measure into the symmetrical weights. The source codes of state-of-the-art algorithms are used with default parameter values and are compared at most first 50 axis candidates for fair performance evaluation. In Gabor and Log-Gabor edge detections, we set the number of scales S and number of orientations O to 12 and 32. We also set the radial bandwidth λ_μ to 0.55, the angular bandwidth λ_β to 0.2, the minimum wavelength Γ to 6, and the scaling factor Λ to 1.2. In textural and color histogram calculations, we define the number of bins for textural L and color C to 32 and 32 (sampling rate $C^{hu} : C^{sa} : C^{va} = 8 : 2 : 2$) respectively. We choose those parameters on the basis of extensive experiments. In case of gray-scale images, contrast values are used instead of color information in *HSV* color space.

3.5.2 Performance analysis

In our experimental evaluation, the algorithms are executed to detect and compare the global symmetries inside synthetic and real-world images. Tables 3.2 shows the true positive rates for the proposed methods (*GbT*, *LgT*, and *LgTC*) against Loy and Eklundh (*Loy*) [101], and Cicconet et al. (*Cic*) [28]. *LgTC* performs the best result among most cases in single and multiple symmetry, due to the importance of color information for the voting computations in colorful images. At the same time, *LgT* has the top 2nd result, and sometimes the top 1st results in gray-scale or low-saturated images, thanks for the use of the bank of Log-Gabor filters in the feature extraction step. *GbT* ranked as the top 3rd result, due to the utilization of

Table 3.1 Implementation details of the state-of-art algorithms along side with the proposed work, showing the main contributions of each algorithm in two aspect: feature detection & extraction, and symmetrical weights.

Algorithms	Detection & Extraction			Weights		
	SIFT	Gabor	Log-Gabor	Edge	Textural	Color
Loy [101]	✓			✓		
Cic[28]		✓		✓		
GbT		✓		✓	✓	
LgT			✓	✓	✓	
LgTC			✓	✓	✓	✓

Table 3.2 Using evaluation metrics **CVPR2013** [95] (table 2.2), comparison of the true positive rates based on top detection for the proposed methods against the state-of-art algorithms. Symmetry datasets are presented as: single-case (first 4 rows) and multiple-case (last 3 rows), highlighted between (parenthesis) the number of images for each dataset. The last row represents sum of true positive rates among all datasets. Top 3 results are in **Bold** with **red**, **blue** and **green** colors respectively.

Datasets	*Loy* [101]	*Cic* [28]	*GbT*	*LgT*	*LgTC*
PSU (157)	81	90	**97**	**104**	**113**
AVA (253)	**174**	124	170	**188**	**182**
NY (176)	98	92	**109**	**124**	**135**
ICCV17 (100)	**52**	**53**	**52**	**70**	**70**
PSUm (142)	69	68	**67**	**72**	**75**
NYm (63)	32	**36**	**36**	**38**	**40**
ICCV17m (100)	**54**	39	**52**	**52**	**57**
Total (991)	560	502	**583**	**648**	**672**

small grids to compute window-based features as textural weights. Thanks for the advantage of SIFT features, *Loy* [101] is still strong competent to be ranked as the top 4th result in general. *Cic* [28] has the lowest performance.

Figure 3.10 presents performance results in terms of precision and recall curves for single-case and multiple-case symmetry datasets, plus the values of the maximum F1 scores in table 3.3 to measure the performance of the proposed algorithms (*El*, *LgT*, and *LgTC*) against Loy and Eklundh (*Loy*) [101], and Cicconet et al. (*Cic*) [28]. In single-case symmetry, our method *LgT* outperforms the other concurrent algorithms (*Loy*, and *Cic*) in the context of using only gray-scale version of involved images. Furthermore, color version of our method

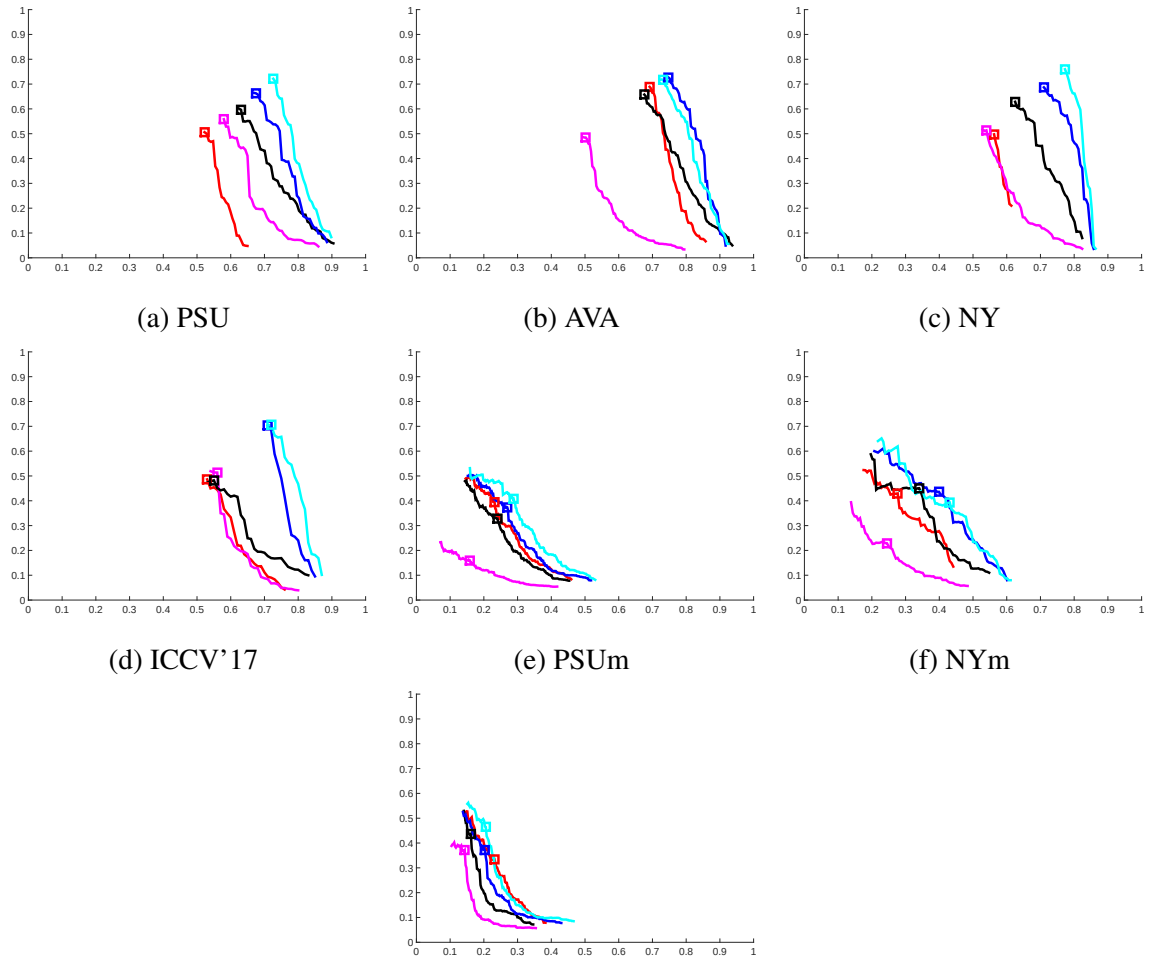

(a) PSU (b) AVA (c) NY

(d) ICCV'17 (e) PSUm (f) NYm

(g) ICCV'17m

Figure 3.10 Using evaluation metrics **CVPR2013** [95] (table 2.2), Precision-Recall curves on: (1) four single-case symmetry (a,b,c,d) datasets, and (2) three multiple-case symmetry (e,f,g) datasets to show the overall superior performance of our proposed methods: ***GbT*** **(black)**, ***LgT*** **(blue)**, and ***LgTC*** **(cyan)**; against the prior algorithms: ***Loy*** **(red)** [101], and ***Cic*** **(magenta)** [28]. The maximum F1 scores are qualitatively presented as square symbols along the curves, and quantitatively indicated between parentheses in table 3.3. (x-axis: Recall, y-axis: Precision).

LgTC exploits slightly improvement over gray-scale one *LgT*. On the other hand, Only *LgTC* has better precision performance among others in (*PSUm* and *NYm*) datasets, due to many local groundtruth presenting inside multiple-case symmetry. In *ICCV2017m* dataset, *Loy* has better precision performance at some intermediate recall rates, for the purpose of detecting minor or skeleton axes defined as symmetry groundtruth inside some image objects. In average summary, *LgTC* has the best efficiency results to handle symmetries with all dataset

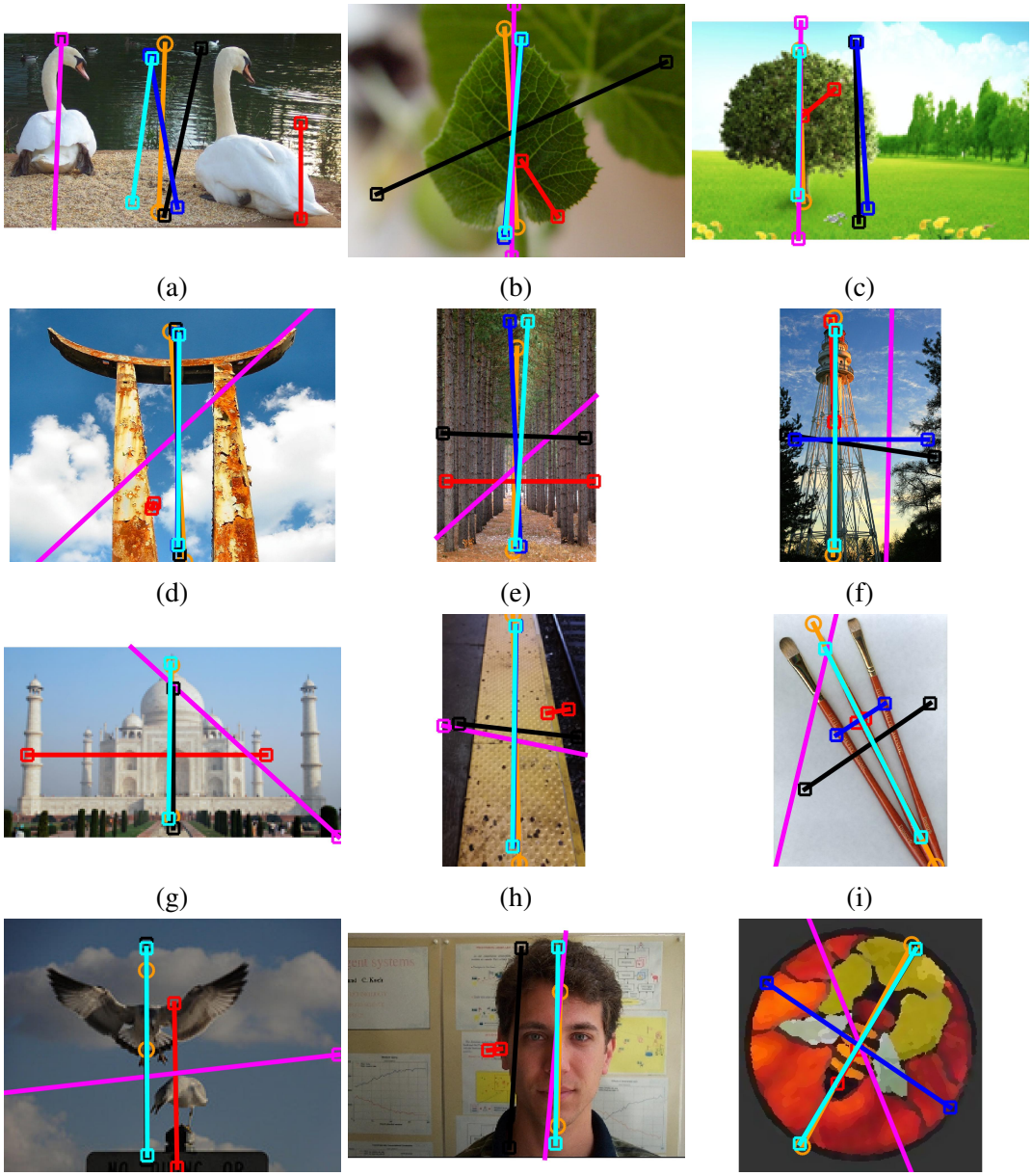

Figure 3.11 Some single-case results from PSU [134, 95], NY [27], AVA [44], and ICCV [53] datasets, with *groundtruth (orange)*, state-of-art methods: *Loy (red)*, and *Cic (magenta)* axes against the proposed methods: ***GbT* (black)**, ***LgT* (blue)**, and *LgTC* (cyan). Each symmetry axis is shown in a straight line with circular and squared endpoints for groundtruth and methods respectively.

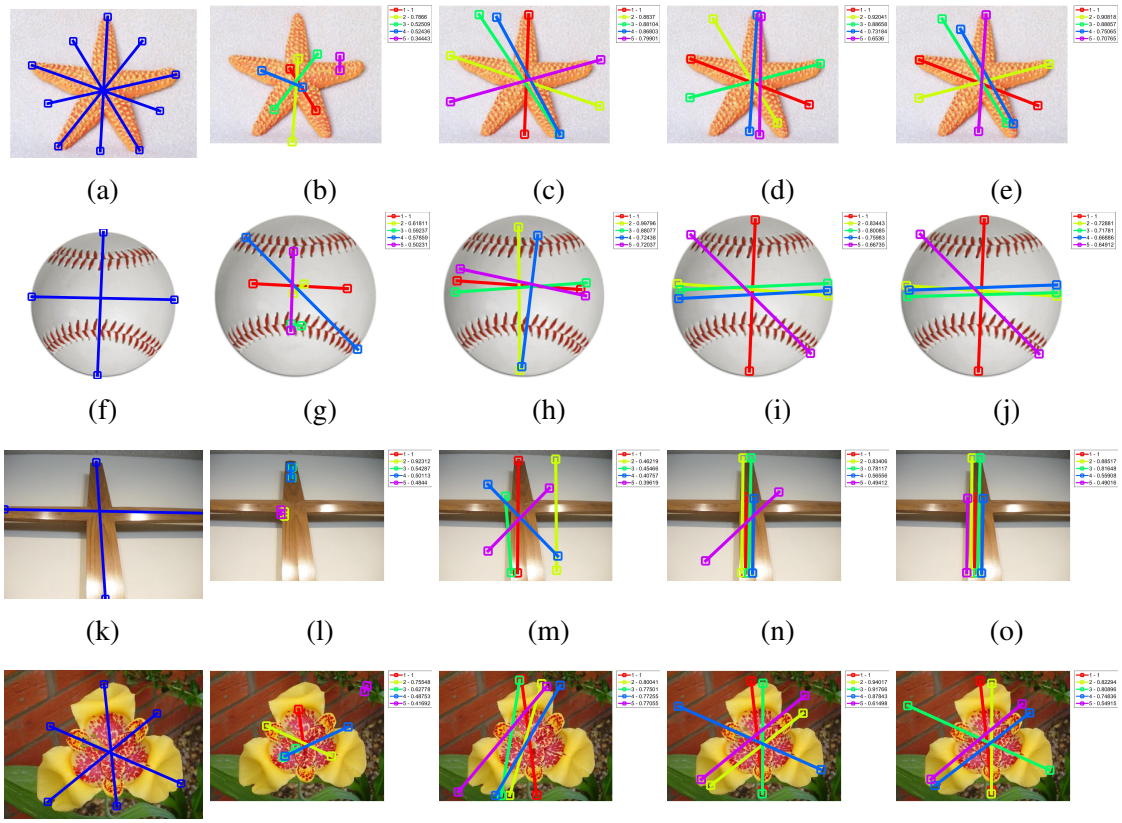

Figure 3.12 Some multiple-case results from PSUm [134, 95], NYm [27], and ICCVm [53] datasets, with ***groundtruth (blue)*** in 1st column (a-p). Thanks to textural weights, the proposed methods: ***GbT*** in 3rd column (c-r), ***LgT*** in 4th column (d-s), and ***LgTC*** in 5th column (e-t); produce higher accuracy results against the baseline ***Loy*** in 2nd column (b-q). For each algorithm, the top five symmetry results is presented in such order: ***red***, ***yellow***, ***green***, ***blue***, and ***magenta***. Each symmetry axis is shown in a straight line with squared endpoints.

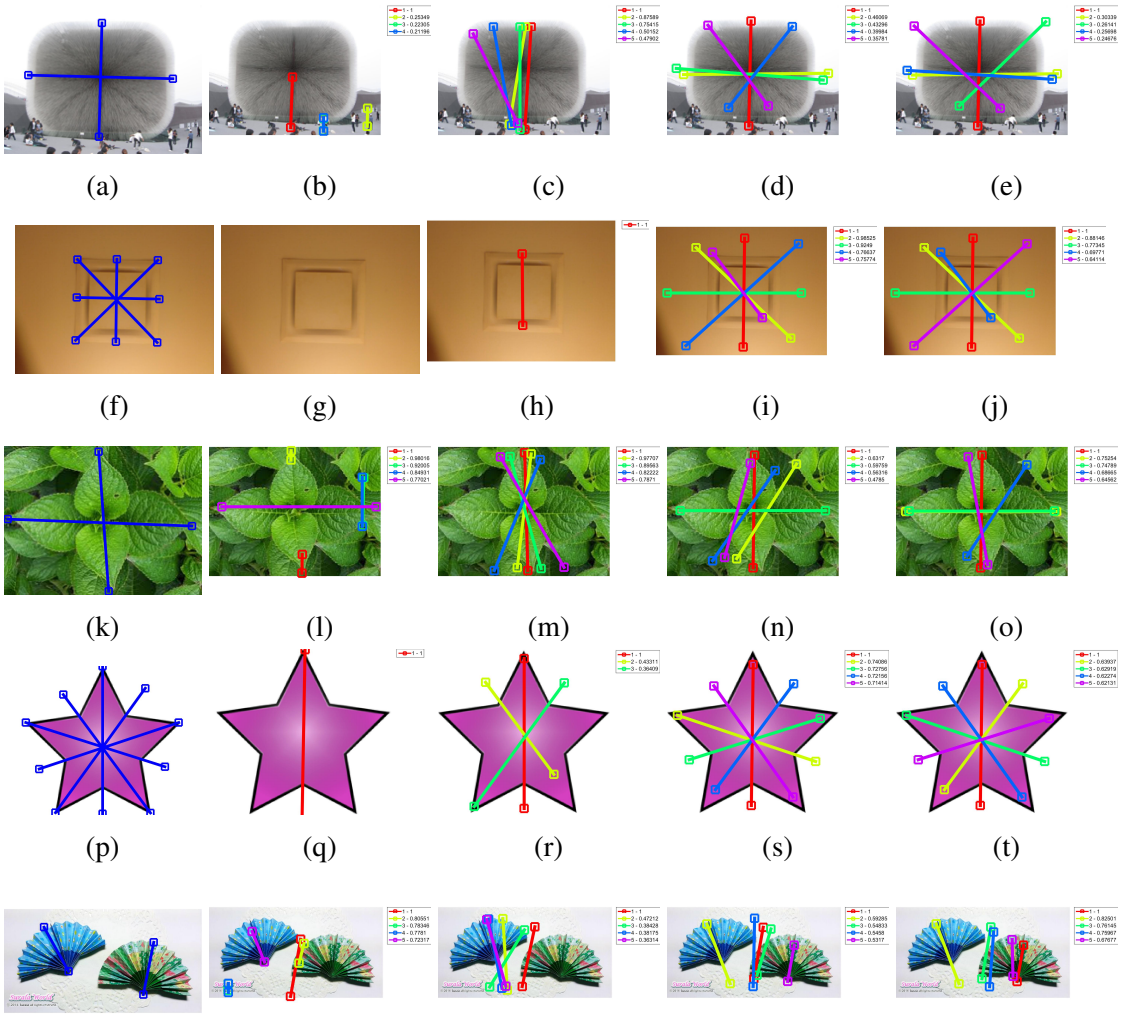

Figure 3.13 Some multiple-case results from NYm [27], and ICCVm [53] datasets, with ***groundtruth (blue)*** in 1st column (a-u). Thanks to Log-Gabor feature extraction and color weights, the proposed methods: ***GbT*** in 3rd column (c-w), ***LgT*** in 4th column (d-x), and ***LgTC*** in 5th column (e-y); produce higher accuracy results against the baseline ***Loy*** in 2nd column (b-v). For each algorithm, the top five symmetry results is presented in such order: ***red***, ***yellow***, ***green***, ***blue***, and ***magenta***. Each symmetry axis is shown in a straight line with squared endpoints.

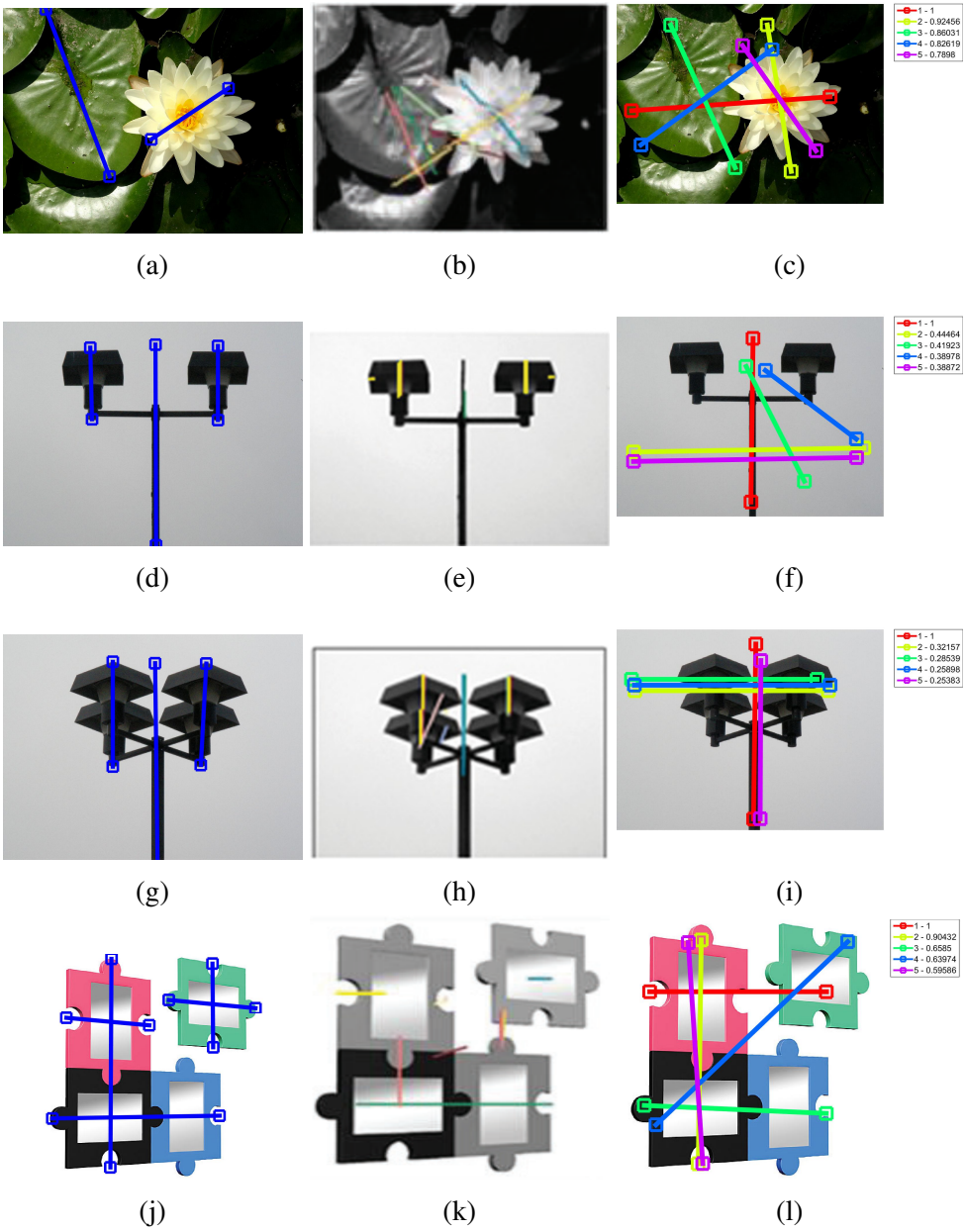

Figure 3.14 Qualitative comparison between the proposed method ***LgTC*** and the recent state-of-art Atadjanov and Lee ***Ata***, ECCV 2016 [8] using PSU [134, 95] dataset. First column: ***groundtruth (blue)***, second column: state-of-art ***Ata*** axis candidates with colored line segments (images from [8], third column: ***LgTC*** results with top five symmetry axes in such order: ***red***, ***yellow***, ***green***, ***blue***, and ***magenta***. Each symmetry axis in 1st and 3rd columns is shown in a straight line with squared endpoints.

Table 3.3 Using evaluation metrics **CVPR2013** [95] (table 2.2), comparison of the maximum F1 scores based on all detections for the proposed methods against the state-of-art algorithms. Symmetry datasets are presented as: single-case (first 4 rows) and multiple-case (last 3 rows). The last row represents average of the maximum F1 scores among all datasets. Top 3 results are in **Bold** with **red**, **blue** and **green** colors respectively.

Datasets	*Loy* [101]	*Cic* [28]	*GbT*	*LgT*	*LgTC*
PSU	0.514	0.569	**0.613**	**0.669**	**0.724**
AVA	**0.690**	0.493	0.667	**0.736**	**0.729**
NY	0.528	0.526	**0.627**	**0.698**	**0.766**
ICCV17	0.507	**0.536**	0.514	**0.707**	**0.713**
PSUm	**0.292**	0.159	0.277	**0.313**	**0.338**
NYm	0.337	0.237	**0.388**	**0.417**	**0.411**
ICCV17m	**0.273**	0.207	0.236	**0.263**	**0.285**
Average	0.449	0.390	**0.475**	**0.543**	**0.567**

images of single and multiple cases, with big difference in performance from the state-of-art algorithms (*Loy*, and *Cic*).

As a summary of the previous quantitative evaluations, figures (3.11-3.14) compare qualitatively top performing algorithms showing different examples of reflection symmetry detection. Despite the single-case images in figure 3.11 have strong edge information in foreground objects, the color version of the proposed method *LgTC* easily finds the correct symmetry axes in all presented examples as a first candidate. On the other hand, the non-color proposed method *LgT* satisfies the single-symmetry groundtruth in the half examples. In contrast, *GTb* mismatches the provided groundtruth with most examples of less edge detail, and *Loy* [101] mis-detects the symmetry axes as short segments or horizontal lines having same contrast values. In multiple-case images, The importance of textural weight in all proposed methods (*GTb*, *LgT*, *LgTC*) is presented in figure 3.12. However, the introduction of Log-Gabor feature representation (*LgT*) along side with color weight (*LgTC*) clearly detects the global and most of local symmetries in precise way as shown in figure 3.13. In the opposite side, *Loy* [101] struggles determining global groundtruth with incomplete endpoints. The recent algorithm *Ata* [8] (defined as the second baseline after Loy et Eklundh [101] in the recent symmetry competition [53]) is visually compared with the proposed method *LgTC* in figure 3.14, in terms of multiple symmetries inside natural, man-made and synthetic images. *LgTC* easily outperforms *Ata*[8] to find well-defined axes in a global scale. In natural example, *Ata* outputs incomplete axes to define symmetry inside the focused scene objects (flower, leave), while *LgTC* is able to fully represent symmetries in the same objects.

In two lamp examples, *Ata* focuses in defining local symmetries in the image parts (light holders), while *LgTC* displays the global symmetry in the middle column equalizing the sides of the entire scene. In the artificial image (puzzle game), *Ata* only manages in getting one global symmetry and cluttered local symmetries in the rest, while *LgTC* finds most global symmetrical axes except in the top right object.

3.6 Conclusion

In this chapter, we proposed a novel method to detect symmetry axes inside natural images using multi-scale Log-Gabor wavelets to extract symmetrical keypoints, followed by feature triangulation based on textural (neighboring orientation histograms) and color (local HSV descriptors) weights. This method preserves the neighboring spatial information around the content details of the focused objects inside an image. The evaluation was conducted on symmetry detection task on single and multiple cases, using all public dataset with standard evaluation measures. Experiments conclude that our method outperforms the state-of-art algorithms [101, 28]. The future direction could be extending our method to fuse different curve/edge detection approaches to refine the feature extraction process. In additions, different color descriptors (i.e. Opponent, rg) with better invariance properties [154] can be used instead of local HSV descriptors.

Chapter 4

Symmetry Representation and Selection

Résumé: Dans ce chapitre, nous étendons les méthodes proposées dans le chapitre précédent, afin d'estimer et de trouver des maxima dans un schéma continu. Par conséquent, nous proposons une méthode à noyau pour décrire des distributions comportant des données linéaires (noyau gaussien) et des données directionnelles (noyau de von-Mises). Puis, une méthode de type "mean-shift" de détection des pics de la distribution est développée. Dans un premier temps, nous validons les méthodes proposées sur des ensembles de données publics comportant des images réelles et des images synthétiques. Une étude comparative est menée pour la détection des axes de symétrie globaux lorsqu'un axe ou plusieurs axes sont recherchés. Les résultats obtenus indiquent que les méthodes proposées permettent d'obtenir des scores de symétrie élevés pour les axes présents dans les images.

Abstract: In this chapter, we extend the proposed methods in the previous chapter, in order to estimate and find linear-directional symmetrical peaks in a continuous scheme. Therefore, we propose a voting representation model and an algorithm for peak detections using joint linear-directional distributions respectively. Given data extracted from continuous statistical mixture model, we use Gaussian and von-Mises kernels for linear and directional distributions. First, we validate the proposed methods among real-world and synthetic images in public datasets to detect precisely global symmetrical axes for single and multiple cases. The final results summarized that the proposed framework can produce effective symmetry scores for correct axis candidates inside an image.

4.1 Introduction

In the baseline approaches [101, 28], a set of feature points are detected in the image, axis candidates are discretely sampled across the voting space. These sparse symmetry candidates further need to be grouped through a smoothing kernel to define relevant mono-

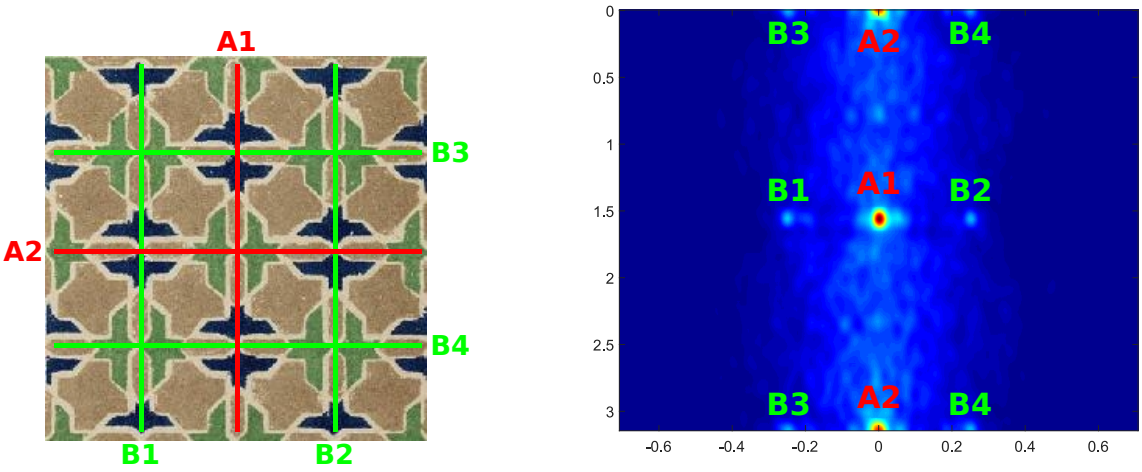

(a) Input with GT

(b) Voting representation

Figure 4.1 Symmetry voting process: (a) Input image with major (in red) and minor (in green) symmetry axes. (b) Smoothed output of the symmetry histogram with displacement (x-axis) and orientation (y-axis) coordinates, highlighting the corresponding axes.

or multi- axis hypothesis. Our idea (see figure 4.1) is to formulate the voting problem as a density estimation scheme, by computing the probability of detecting symmetry axis at every position and orientation inside the image plane. Kernel density estimation (KDE) is one of the most popular techniques in nonparametric statistics, which enables to perform continuous optimization finding precise maxima. Density estimates are controlled by a single kernel parameter (smoothing bandwidth in Gaussian or concentration term in von-Mises), and a weighting kernel function. Density estimates with linear kernels have been introduced in 1950s [4, 136] and have been represented in 1960s [129] as Parzen's windows, and then have been adapted to deal with directional data since the mid 1980s [70]. Many computer vision applications used kernel density estimation for linear data [47, 117, 36, 158, 150, 98], and fewer recently used it for directional data [155, 127]. Garcia-Portugues et al. [58] derived the general principle of joint kernel density estimator for linear-directional data.

In symmetry detection, state-of-art methods [101, 8] in the recent competition [53] uses a classical approach (Non-maximal Suppression) of a fixed window size to select symmetry maxima inside any voting representation. Our idea is to adapt mean-shift clustering technique to find precise locations of symmetry axes in continuous scheme, using weighted linear-directional distributions. mean-shift is widely-used mode-seeking method which clusters data and finds their centers iteratively by maximizing the embedded kernel density estimator. Thanks for nonparametric property, a prior knowledge of the number of clusters is not required for its internal processing. it was early introduced by Fukunaga and Hostetler [52] in 1970's. Cheng [25] presented the idea of using mean-shift in clustering linear

data, and this idea got generalized later using Gaussian kernel by Fashing and Tomasi [48], followed by Wu and Yang [164]. Linear mean-shift had been applied to many computer vision research areas (object tracking [35, 69, 33, 140, 172, 42, 170], image segmentation [34, 157, 19, 148, 80], texture classification [60], medical analysis [112, 103], line detection [12]). Recently for directional data, Kobayashi and Otsu [85] firstly proposed mean-shift algorithm using von-Mises distribution for hyper-spherical data based on Euclidean space. Afterwards, Chang-Chien et al. [23, 22] extended Wu and Yang's linear mean-shift method [164] and presented different versions of mean-shift approach (non-blurring and blurring) to handle circular data (directional information on 2D plane). The latter was extended by Yang et al. [165] to cluster directional data on a hypersphere space.

Our contribution in this chapter is twofold. First, we introduce a weighted Gaussian von-Mises (GvM) kernel-based voting representation for reflection symmetry detection, based on orientation and displacement information. Second, we propose a robust convergence method based on linear-directional mean-shift approach to select global symmetry peaks and find the corresponding feature pairs for each peak. The rest of the chapter is organized as follows: section 4.2 describes our method to represent symmetry voting scheme using a weighted linear-directional kernel density estimator. Section 4.3 presents detection of major symmetry peaks based on the proposed 2D mean-shift approach for linear and directional data. Section 4.4 describes the implementation details and the results on different benchmark datasets along side with comparisons with state-of-art algorithms. Section 4.5 summarizes the proposed work with highlighting the future works.

4.2 Symmetry representation

Let $\{\rho_n, \theta_n;\ \rho_n \in \mathbb{R}, \theta_n \in [-\pi, \pi[\}$ be a set of realizations of linear and directional continuous random variables representing the displacement and orientation parts of the candidate axis $\{q_n |\ n = 1, \ldots, N\}$ (defined in section 3.4), associated with the symmetry weight ω_n. N is the number of the candidate axes. Let $\boldsymbol{\theta}_n = [\cos(\theta_n), \sin(\theta_n)]$ describes the vector-based directional variable, as a circular data corresponding to θ_n.

4.2.1 Hough-like histogram

In order to detect symmetry axes, standard methods use an Hough transform like histogram defined as follows. Up on the introduction of symmetry voting in the previous chapter (see section 3.4), an accumulation histogram $\hat{f}(\bar{x}, \bar{y})$ is defined as the sum of the symmetry

weights of all discretized pairs of feature points such as:

$$\hat{f}(\bar{x},\bar{y}) = \sum_{n=1}^{N} \omega_n \, \delta_{\bar{x}-\bar{\rho}_n} \, \delta_{\bar{y}-\bar{\theta}_n} \tag{4.1}$$

where δ is the Kronecker delta, and $(\bar{\rho}_n, \bar{\theta}_n)$ is the discrete version of (ρ, θ) space. The voting histogram $\hat{f}(\bar{x},\bar{y})$ is extended along the vertical axis $\bar{y}$ in a circular way to solve the orientation discontinuity problem, and then is smoothed using a symmetric Gaussian low-pass filter of standard deviation σ_H to output a proper density representation.

This approach has three major drawbacks. First, the voting space is discretized and the discretization parameters have to be previously defined. Second, a smoothing function has to be used to define symmetry peaks properly. The standard deviation of this function has to be fixed and is also depending on the discretization of the accumulation space. Third, the vertical axis has to be extended in a circular way to avoid discontinuity problems. All these steps are defined in an empirical way.

4.2.2 Weighted kernel density estimator

Our proposition is to formulate the problem as a density estimation problem. Given the data samples, the voting space can be seen as a density function. Thus, standard density estimation tools can be used to estimate it namely the weighted kernel density estimation. In this context, we introduce our framework to define a linear-directional kernel density estimation for weighted data samples in the context of symmetry detection. To the best of our knowledge, this formulation has never been proposed before.

Inspired by [129], the linear kernel density estimator $f_\varepsilon(.)$ is defined as

$$f_\varepsilon(x;\sigma) = \frac{1}{N} \sum_{n=1}^{N} G_\varepsilon(\frac{x-\rho_n}{\sigma}),\ x \in \mathbb{R} \tag{4.2}$$

$$G_\varepsilon(u) = \frac{1}{\sqrt{2\pi}\sigma} \, e^{-\frac{1}{2}|u|^2}, \tag{4.3}$$

where $G_\varepsilon(.)$ is a Gaussian kernel with bandwidth parameter σ. Inspired by [70], The directional kernel density estimator $f_\vartheta(.)$ is defined as:

$$f_\vartheta(\mathbf{y};\kappa) = \frac{1}{N} \sum_{n=1}^{N} G_\vartheta(\boldsymbol{\theta}_n^T \mathbf{y};\kappa),\ \mathbf{y} \in \Omega_2 \tag{4.4}$$

$$G_\vartheta(x;\kappa) = A(\kappa)\, e^{\kappa x},\ A(\kappa) = \frac{1}{2\pi B(0,\kappa)}, \tag{4.5}$$

$$\mathbf{y} = [\cos(\theta), \sin(\theta)]^T,\ \boldsymbol{\theta}_n = [\cos(\theta_n), \sin(\theta_n)]^T, \tag{4.6}$$

where $G_\vartheta(.)$ is a von-Mises kernel [107] with concentration parameter κ, and normalization constant $A(\kappa)$. $B(.)$ is the modified Bessel function of the first kind. $\mathbf{y}$ is remarked as directional unit-vector of angle θ, such that $||\mathbf{y}|| = 1$. Ω_2 is a circular directional space. The motivation to use von-Mises kernel is the periodic nature of the angle parameter. This choice allows to formulate this problem in a rigorous way.

In order to combine linear and directional information in 2D space, the axis candidate samples $(\rho_1, \theta_1), \ldots, (\rho_N, \theta_N)$ are associated with symmetry weights $\omega = \omega_1, \omega_2, \cdots, \omega_N$, and use of the linear-directional density estimator $f_{\varepsilon,\vartheta}(.)$ in [58]. We define the extended weighted version $\hat{f}_{\varepsilon,\vartheta}(.)$ as:

$$\hat{f}_{\varepsilon,\vartheta}(x, \mathbf{y}; \sigma, \kappa) = \frac{1}{N} \sum_{n=1}^{N} \omega_n G_\varepsilon(\frac{x - \rho_n}{\sigma}) G_\vartheta(\boldsymbol{\theta}_n^T \mathbf{y}; \kappa) \tag{4.7}$$

For sake of simplicity [58], the 2D kernel $G_{\varepsilon,\vartheta}(.)$ is splitted in a product of two kernels $G_\varepsilon(.)\, G_\vartheta(.)$, which doesn't mean that x and $\mathbf{y}$ are considered as independent. Assuming the previous sum of the weights (see equation 3.25) is normalized to 1, they have to be multiplied by N. In the case, we need the computation of the density over a discrete set, the density estimator can be expressed in a matrix form:

$$\boldsymbol{\varepsilon}_m = \begin{bmatrix} G_\varepsilon(\frac{x_m - \rho_1}{\sigma}) \\ \vdots \\ G_\varepsilon(\frac{x_m - \rho_N}{\sigma}) \end{bmatrix} \quad , \quad \boldsymbol{\vartheta}_l = \begin{bmatrix} G_\vartheta(\boldsymbol{\theta}_1^T \mathbf{y_l}; \kappa) \\ \vdots \\ G_\vartheta(\boldsymbol{\theta}_N^T \mathbf{y_l}; \kappa) \end{bmatrix} \tag{4.8}$$

$$\mathbf{G}_\varepsilon = \begin{bmatrix} \boldsymbol{\varepsilon}_1 & \cdots & \boldsymbol{\varepsilon}_m & \cdots & \boldsymbol{\varepsilon}_M \end{bmatrix} \quad , \quad \mathbf{G}_\vartheta = \begin{bmatrix} \boldsymbol{\vartheta}_1 & \cdots & \boldsymbol{\vartheta}_l & \cdots & \boldsymbol{\vartheta}_L \end{bmatrix} \tag{4.9}$$

$$\hat{F}_{\varepsilon,\vartheta} = \frac{1}{N} \mathbf{G}_\varepsilon^T\, diag(\omega)\, \mathbf{G}_\vartheta \tag{4.10}$$

where M and L are number of sampling bins for linear and directional data respectively.

Figure 4.2 presents an example of multiple symmetry detection, using 1D and 2D kernel-based voting maps. Three vertical symmetry axes are shown in the weighted linear kernel density $\hat{f}_\varepsilon(x; \sigma)$ (figure 4.2b). Two major directional axes appear in the weighted directional kernel density $\hat{f}_\vartheta(y; \kappa)$ at angles $(90°, 180°)$ (figure 4.2c). All global symmetry axes are clearly recognized through the combination version of the previous weighted densities $\hat{f}_{\varepsilon,\vartheta}(x, y; \sigma, \kappa)$ (figure 4.2d). To obtain such representation, as θ originally belongs to $[0, \pi)$,

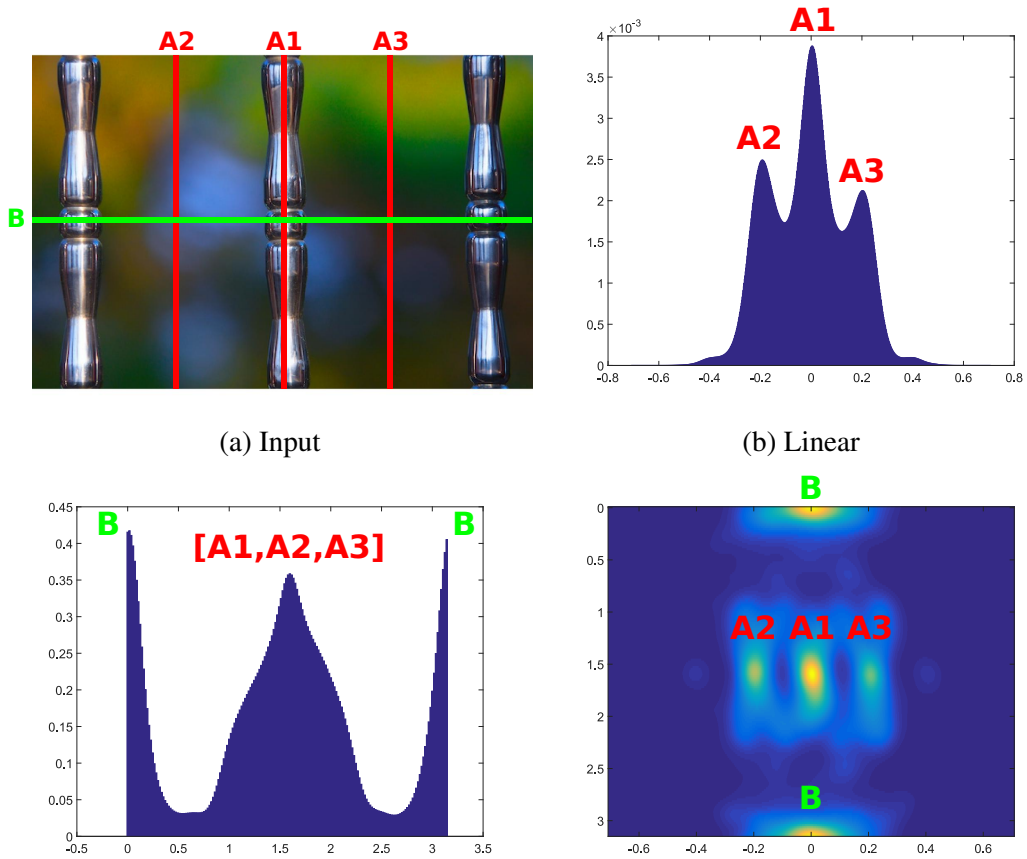

(a) Input

(b) Linear

(c) Directional

(d) Linear-Directional

Figure 4.2 Symmetry voting process: (a) Some input image with global symmetry axis candidates (three vertical axes in red and one horizontal axis in green). (b) the output of weighted linear kernel density $\hat{f}_{\varepsilon}(x;\sigma)$ over 800 bins. (c) The output of the weighted directional kernel density $\hat{f}_{\vartheta}(y;\kappa)$ over 180 bins. (d) The output of the weighted linear-directional kernel density $\hat{f}_{\varepsilon,\vartheta}(x,y;\sigma,\kappa)$ over 800×180 bins. The default values of σ and κ are used, see subsection 4.4.1. Maximal peaks are associated with global symmetry axes.

each angle value is multiplied by 2 in order to obtain an appropriate periodicity with the directional kernel.

Figure 4.3 shows in-process voting comparison of linear data ρ between Hough-like histograms $\hat{f}(\bar{x})$ and weighted KDE $\hat{f}_{\varepsilon}(x;\sigma)$. The discrete linear representation $\bar{x}$ of Hough-like histogram $\hat{f}(\bar{x})$ (figure 4.3a) takes a sampling effect on the smoothed output (figure 4.3c) to determine the precise center location of the symmetrical peak. However, the computation of the weighted KDE $\hat{f}_{\varepsilon}(x;\sigma)$ applies on continuous data x with less sampling effect, resulting the symmetrical peaks in clear way especially the top peak at the center displacement $x \simeq 0$.

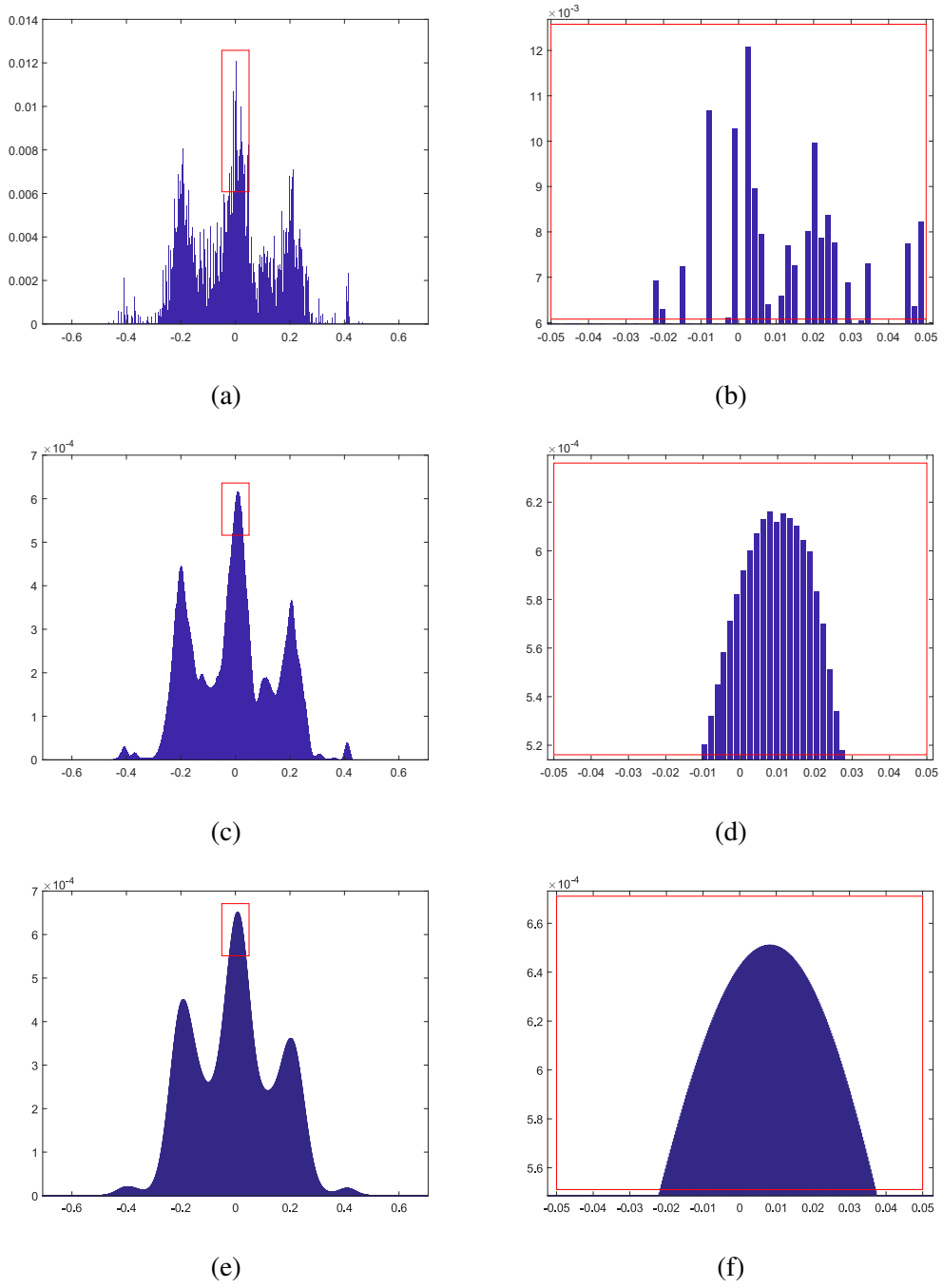

Figure 4.3 an example of symmetry voting between Hough-like Histogram (1st two rows) and Weighted KDE (last row) to find the reflection axes over linear data ρ, inside the input image used in figure 4.2. 1st column represents (a,c) Hough Histogram $\hat{f}(\bar{x})$ before and after Gaussian smoothing, (e) Weighted linear kernel density $\hat{f}_{\varepsilon}(x;\sigma)$. 2nd column displays zoom-in details of top peaks that appear as red rectangles in 1st column. The default value of σ is used, see subsection 4.4.1.

4.3 Dominant axes selection

In standard existing methods, upon providing the voting representation (figure 4.4a), the symmetrical peaks are selected through some maxima-finding techniques to output the segments of different axis candidates. The spatial boundaries of each symmetry candidate segment are computed as shown in figure 4.4b through the convex hull of the associated voting pairs [101].

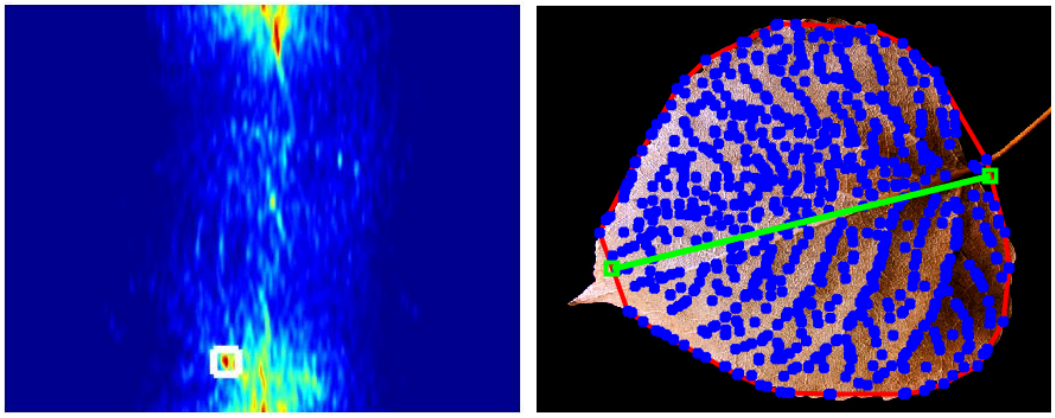

(a) Voting Space (b) Image with Top Symmetry Segment

Figure 4.4 Process of symmetry axes selection. (a) Input: finding the line parameters of the maxima (white square box) from the voting representation. (b) Output: symmetry axis (green line) with defined endpoints (two green square boxes) through intersection of the maxima line parameters with the convex hull (red segments) of points (blue dots) voting for this maxima.

Thanks to the continuous nature of our density estimation, we can then formulate the problem of maxima determination as a functional analysis problem: how to find the local maxima of a continuous function. Moreover, our continuous function is defined by kernel density estimation. Hopefully, this problem benefits from a well known solution through the mean shift algorithm. In this section, after recalling the principal of non maximal suppression, we introduce the symmetry peak selection based on the mean shift algorithm.

4.3.1 Non-maximal suppression

Major symmetry peaks are selected as in [101, 28] among the voting representation by reaching-out clear extreme spots using well-known non-maximal suppression technique [18]. The basic steps are explained in algorithm 1: (1) wrap angular axis using a predefined extension parameter to solve the periodic discontinuity of directional θ data, (2) blur the voting representation using smoothing kernel of Gaussian distribution to remove the small

texture details and noise inside an image, (3) unwrap angular axis to reshape the processed image back into the original size, (4) keep only local maxima points that are maximum with respect to their neighbors inside a region located around the point (i.e. rectangular window). Figure 4.5 shows a 1D example of different normal distributions and illustrates how Non-Maximal Suppression (NMS) technique can be effective to select the maxima points among the different peaks.

Algorithm 1 Maxima selection using Non-Maximal Suppression (NMS) algorithm

Input: Weighted voting representation $\hat{f}(x,y)$ in terms of linear ρ and directional θ data
Output: Peak positions of ρ, θ

1: Wrap along angular θ axis
2: Blur using Gaussian kernel
3: Unwrap along angular θ axis
4: Select well-separated maxima peaks using NMS

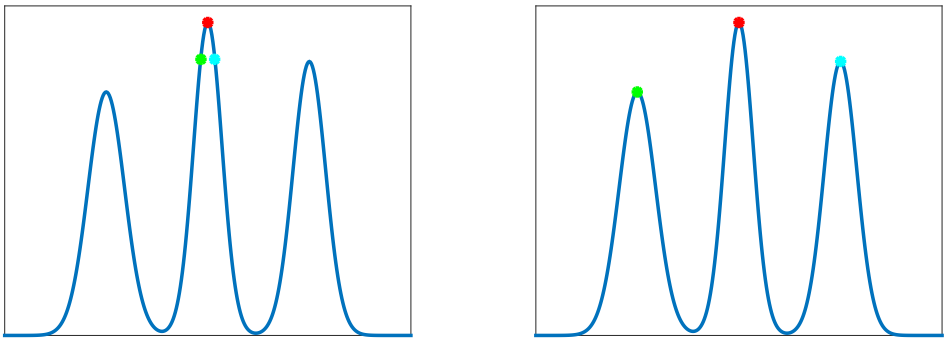

(a) Before NMS (b) After NMS

Figure 4.5 An example showing the effectiveness of Non-Maximal Suppression (NMS) technique on selecting maxima over three Gaussian peaks (1st in red, 2nd in cyan, 3rd in green). (a) all top 3 maxima are concentrated over the highest peak. (b) with predefined elimination window size, the top 3 maxima are well distributed across the different peaks.

4.3.2 Mean-shift

Mean-shift is a non-parametric density gradient estimation technique that doesn't need prior knowledge about number and shape of peak regions [38]. Now, we will explain the general principle of mean-shift algorithm.

Given samples x of size N and kernel K, a simple kernel density estimator is as follows:

$$f(x) = \frac{1}{N} \sum_{n=1}^{N} K(x - x_n) \tag{4.11}$$

The general formula of gradient ascent from generation i to generation $i+1$ is:

$$x^{i+1} = x^i + m(x^i) \tag{4.12}$$

Such that for any generation i, the mean shift vector $m(x^i)$ is defined as follows:

$$m(x^i) = \frac{\sum_{n=1}^{N} x_n^i \, g(x^i - x_n^i)}{\sum_{n=1}^{N} g(x^i - x_n^i)} - x^i \tag{4.13}$$

where $g(.) = -K'(.)$. So the general procedure can be explained according for each sample point x_n^i of size N at generation i:

— Compute mean shift vector $m(x^i)$.
— Shift each sample point x_n^i by this vector $m(x^i)$.
— Repeat the previous steps till convergence $m(x^i) \simeq 0$.

The main purpose of mean-shift as shown in figure 4.6 is converging the data samples in continuous feature space into the dense regions corresponding to the local maxima peaks of the underlying kernel distribution. The rest of this section explains the extension of the general definition of mean shift principle to deal with two different types of kernels: linear and directional.

In algorithms (2,3), the proposed mean-shift technique handles weighted linear and directional data to find precise locations of symmetry peaks in 2D voting representation with respect to the underlying kernel density estimators (in our case, linear: Gaussian and directional: von-Mises).

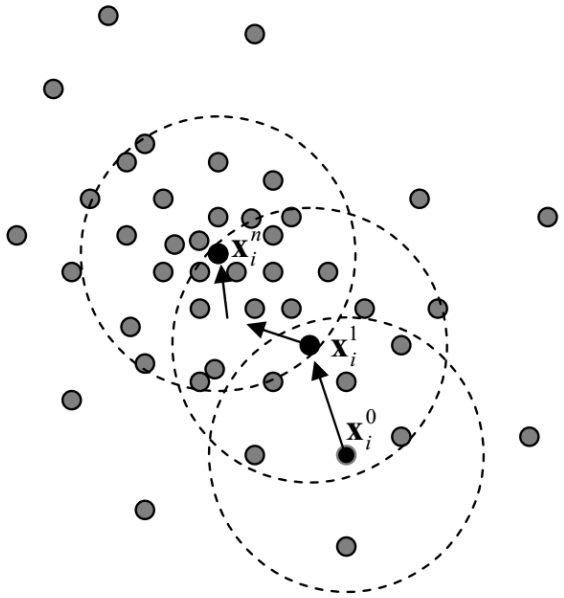

Figure 4.6 Visual explanation of mean-shift algorithm. Source: Mean Shift Clustering, Konstantinos G. Derpanis, August 15, 2005, Lecture Notes in Computer Vision.

Algorithm 2 GvM mean-shift algorithm

Input: $(\rho_n, \theta_n, \omega_n)$; $n = 1 \ldots N$ samples
Output: Peak positions of $\rho, \theta = \{\tilde{x}_j, \tilde{\mathbf{y}}_j, \tilde{\omega}_j\}$; $j = 1 \ldots J$, $J \leq N$

1: **Initialization:** $x_n^{(0)} = \rho_n$, $\mathbf{y}_n^{(0)} = [\cos(\theta_n), \sin(\theta_n)]$; $n = 0 \ldots N$
2: t=0
3: **while** not converged **do**
4: **for** $i = 1$ to N **do**
5: Update $\mathbf{y}_i^{(t+1)} \leftarrow (x_i^{(t)}, \mathbf{y}_i^{(t)})$ using Eq. (4.22)
6: Update $x_i^{(t+1)} \leftarrow (x_i^{(t)}, \mathbf{y}_i^{(t+1)})$ using Eq. (4.23)
7: **stop:** $\sum_i d((x_i^{(t+1)}, y_i^{(t+1)}), (x_i^{(t)}, y_i^{(t)})) \leq \Delta_C$; using Eq. (4.24)
8: t=t+1
9: **merge:** Alg. 3 with Inputs $\{x_n^{t+1}, \mathbf{y}_n^{t+1}, \omega_n\}$

Algorithm 3 Joint merge algorithm

Input: $X = \{(x_n, \mathbf{y}_n, \omega_n)\};\ n = 1 \dots N$ samples
Output: $\tilde{X} = \{(\tilde{x}_j, \tilde{\mathbf{y}}_j, \tilde{\omega}_j)\};\ j = 1 \dots J,\ J \leq N$ merged samples

Initialization: $\tilde{X} = X$
$m = 1,\ J = N$
while $m \neq J$ **do**
    Compute $d_{m,j} = d(x_m, y_m, x_j, y_j);\ j = 0 \dots J,\ j \neq k$ using eq. (4.24)
    Compute $I = \{j | d_{m,j} \leq \Delta_M\} \cup \{m\}$
    $J = J + 1$
    $\tilde{x}_J = \frac{\sum \omega_n x_n}{\sum \omega_n};\ n \in I$
    $\tilde{\mathbf{y}}_J = \frac{\sum \omega_n \mathbf{y}_n}{||\sum \omega_n \mathbf{y}_n||};\ n \in I$
    $\tilde{\omega}_J = \sum \omega_n;\ n \in I$
    Delete $\tilde{X} \rightarrow \{(x_n, \mathbf{y}_n, \omega_n)\};\ n \in I$
    Add $\tilde{X} \leftarrow (\tilde{x}_J, \tilde{\mathbf{y}}_J, \tilde{\omega}_J)$
    $J = J - |I|$
    $m = m + 1$

In 1D case, mean-shift iteratively convergences through the computation of linear $x_i^{(t+1)}$ and directional $\mathbf{y}_i^{(t+1)}$ samples:

$$x_i^{(t+1)} = x_i^{(t)} + m_\varepsilon(x_i^{(t)}) \tag{4.14}$$

$$= x_i^{(t)} + \left[\frac{\sum_{n=1}^{N} \rho_n G'_\varepsilon(\frac{x_i^{(t)} - \rho_n}{\sigma})}{\sum_{n=1}^{N} G'_\varepsilon(\frac{x_i^{(t)} - \rho_n}{\sigma})} - x_i^{(t)} \right] \tag{4.15}$$

$$= \frac{\sum_{n=1}^{N} \rho_n G'_\varepsilon(\frac{x_i^{(t)} - \rho_n}{\sigma})}{\sum_{n=1}^{N} G'_\varepsilon(\frac{x_i^{(t)} - \rho_n}{\sigma})} \tag{4.16}$$

$$= \frac{\sum_{n=1}^{N} \rho_n \exp(-\frac{(x_i^{(t)} - \rho_n)^2}{2\sigma^2})}{\sum_{n=1}^{N} \exp(-\frac{(x_i^{(t)} - \rho_n)^2}{2\sigma^2})} \tag{4.17}$$

$$\mathbf{y}_i^{(t+1)} = \mathbf{y}_i^{(t)} + m_\vartheta(\mathbf{y}_i^{(t)}) \tag{4.18}$$

$$= \mathbf{y}_i^{(t)} + \left[\frac{\sum_{n=1}^{N} \boldsymbol{\theta}_n \, G'_\vartheta(\boldsymbol{\theta}_n^T \mathbf{y}_i^{(t)}; \kappa)}{||\sum_{n=1}^{N} \boldsymbol{\theta}_n \, G'_\vartheta(\boldsymbol{\theta}_n^T \mathbf{y}_i^{(t)}; \kappa)||} - \mathbf{y}_i^{(t)} \right] \tag{4.19}$$

$$= \frac{\sum_{n=1}^{N} \boldsymbol{\theta}_n \, G'_\vartheta(\boldsymbol{\theta}_n^T \mathbf{y}_i^{(t)}; \kappa)}{||\sum_{n=1}^{N} \boldsymbol{\theta}_n \, G'_\vartheta(\boldsymbol{\theta}_n^T \mathbf{y}_i^{(t)}; \kappa)||} \tag{4.20}$$

$$= \frac{\kappa \sum_{n=1}^{N} \boldsymbol{\theta}_n \, exp(\kappa(\boldsymbol{\theta}_{n,1} \,.\, \mathbf{y}_{i,1}^{(t)} + \boldsymbol{\theta}_{n,2} \,.\, \mathbf{y}_{i,2}^{(t)}))}{||\kappa \sum_{n=1}^{N} \boldsymbol{\theta}_n \, exp(\kappa(\boldsymbol{\theta}_{n,1} \,.\, \mathbf{y}_{i,1}^{(t)} + \boldsymbol{\theta}_{n,2} \,.\, \mathbf{y}_{i,2}^{(t)}))||} \tag{4.21}$$

with initialization $x_i^{(0)} = \rho_i$, $\mathbf{y}_i^{(0)} = \boldsymbol{\theta}_i$ where $i = 1, \ldots, N$ represents samples index, $m_\varepsilon(.)$, $m_\vartheta(.)$ are linear and directional mean-shift vectors, G'_ε, G'_ϑ are first derivatives of G_ε, G_ϑ kernels, and $\mathbf{y}_i, \boldsymbol{\theta}_i$ are directional unit-vectors.

As in [58], we simplify and consider the joint case of linear-directional data as a kernel product $G_{\varepsilon,\vartheta}(x, \mathbf{y}) = G_\varepsilon(x) \times G_\vartheta(\mathbf{y})$. So that the joint convergence of mean-shift with weighted linear-directional data is defined as follows:

$$\mathbf{y}_i^{(t+1)} = \frac{\sum_{n=1}^{N} \omega_n \, \boldsymbol{\theta}_n \, G'_\vartheta(\boldsymbol{\theta}_n^T \mathbf{y}_i^{(t)}; k) \, G_\varepsilon(\frac{x_i^{(t)} - \rho_n}{\sigma})}{||\sum_{n=1}^{N} \omega_n \, \boldsymbol{\theta}_n \, G'_\vartheta(\boldsymbol{\theta}_n^T \mathbf{y}_i^{(t)}; k) \, G_\varepsilon(\frac{x_i^{(t)} - \rho_n}{\sigma})||} \tag{4.22}$$

$$x_i^{(t+1)} = \frac{\sum_{n=1}^{N} \omega_n \, \rho_n \, G'_\varepsilon(\frac{x_i^{(t)} - \rho_n}{\sigma}) \, G_\vartheta(\boldsymbol{\theta}_n^T \mathbf{y}_i^{(t+1)}; k)}{\sum_{n=1}^{N} \omega_n \, G'_\varepsilon(\frac{x_i^{(t)} - \rho_n}{\sigma}) \, G_\vartheta(\boldsymbol{\theta}_n^T \mathbf{y}_i^{(t+1)}; k)} \tag{4.23}$$

The convergence constraint of mean-shift algorithm is computed based on the similarity criteria between data samples of upcoming $(x_i^{(t+1)}, y_i^{(t+1)})$ and current iterations $(x_i^{(t)}, y_i^{(t)})$, such that we introduce the joint linear-directional distance function $d(.)$ to handle the termination condition required to limit the unnecessary mean-shift convergence after some iterations. We define this distance in terms of linear and directional data in continuous and periodic way (see ap. B: eq. B.29):

$$d((x_i^{(t+1)}, y_i^{(t+1)}), (x_i^{(t)}, y_i^{(t)})) = \frac{(x_i^{(t+1)} - x_i^{(t)})^2}{2\sigma^2} + \kappa \frac{B'(0,\kappa)}{B(0,\kappa)} (1 - \cos(y_i^{(t+1)} - y_i^{(t)})); \; \forall i \tag{4.24}$$

where $B'(.)$ is the first derivative of $B(0, \kappa)$. The same distance function $d(.)$ is also used to merge between final data samples after mean-shift convergence as shown in algorithm 3.

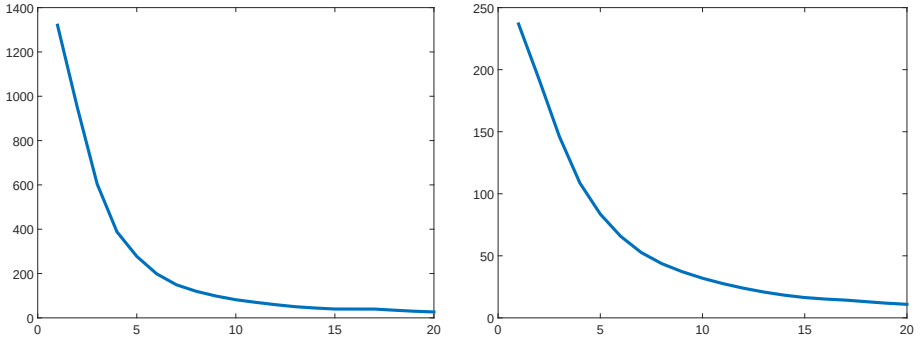

(a) Joint Distance (b) MS Vector Norm

Figure 4.7 Validation of mean-shift convergence for the input image shown in figure 4.2 using (1) sum of joint linear-directional distance function $\sum d(.)$ (equation 4.24), (2) sum of linear-directional mean-shift vector norm $\sum ||m_{\varepsilon,\vartheta(.)}||$ with $\alpha = 0.5$ (equation 4.26). Number of iterations is 20. (x-axis: iteration number, y-axis: error).

Figure 4.7 numerically shows that the distance function $d(.)$ have same convergence behavior as joint mean-shift mean vector norm defined as:

$$||m_{\varepsilon,\vartheta}(x_i^{(t)}, \mathbf{y}_i^{(t)})|| = \alpha\, ||m_{\varepsilon}(x_i^{(t)}; \mathbf{y}_i^{(t)}, \omega_i)||^2 + (1-\alpha)\, ||m_{\vartheta}(\mathbf{y}_i^{(t)}; x_i^{(t)}, \omega_i)||^2;\ \forall i \tag{4.25}$$

$$= \alpha\, (x_i^{(t+1)} - x_i^{(t)})^2 + (1-\alpha)\, (1 - \cos(y_i^{(t+1)} - y_i^{(t)}))^2 \tag{4.26}$$

where $\alpha \in [0,1]$ is a weighting term. The norm equation is in its simple form without handling kernel parameters, such that the first term is euclidean distance between displacement samples and the second term is cosine distance between directional ones.

Figure 4.8 shows the step-by-step results of the proposed mean-shift algorithm, based on the same image used in figure 4.2. Sub-figure 4.8a presents initial state of linear ρ (x-axis) and directional θ (y-axis) data, with four symmetric centroids (three at $\theta \simeq 90^\circ$ and one at $\theta \simeq 0^\circ$). An extra optional merging step (sub-figure 4.8b) is applied into the initial data, to reduce the input size for MS convergence step through combining the samples with exact or very close locations. In the iterations of MS convergence (sub-figures 4.8c- 4.8g), the non-centric samples move fast into the corresponding nearest centroids and collapse into them. A final merging step in sub-figure 4.8h and its zoom-in version in figure 4.9 is employed on the last MS version of the samples to refine the densities of the symmetric centroids.

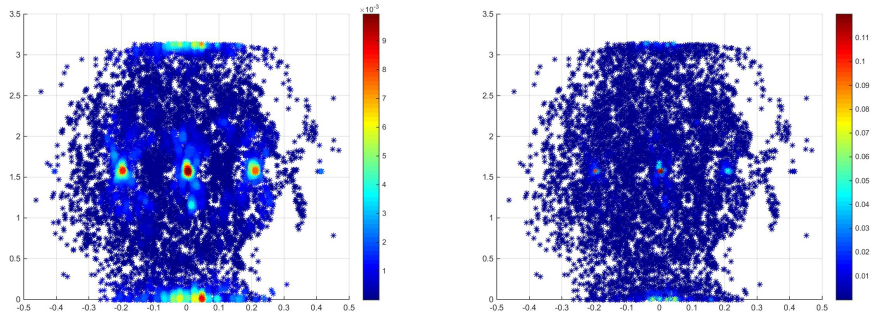

(a) Initial

(b) 1st Merging

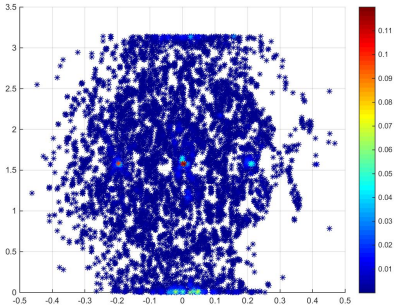

(c) Itr = 1

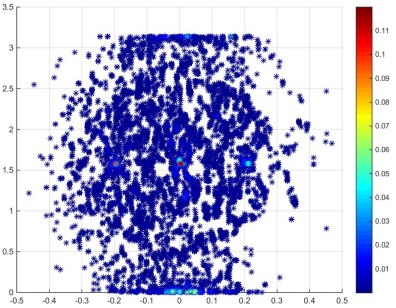

(d) Itr = 2

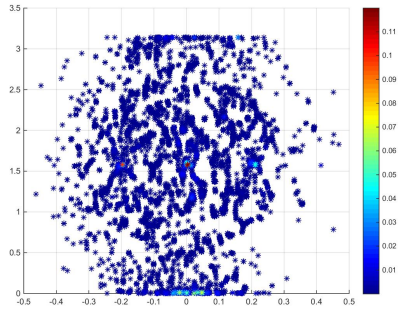

(e) Itr = 5

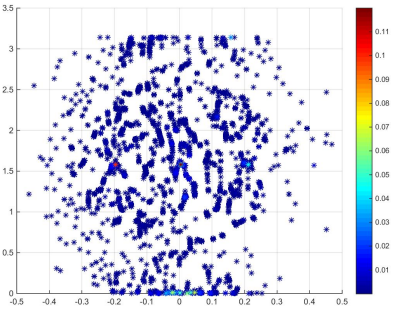

(f) Itr = 10

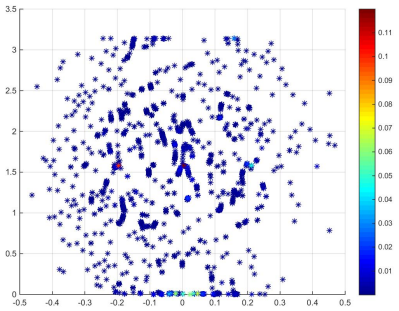

(g) Itr = 20

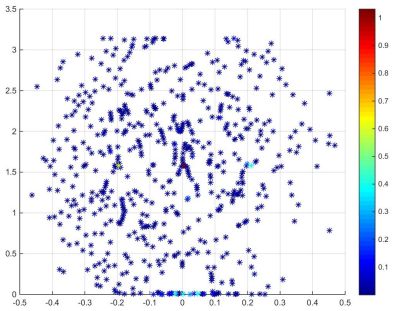

(h) 2nd Merging

Figure 4.8 Sequence of linear ρ and directional θ data obtained by the proposed mean-shift algorithm for the input image shown in figure 4.2. Each image is presented using 2D projection on the polar system (ρ: x-axis, θ: y-axis), colored by its density ω.

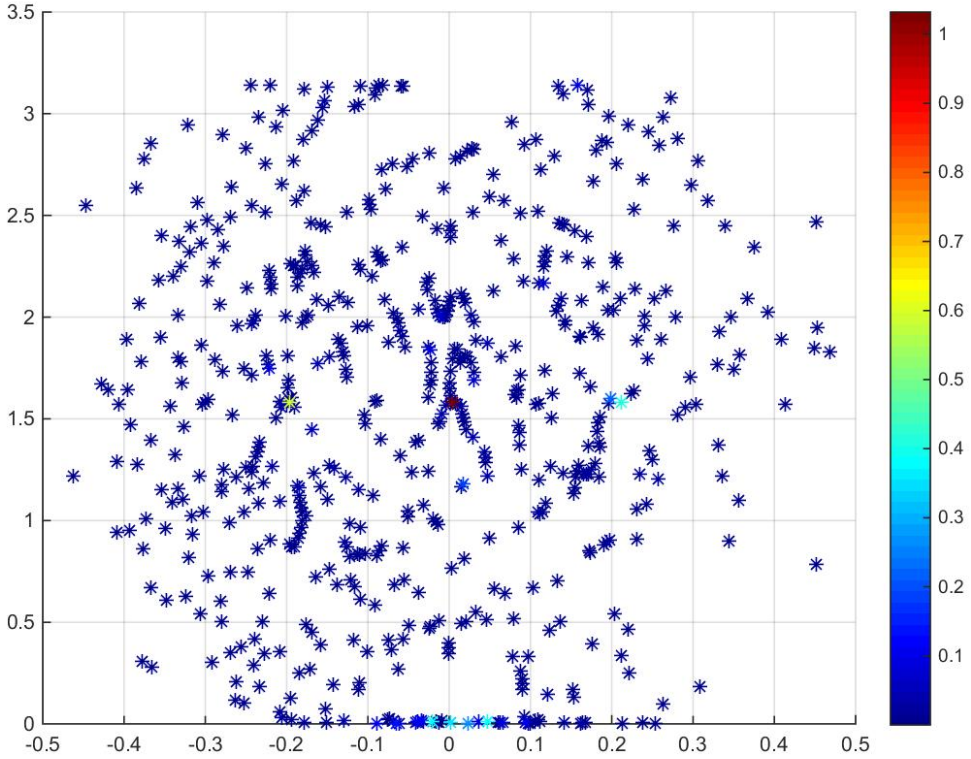

Figure 4.9 Zoom-in version of merging post-processing after last MS step, which is presented using 2D projection on the polar system (ρ: x-axis, θ: y-axis), colored by its density ω.

4.4 Results

In this section, we present experimental results on both synthetic and real-world images of the benchmark symmetry detection datasets [95, 27, 44, 53], respect to standard metrics [95, 53]. Firstly, we compare the improvement of symmetrical voting representation using weighted linear-directional kernel density estimator, instead using a smoothed hough-like histogram space. Then we also compare the enhancement of finding the symmetrical axes through the convergence of the weighted linear-directional mean-shift algorithm using Gaussian and von-Mises kernels, rather than application of classical non-maximal suppression selection method.

4.4.1 Experimental settings

In our experiments, State-of-the-art approaches (*Loy* [101] and *Cic* [28]) with different variants of the proposed methods from the previous chapter (*GbT*, *LgT*, and *LgTC*) are compared with the proposed work in this chapter (*LgTC-KDE*, *LgTC-MS*). Table 4.1 illustrates the strategy selection for each method in two aspects: symmetry voting (***Hough:*** *Hough*-like histogram, ***KDE:*** weighted GvM *K*ernel *D*ensity *E*stimator) and symmetry selection (***NMS:*** *N*on-*M*aximal *S*uppression, ***MS:*** weighted GvM *M*ean-*S*hift). For fair comparison, we consider at most first 50 axis candidates to evaluate each algorithm. In Hough-like Histogram, we set the number of bins for linear $\bar{x}$ and directional $\bar{y}$ discrete variables to $\sqrt{H^2+W^2}$ and 360 respectively, we set standard deviation σ_H of Gaussian filter to 5 and its kernel size $4\,\sigma_H$. For the computation of the weighted kernel density estimator, we set the Gaussian bandwidth parameter σ to $2/max(W,H)$, and the concentration parameter κ of von-Mises kernel to $max(W,H)/5$. In the proposed mean-shift algorithm, we set the maximum number of iterations to 20, the convergence threshold Δ_C to $2.2204e^{-16}$, the merging distance threshold Δ_M to 0.1. For the sake of fast mean-shift computation, we firstly sort the axis candidate pairs respect to its symmetry weights in descend way. Then we applied an extra merging step inside the mean-shift algorithm (before the convergence step).

4.4.2 Performance analysis

We tested the performance of our proposed methods to detect global symmetries inside images precisely, and separate the correct axis candidates from the incorrect ones. We verified these methods with the state-of-art algorithms in terms of voting representation and maximal selection.

Table 4.1 Implementation details of the state-of-art algorithms along side with the proposed work, showing the main contributions of each algorithm in two aspect: symmetry voting and selection of maximal peaks along side with corresponding contributing pairs.

Algorithms	Voting		Selection	
	Hough	KDE	NMS	MS
Loy [101]	✓		✓	
Cic [28]	✓		✓	
GbT	✓		✓	
LgT	✓		✓	
LgTC	✓		✓	
LgTC-KDE		✓	✓	
LgTC-MS		✓		✓

Table 4.2 Using evaluation metrics **CVPR2013** [95] (table 2.2), comparison of the true positive rates based on top detection for the proposed methods (especially *LgTC-KDE*) against the state-of-art algorithms. Symmetry datasets are presented as: single-case (first 4 rows) and multiple-case (last 3 rows), highlighted between (parenthesis) the number of images for each dataset. The last row represents sum of true positive rates among all datasets. Top 3 results are in **Bold** with **red**, **blue** and **green** colors respectively.

Datasets	*Loy* [101]	*Cic* [28]	*GbT*	*LgT*	*LgTC*	*LgTC-KDE*
PSU (157)	81	90	97	**104**	**113**	**118**
AVA (253)	**174**	124	170	**188**	**182**	**188**
NY (176)	98	92	**109**	**124**	**135**	**135**
ICCV17 (100)	52	**53**	52	**70**	**70**	**74**
PSUm (142)	69	68	67	**72**	**75**	**78**
NYm (63)	32	**36**	**36**	**38**	**40**	**38**
ICCV17m (100)	**54**	39	52	52	**57**	**56**
Total (991)	560	502	583	**648**	**672**	**687**

In first experiment through the statistical tables (4.3, 4.2) and visual comparison in figure 4.10, we evaluated the proposed method *LgTC-KDE*, using GvM kernel density estimator for voting representation against the previous proposed methods (*GbT*, *LgT*, and *LgTC*) and state-of-art (*Loy* [101] and *Cic*[28]). Table 4.3 presents performance results in terms of maximum F1 scores. In single-case, the proposed work *LgTC-KDE* shows a noticeable improvement especially in the recent symmetry dataset (ICCV17). While in multiple case, *LgTC-KDE* has a slightly performance increase over the concurrent methods.

Table 4.3 Using evaluation metrics **CVPR2013** [95] (table 2.2), comparison of the maximum F1 scores based on all detections for the proposed methods (especially *LgTC-KDE*) against the state-of-art algorithms. Symmetry datasets are presented as: single-case (first 4 rows) and multiple-case (last 3 rows). The last row represents average of the maximum F1 scores among all datasets. Top 3 results are in **Bold** with **red**, **blue** and **green** colors respectively.

Datasets	*Loy* [101]	*Cic* [28]	*GbT*	*LgT*	*LgTC*	*LgTC-KDE*
PSU	0.514	0.569	0.613	**0.669**	**0.724**	**0.757**
AVA	0.690	0.493	0.667	**0.736**	**0.729**	**0.737**
NY	0.528	0.526	0.627	**0.698**	**0.766**	**0.771**
ICCV17	0.507	0.536	0.514	**0.707**	**0.713**	**0.753**
PSUm	0.292	0.159	0.277	**0.313**	**0.338**	**0.341**
NYm	0.337	0.237	0.388	**0.417**	**0.411**	**0.413**
ICCV17m	**0.273**	0.207	0.236	0.263	**0.285**	**0.287**
Average	0.449	0.390	0.475	**0.543**	**0.567**	**0.580**

The baseline *Loy* [101] is still best competent in the recent multiple symmetry dataset (ICCV17m). In table 4.2, *LgTC-KDE* has the best true positive results based on the first axis candidate with maximum score, especially in (PSU and ICCV17) for single-case and (PSUm) for multiple-case datasets. Some results of the top axis candidates of each method is proving in figure 4.10 the significant effect of the proposed method *LgTC-KDE* in terms of symmetry orientation and spatial location. *LgTC-KDE* identifies the correct axis orientation in 1st row with improper shifted displacement and finds in 2nd row the false angular information inside visual scenes of different environments (landscape, street, aerial, and indoor). *Loy* [101] concentrates in finding either correct local axes or incorrect short segments defining intra-object symmetry details.

Table 4.4 Using evaluation metrics **ICCV2017-Training** [53] (table 2.2), comparison of the maximum F1 scores based on all detections for the proposed methods (especially *LgTC-MS*) against the state-of-art algorithms. Symmetry datasets are presented in multiple-case (first 3 rows). The last row represents average of the maximum F1 scores among all datasets. Top 3 results are in **Bold** with **red**, **blue** and **green** colors respectively.

Datasets	*Loy* [101]	*Cic* [28]	*GbT*	*LgT*	*LgTC*	*LgTC-KDE*	*LgTC-MS*
PSUm	0.125	0.052	0.145	0.142	**0.147**	**0.160**	**0.171**
NYm	0.136	0.092	**0.231**	0.189	**0.202**	0.197	**0.256**
ICCV17m	0.113	0.059	**0.118**	0.106	0.117	**0.121**	**0.129**
Average	0.125	0.068	**0.165**	0.146	0.155	**0.159**	**0.185**

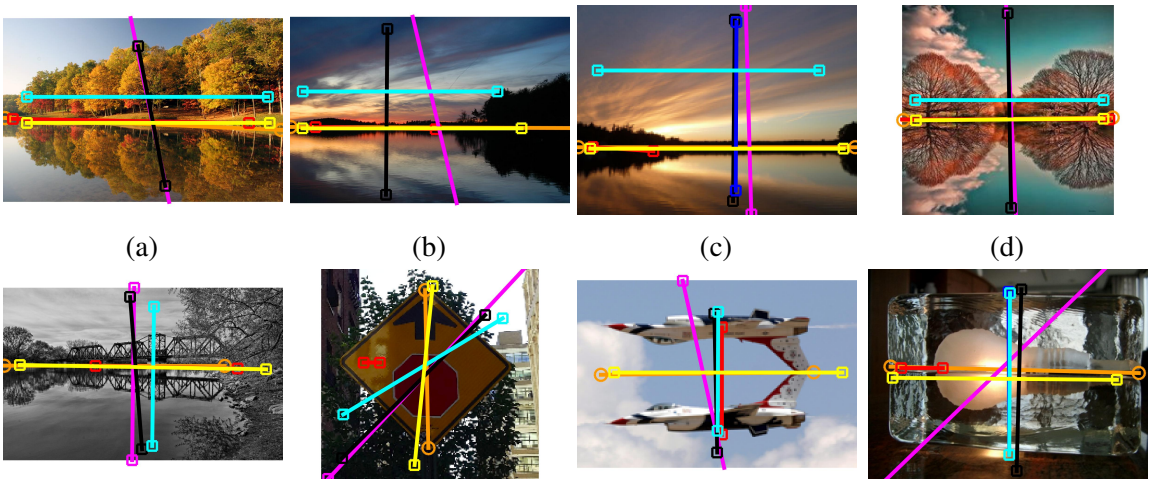

Figure 4.10 Some single-case results from PSU [134, 95], NY [27], AVA [44], and ICCV [53] datasets, with ***groundtruth (orange)***, state-of-art methods: ***Loy (red)*** [101], and ***Cic (magenta)*** [28] axes. The rest are our recent method ***LgTC-KDE (yellow)*** plus the previous proposed methods: ***GbT* (black)**, ***LgT* (blue)**, and ***LgTC* (cyan)**. Each symmetry axis is shown in a straight line with circular and squared endpoints for groundtruth and methods respectively.

Table 4.5 Using evaluation metrics **ICCV2017-Training** [53] (table 2.2), comparison of the true positive rates based on top detection for the proposed methods (especially *LgTC-MS*) against the state-of-art algorithms. Symmetry datasets are presented in multiple-case (first 3 rows), highlighted between (parenthesis) the number of images for each dataset. The last row represents sum of true positive rates among all datasets. Top 3 results are in **Bold** with **red**, **blue** and **green** colors respectively.

Datasets	*Loy* [101]	*Cic* [28]	*GbT*	*LgT*	*LgTC*	*LgTC-KDE*	*LgTC-MS*
PSUm (142)	27	10	**38**	**34**	33	**38**	**43**
NYm (63)	14	10	**23**	20	20	**21**	**20**
ICCV17m (100)	**24**	12	**26**	22	23	**26**	**28**
Total (305)	65	32	**87**	76	76	**85**	**91**

In second experiment through the statistical tables (4.4, 4.5), precision-recall curves in figure 4.11, and visual comparison in figures (4.12, 4.13), we evaluated the proposed method *LgTC-MS*, using GvM mean-shift algorithm for maximal selection in multiple symmetry case, against the previous proposed methods (*GbT*, *LgT*, *LgTC*, and *LgTC-KDE*) and state-of-art (*Loy* [101] and *Cic*[28]). For the sake of precise symmetrical comparison, all methods were assessed using restricted evaluation metrics *ICCV2017-Training* [53]. Tables (4.4,

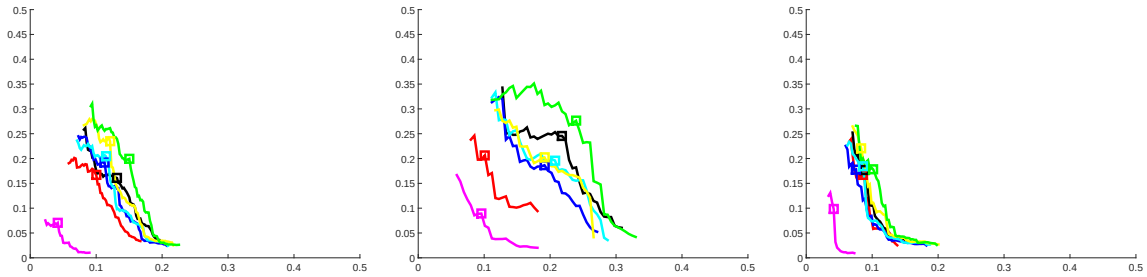

(a) PSUm (b) NYm (c) ICCV17m

Figure 4.11 Using evaluation metrics **ICCV2017-Training** [53] (table 2.2), Zoom-in version of Precision-Recall curves presented in three multiple-case symmetry (a,b,c) datasets to show the overall superior performance of our proposed methods: ***GbT* (black)**, ***LgT* (blue)**, ***LgTC* (cyan)**, ***LgTC-KDE* (yellow)**, and ***LgTC-MS* (green)**; against the prior algorithms: ***Loy* (red)** [101], and ***Cic* (magenta)** [28]. The maximum F1 scores are qualitatively presented as square symbols along the curves, and quantitatively indicated between parentheses in table 4.4. (x-axis: Recall, y-axis: Precision).

4.5) verifies that *LgTC-MS* improves detection performance of *LgTC-KDE* to find multiple symmetries, due to the weighted property of the continuous convergence scheme. Figure 4.11 proves the superior performance of *LgTC-MS* especially in *PSUm, NYm* datasets. In visual analysis of multiple symmetry results, figure 4.12 shows the effect of ranking correct candidate axes over incorrect ones while figure 4.13 presents the importance of ordering the global symmetries over the local ones, respect to the values of the normalized axis scores.

4.5 Conclusion

We proposed a supervised symmetry detection method for multiple reflection axes inside an image in a global scale, in terms of voting representation and selection. Our method is based on a weighted kernel density estimator to handle linear and directional distributions, followed by the extended version of mean-shift algorithm to identify the correct symmetry locations precisely from the incorrect ones. We evaluated the proposed work with public benchmark datasets in single and multiple cases, and using two standard evaluation metrics (normal and restricted). We concluded that the proposed work outperforms the state-of-the-art methods in selecting major symmetries inside 2D images.

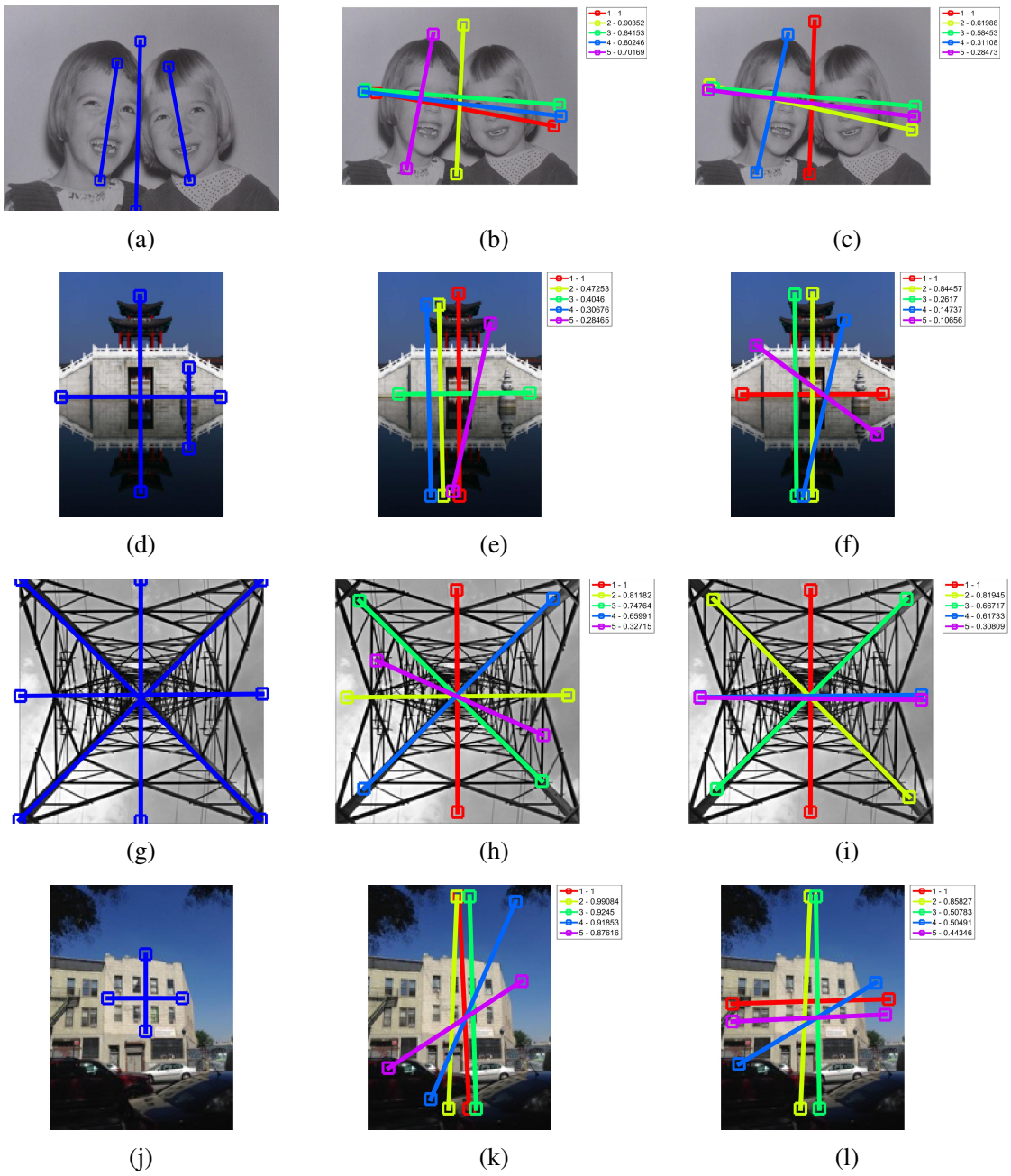

(a) (b) (c)

(d) (e) (f)

(g) (h) (i)

(j) (k) (l)

Figure 4.12 Some multiple-case results from PSUm [134, 95], and NYm [27] datasets, with ***groundtruth (blue)*** in 1st column (a-j). Thanks to continuous maximal-seeking, the proposed method ***LgTC-MS*** in 3rd column (c-l) produces higher accuracy results against ***LgTC-KDE*** in 2nd column (b-k). For each algorithm, the top five symmetry results is presented in such order: ***red***, ***yellow***, ***green***, ***blue***, and ***magenta***. Each symmetry axis is shown in a straight line with squared endpoints.

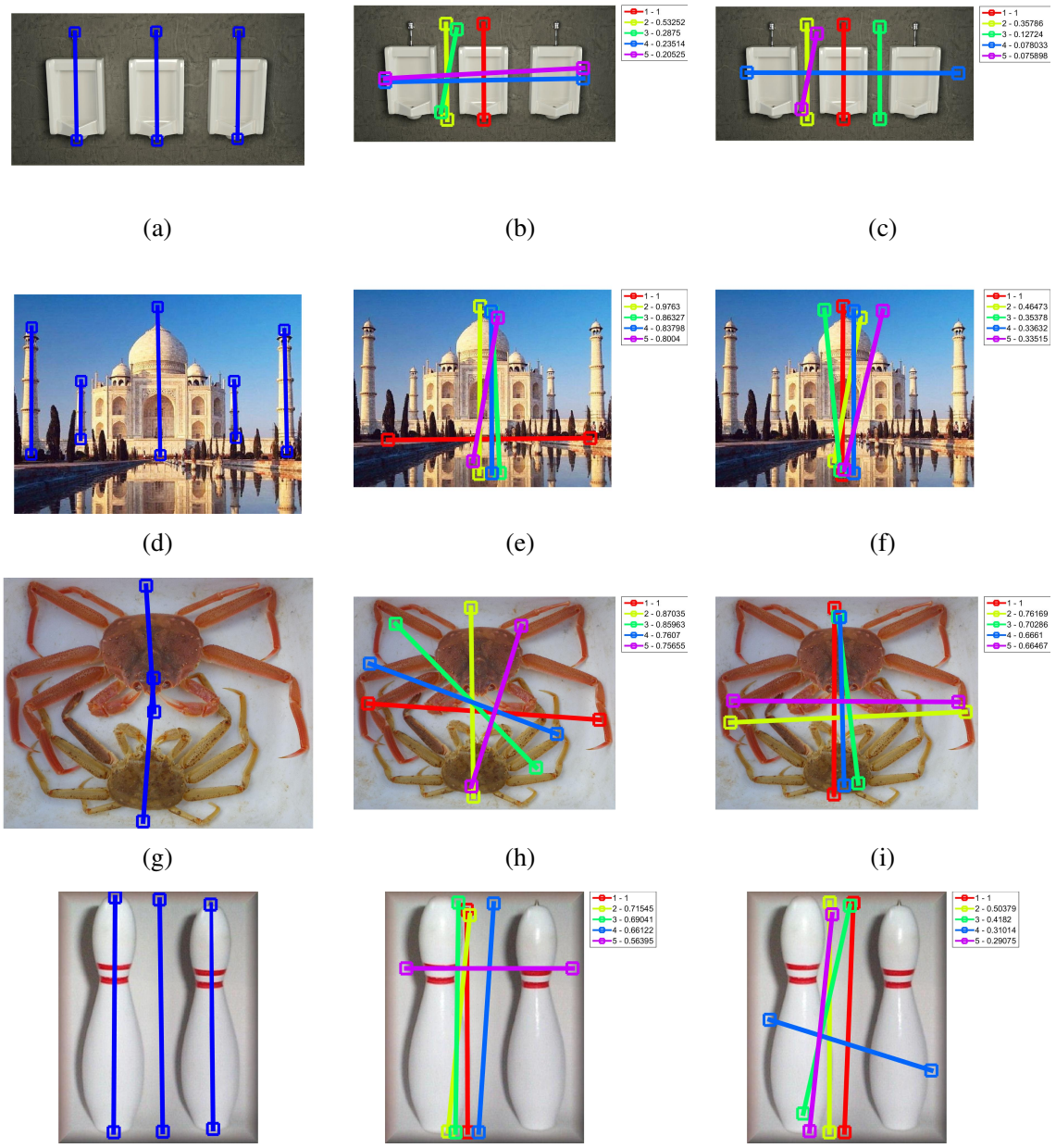

(a) (b) (c)

(d) (e) (f)

(g) (h) (i)

(j) (k) (l)

Figure 4.13 Some multiple-case results from ICCV17m [53] dataset, with ***groundtruth (blue)*** in 1st column (a-j). Thanks to continuous maximal-seeking, the proposed method ***LgTC-MS*** in 3rd column (b-k) produces better performance results against ***LgTC-KDE*** in 2nd column (c-l). For each algorithm, the top five symmetry results is presented in such order: ***red***, ***yellow***, ***green***, ***blue***, and ***magenta***. Each symmetry axis is shown in a straight line with squared endpoints.

Chapter 5

Conclusion and Future Works

This chapter presents a summary of our main contributions in reflection symmetry detection. Future perspectives are also provided to improve the limitations of the proposed framework and to discuss its possible impact in different research topics.

5.1 Main contributions

In this thesis, we focused on exploring, proposing, and evaluating the whole pipeline of reflection symmetry detection in a global scale inside synthetic and real-world images (especially in artistic photographs). The contributions of this thesis are:

— **A new feature extraction and local description based on Log-Gabor filters**: instead of using black-box SIFT scheme [101] or unreliable edge extraction using Gabor wavelets [28], we use Log-Gabor wavelets finding correct features over focused objects inside an image scene with ignoring the cluttered background. In chapter 3, Log-Gabor results a superior performance over Gabor and SIFT significantly in single symmetry datasets (especially the one used in the recent competition: ICCV17).

— **A new symmetry measure using local histogram of edge orientation and color descriptors using HSV space**: as the edge information [28] is not enough to find dual similarities between the corresponding features, we defined two local symmetrical metrics in terms of textural and color information around each features. In chapter 3, these new metrics show better symmetrical results (especially in PSU datasets for single and multiple cases) for objects of non-similar appearances or different colors.

— **A new representation space for symmetry axis voting based on kernel density estimation**: While the state-of-the-art methods [101, 28] used sparse Hough-like voting space for symmetrical representation, we proposed continuous density estimation for joint linear and periodic kernels weighted by the symmetry metrics. In chapter 4, the overall performance across all public datasets has improved in terms of single and multiple symmetrical cases.

— **A new unsupervised algorithm to select relevant axis in the previous representation space**: in literature review, a classical approach based on non-maximal suppression is used to find approximately the maxima peaks representing the symmetrical candidate axes, which lacks handling the periodic data. We defined mean-shift convergence algorithm for linear and directional data for the sake of precision peak selection. In chapter 4, the comparison study shows better results in multiple cases (especially in NYm dataset) under the highly-restricted evaluation metrics.

— **A new dataset for global symmetry evaluation in professional photographs**: unlike the previous public datasets [134, 95, 27, 53] focused on the simple scenarios of centered objects with smooth background, we proposed a challenging dataset of aesthetic photos with high-detailed environments, which can be benchmark for detecting global symmetries in such complex scenarios. In chapter 2, we provided a detailed description about the proposed dataset plus a set of symmetrical samples appendix A.

5.2 Future perspectives

Besides the advances made by the proposed work inside this thesis among the reflection symmetry detection, different research directions can be introduced in the near future. We briefly present some of these directions:

Parameter selection of KDE bandwidths: in chapter 4, we proposed to use Kernel Density Estimation to estimate the symmetry voting density. For that, we introduce a linear-directional kernel which combines a Gaussian kernel and a von Misses kernel depending respectively on a bandwidth parameter σ and a concentration parameter κ. In our experiments, these two parameters were determined empirically and there automatic estimation would be an interesting improvement. There are different ways to automatically estimate Gaussian parameter σ (Improved Sheather-Jones [15], iterative [76], smooth cross validation [21], Scott's rule of

thumb [138] and Silverman's rule of thumb [141]), and also to find a proper value for the concentration parameter κ in von-Mises distribution (Taylor [151], Kobayashi and Otsu [85], Chang-Chien et al. [23] and Garcia-Portugues [59]).

Applications of weighted linear-directional model: in chapter 4, we defined kernel density estimation and mean-shift methods for symmetry detection application only. It can be also applied to other schemes of geometrical detection algorithms: repetition of patterns and vanishing points. In the latter scheme, the baseline algorithm [149] used a simultaneous estimation of multiple models called J-Linkage, which defines a well-presented transformation between a vanishing point and an edge in closed form under Manhattan assumptions. Our work can integrate with J-Linkage algorithm through substitute the conventional Maximal Likelihood Estimator for the identification process of the edges' intersection. The state-of-the-art [90] a conventional Hough algorithm for line detection and introduced a novel alignment algorithm based on duality space between the grouped line segments and its corresponding points. Our work can improve these proposed algorithms in a continuous and periodic way.

Usage of symmetrical axes' density: in chapters (3, 4), we showed the voting score for each candidate axis in visual comparison between concurrent methods. These scores are normalized and ordered decently, but we didn't introduce a image-wise symmetry measure which highlights the connection with photography analysis and computer graphics. This work can be extended through the idea of combining a voting score and the area of the corresponding symmetry region.

Mean-shift improvements: in chapter 4, we introduced the converging algorithm using mean-shift scheme, in which it doesn't ignore the outliers cases while shifting into local maxima points. The MS convergence with noise data can be improved though Manifold Blurring mean-shift (MBMS) [159]. Plus, we can generalize the proposed mean-shift scheme to handle multi-dimensional linear-directional data, and substitute the state-of-art [71, 72] (Bregman Soft Clustering Method) for indoor scene segmentation applications.

Evaluation metrics: in chapter 2, we presented the previous competitions [134, 95, 53] in reflection symmetry detection, in which we found out that they provided insufficient explanation to compare the method's axis candidates against the ground-truth in single and multiple cases. The computer vision community expects to have open-source code for such evaluations in fair and unbiased way.

Link between symmetry and balance: in chapter 1, we defined the relationship between computer vision and art domains. Currently the researchers didn't investigate well the bridge to define a symmetry as an art principle (mainly balance), such that the definition of symmetrical categories could be investigated and well-studied for public use (i.e. museums).

Symmetry assessment through human perception metrics: based on a recent study [9], the detection methods are evaluated through different noise transformation (i.e. blurriness, brightness, additive noise, smear) and studied how these methods can preserve the symmetrical outcome in such way that the human can sense. Our work (LgTC [45]) is highlighted in this study as a strong competent among the state-of-the-art algorithms, in which opens new areas of improvements through the mains steps of the proposed detection framework (see section 3.2.1).

Appendix A

AVA Symmetry Dataset

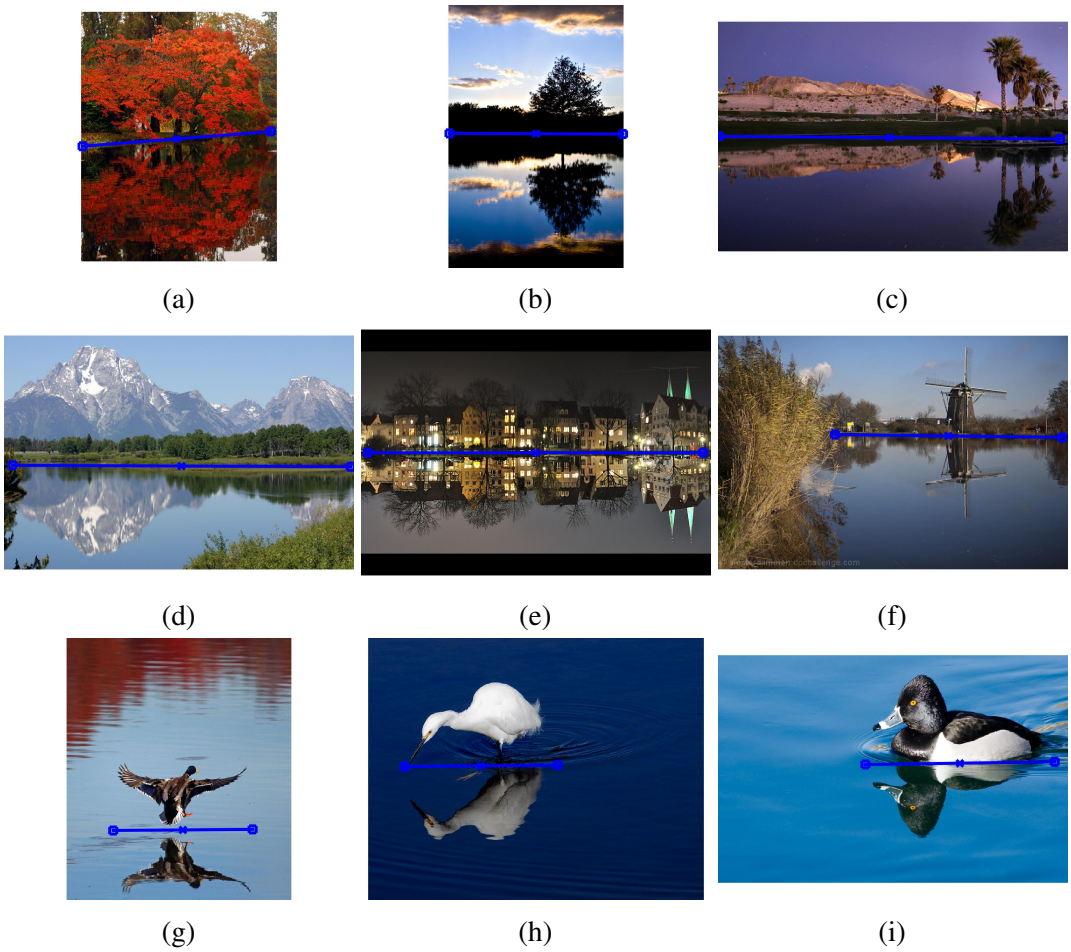

(a) (b) (c)

(d) (e) (f)

(g) (h) (i)

Figure A.1 Some examples with mirror symmetric objects.

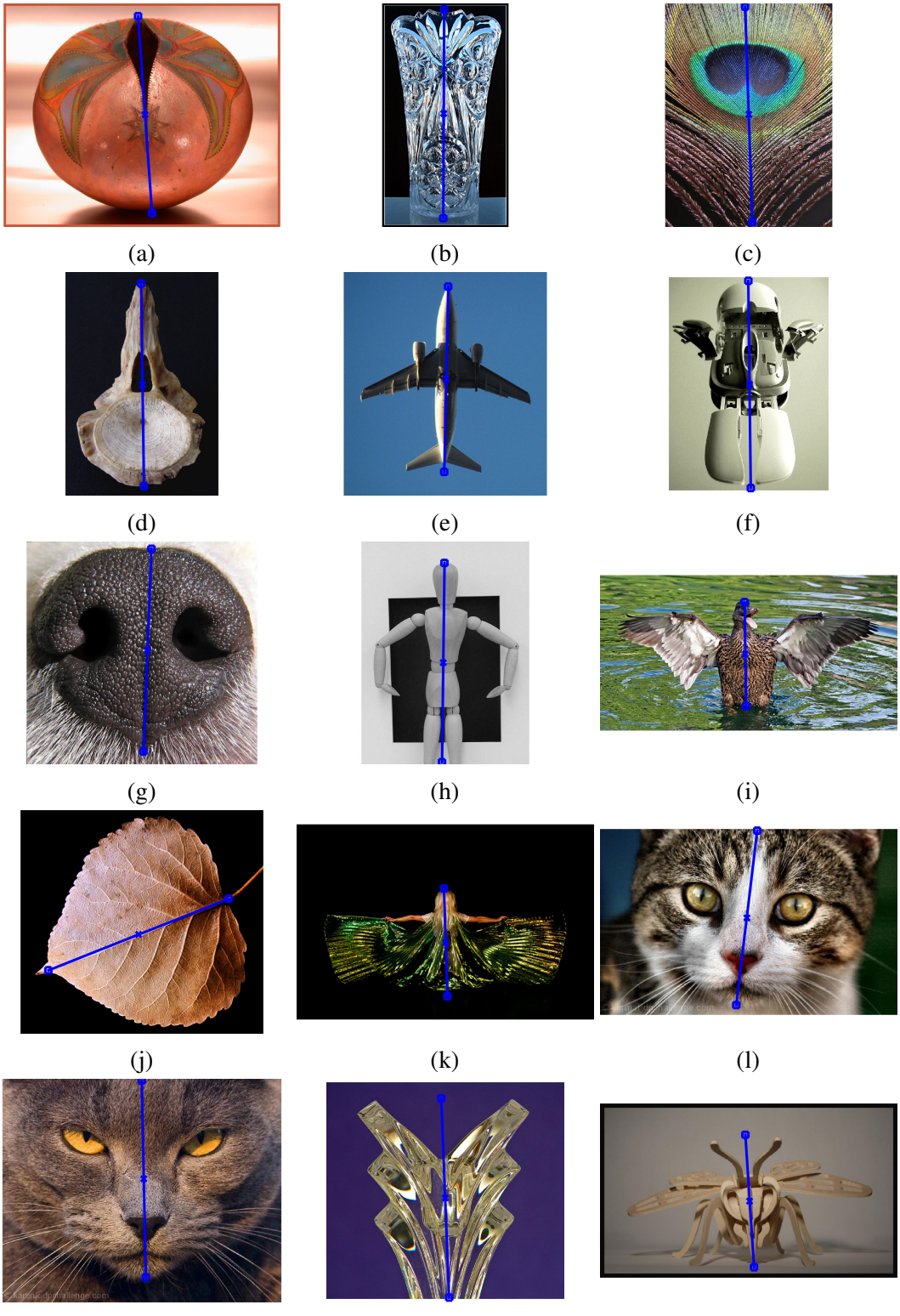

(a) (b) (c)

(d) (e) (f)

(g) (h) (i)

(j) (k) (l)

(m) (n) (o)

Figure A.2 Some examples with centric symmetric objects.

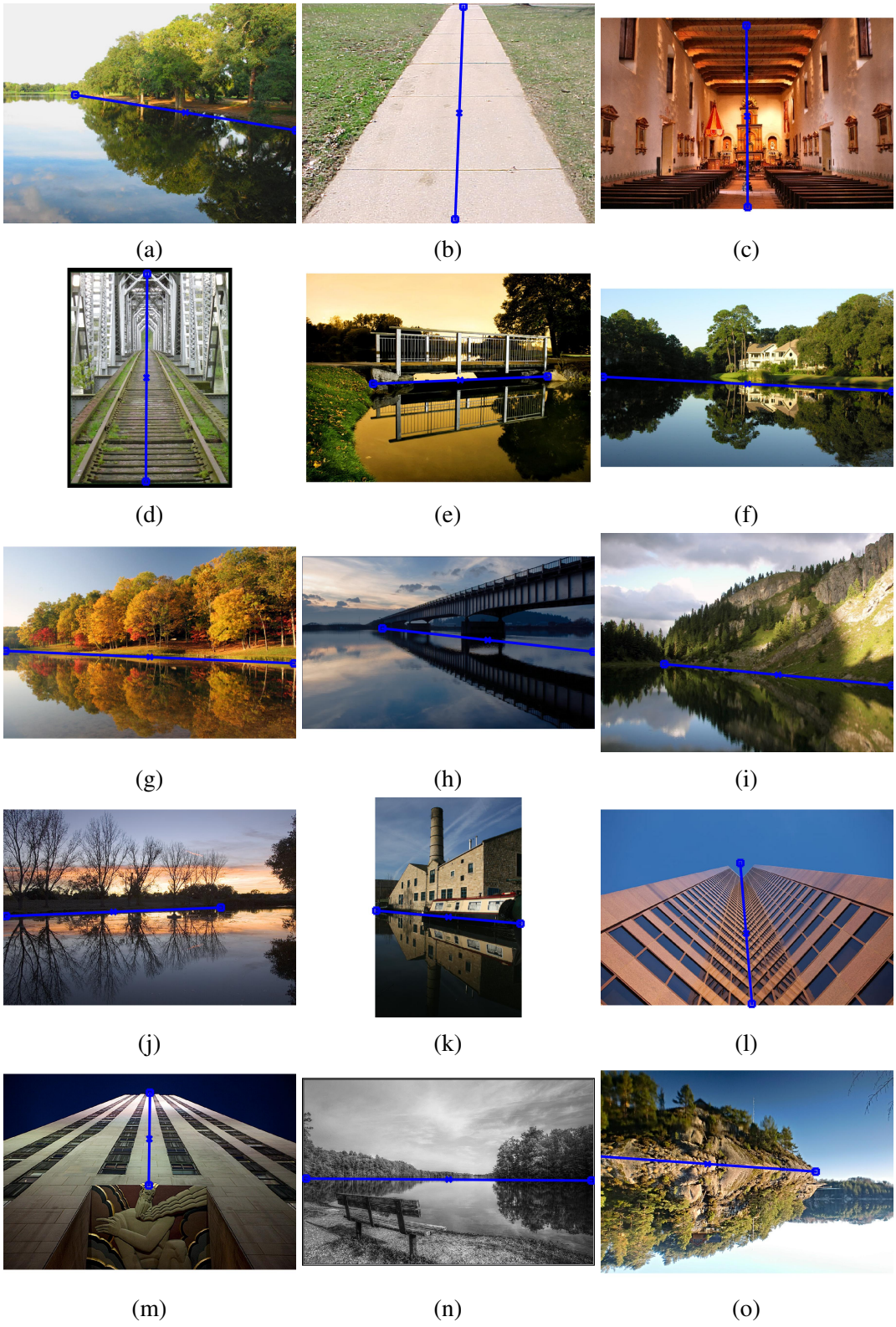

(a) (b) (c)

(d) (e) (f)

(g) (h) (i)

(j) (k) (l)

(m) (n) (o)

Figure A.3 Some examples with perspective scenes.

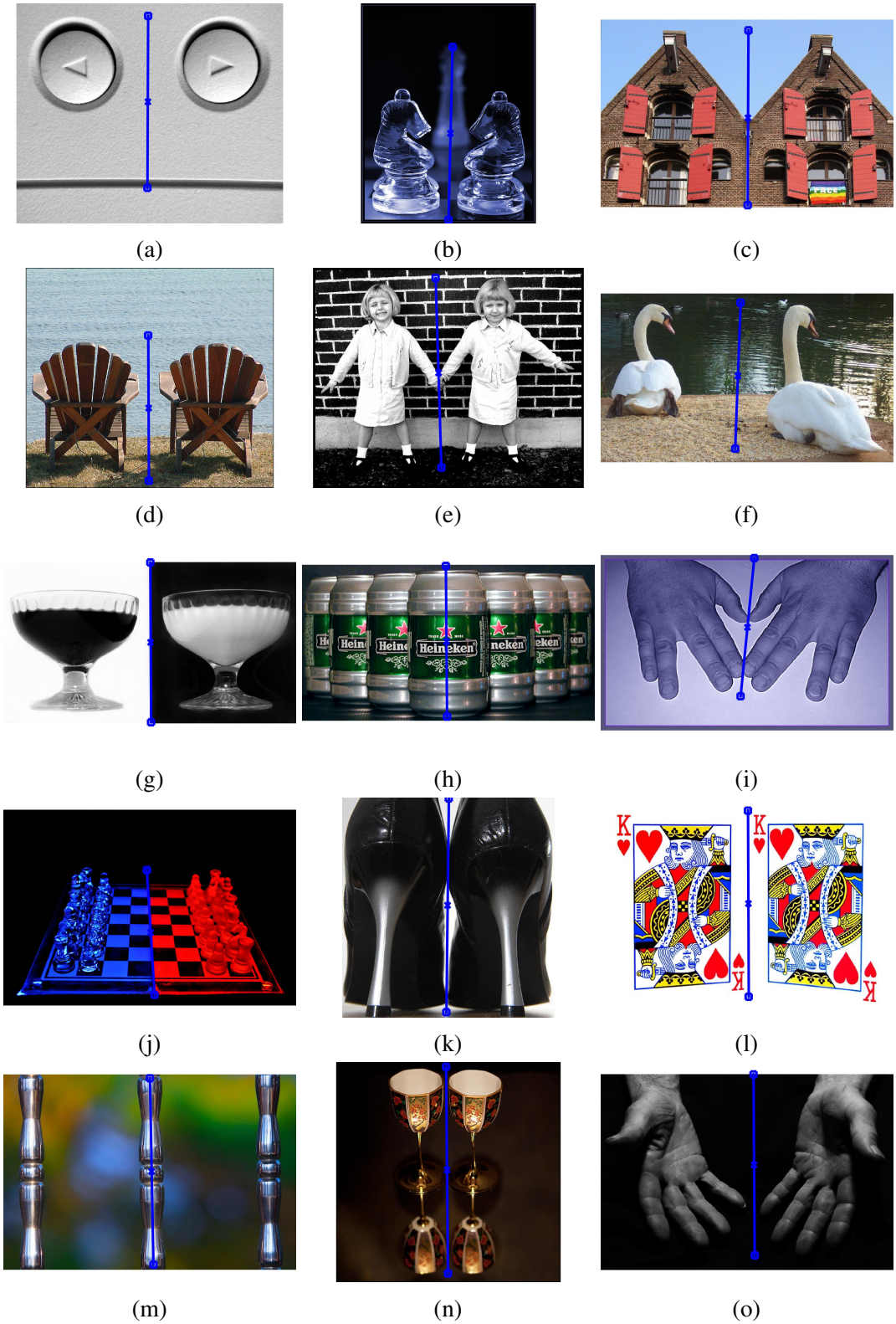

Figure A.4 Some examples with inter symmetric objects.

Appendix B

Derivation of Joint GvM Distance

B.1 Exponential families of distributions and Bregman divergence

A probability density function $f(x|\beta)$ is considered one of multivariate family of exponential in the following decomposition [71, 125, 13]:

$$f(x|\beta) = \exp\{\langle\beta, t(x)\rangle - F(\beta) + k(x)\},\ x \in \Omega_{X_s} \tag{B.1}$$

with

- **Sufficient statistics**: $t(x)$
- **Natural parameter**: β
- **Log-normalizer**: $F(\beta) = \log \int_{\Omega_{X_s}} \exp(\langle\beta, t(x)\rangle + k(x))\,\mathrm{d}x$
- **Carrier measure**: $k(.)$
- **Expectation parameter**: $\eta = \eta(\beta) = \nabla F(\beta)$

Where the log normalizer $F(\beta)$ is strictly convex and differentiable [96], and η expresses the expectation of the sufficient statistics $t(x)$. Examples of $f(x|\beta)$ can be represented among the following distributions: Gaussian, Wishart, Poisson, Rayleigh, etc.

Given a strictly convex function $F(.)$, Then the Bregman divergence $d_F(\beta_1, \beta_2)$ can be expressed on natural parameters ($\beta_1, \beta_2 \in \mathbb{N}$) [13] as follows:

$$d_F(\beta_1, \beta_2) = F(\beta_1) - F(\beta_2) - \langle\beta_1 - \beta_2, \nabla F(\beta_2)\rangle \tag{B.2}$$

where ∇F is gradient of F. The Bregman divergence describes the difference between the value of the convex function at β_1 and its first order Taylor expansion at β_2.

Let F^* be a conjugate function (Legendre dual) of F, which is strictly convex function. Bregman divergence can be expressed on expectation parameters η:

$$f(x|\eta) = \exp\{-d_{F^*}(t(x),\eta)\}\, b_{F^*}(t(x)),\ x \in \Omega_{X_s} \tag{B.3}$$

with

$$d_{F^*}(\eta_1,\eta_2) = F^*(\eta_1) - F^*(\eta_2) - \langle \eta_1 - \eta_2, \nabla F^*(\eta_2)\rangle = d_F(\beta_2,\beta_1) \tag{B.4}$$

$$F^*(\eta) = \sup_{t\in\mathscr{P}_\beta} \{\langle \eta, t\rangle - F(t)\} \tag{B.5}$$

$$b_{F^*}(t(x)) = \exp\left(F^*(t(x)) + g(x)\right) \tag{B.6}$$

where d_{F^*} is the Bregman divergence associated with F^*, and the expectation parameter is as follows: $\beta = \beta(\eta) = \nabla F^*(\eta)$.

B.2 Univariate Gaussian distribution with fixed σ

For a random value x over linear data ρ, the Gaussian distribution with bandwidth parameter σ is defined as [125]:

$$f(x|\beta) = \frac{1}{\sqrt{2\pi}\sigma} \exp -\frac{(x-\rho)^2}{2\sigma^2},\ x \in \mathbb{R} \tag{B.7}$$

— **Sufficient statistics**: $t(x) = x$
— **Natural parameter**: $\beta = \frac{\rho}{\sigma^2}$
— **Log-normalizer**: $F(\beta) = \frac{\sigma^2\beta^2 + \log\left(2\pi\sigma^2\right)}{2}$
— **Carrier measure**: $g(x) = 0$
— **Expectation parameter**: $\eta = \rho$
— **Legendre dual** of F: $F^*(\eta) = \frac{\eta^2}{2\sigma^2} + C = \frac{\rho^2}{2\sigma^2} + C$, where C is a constant.

Bregman divergence expressed on expectation parameters

— first distribution:
  — $\mathscr{N}(\rho_1,\sigma)$ and $\eta_1 = \rho_1$.
  — $F^*(\eta_1) = \frac{\rho_1^2}{2\sigma^2} + C$.
— second distribution:
  — $\mathscr{N}(\rho_2,\sigma)$ and $\eta_2 = \rho_2$.
  — $F^*(\eta_2) = \frac{\rho_2^2}{2\sigma^2} + C$.

$$d_{F^*}(\eta_1,\eta_2) = F^*(\eta_1) - F^*(\eta_2) - \langle \eta_1 - \eta_2, \nabla F^*(\eta_2)\rangle = d_F(\beta_2,\beta_1) \tag{B.8}$$

Then,

$$F^*(\eta_1) - F^*(\eta_2) = \frac{\rho_1^2}{2\sigma^2} - \frac{\rho_2^2}{2\sigma^2} \tag{B.9}$$

Given ρ_1, ρ_2 are scalars, then

$$\langle \eta_1 - \eta_2, \nabla F^*(\eta_2) \rangle = (\rho_1 - \rho_2) \frac{dF^*}{d\rho}(\rho_2) \tag{B.10}$$

As $\frac{dF^*}{d\rho}(\rho_2) = \frac{\rho_2}{\sigma^2}$

$$d_{F^*}(\rho_1, \rho_2) = \frac{\rho_1^2 - \rho_2^2}{2\sigma^2} - \frac{(\rho_1 - \rho_2)\rho_2}{\sigma^2} \tag{B.11}$$

$$= \frac{\rho_1^2 - \rho_2^2 - 2\rho_1\rho_2 + 2\rho_2^2}{2\sigma^2} \tag{B.12}$$

$$= \frac{(\rho_1 - \rho_2)^2}{2\sigma^2} \tag{B.13}$$

B.3 Von Mises distribution with fixed κ

For p-dimensional random unit vector $\mathbf{y}$ over directional data $\boldsymbol{\theta}$, the general case of Von Mises-Fisher distribution with κ concentration parameter is defined as:

$$f(\mathbf{y}|\beta) = A(\kappa) \exp(\kappa \mathbf{y}^T \boldsymbol{\theta}), \mathbf{y} \in \mathbf{R}^p, ||\mathbf{y}||_2 = 1 \tag{B.14}$$

where $\boldsymbol{\theta}$ is the mean direction as a unit vector: $||\boldsymbol{\theta}||_2 = 1$.

The values of the normalization constant $A(\kappa)$ are computed respect to the number of dimension p:

— **Von Mises distribution** for $p = 2$: $A(\kappa) = \frac{1}{2\pi B(0,\kappa)}$ and $\mathbf{y}^T \boldsymbol{\theta} = \cos(y - \theta)$. such that y and θ are the angles associated to unit vectors $\mathbf{y}$ and $\boldsymbol{\theta}$ respectively.

— $p = 3$: $A(\kappa) = \frac{\kappa}{4\pi \sinh \kappa}$ using polar coordinates, $A(\kappa) = \frac{\kappa}{\sinh \kappa}$ otherwise.

— $p > 3$: $A(\kappa) = \frac{\kappa^{p/2-1}}{(2\pi)^{p/2} B(p/2-1,\kappa)}$

where $B(p,x)$ is the modified Bessel function of the first kind at order p.

Then, the elements of Von Mises distribution are defined as:

— **Sufficient statistics**: $t(x) = y$

— **Natural parameter**: $\beta = \kappa\boldsymbol{\theta} = \nabla_\eta F^*(\eta)$ and thus $\kappa = \|\beta\|_2$ as $||\boldsymbol{\theta}||_2 = 1$

— **Log-normalizer**: $F(\beta) = -\log A(\kappa)$

— **Carrier measure**: $g(x) = 0$

— **Expectation parameter**: $\eta = \nabla_\beta F(\beta)$

— **Legendre dual** of F [72]: $F^*(\eta) = \kappa \|\eta\|_2 + \log A(\kappa)$

We derive the expectation parameter η with respect to β:

$$\begin{aligned}
\eta &= \nabla_\beta F(\beta) && \text{(B.15)}\\
&= -\nabla_\beta \left(\log A(\kappa)\right) && \text{(B.16)}\\
&= -\frac{d\log A}{d\kappa}(\kappa)\nabla_\beta \kappa && \text{(B.17)}\\
&= -\frac{A'(\kappa)}{A(\kappa)} \times \frac{\beta}{\|\beta\|_2} && \text{(B.18)}\\
&= -\frac{A'(\kappa)}{A(\kappa)} \times \frac{\beta}{\kappa} && \text{(B.19)}\\
&= \|\eta\|_2 \boldsymbol{\theta} && \text{(B.20)}
\end{aligned}$$

In Von Mises distribution, we derive the first derivative of $A(\kappa)$:

$$\begin{aligned}
A(\kappa) &= \frac{1}{2\pi B(0,\kappa)}\\
A'(\kappa) &= -\frac{B'(0,\kappa)}{2\pi B(0,\kappa)^2}\\
\frac{A'(\kappa)}{A(\kappa)} &= -\frac{B'(0,\kappa)}{B(0,\kappa)}
\end{aligned}$$

Bregman divergence expressed on expectation parameters with $p = 2$ and κ fixed

— first distribution: $\mathscr{VM}(\boldsymbol{\theta}_1, \kappa)$ with $\|\boldsymbol{\theta}_1\|_2 = 1$ and $\boldsymbol{\theta}_1$ is associated with $\theta_1 \in [0, 2\pi[$.

— second distribution: $\mathscr{VM}(\boldsymbol{\theta}_2, \kappa)$ with $\|\boldsymbol{\theta}_2\|_2 = 1$ and $\boldsymbol{\theta}_2$ is associated with $\theta_2 \in [0, 2\pi[$.

If κ fixed, $\|\eta_1\|_2 = \|\eta_2\|_2 = \frac{B'(0,\kappa)}{B(0,\kappa)}$.

$$\begin{aligned}
d_{F^*}(\eta_1, \eta_2) &= F^*(\eta_1) - F^*(\eta_2) - \langle \eta_1 - \eta_2, \nabla F^*(\eta_2)\rangle && \text{(B.21)}\\
&= \kappa(\|\eta_1\|_2 - \|\eta_2\|_2) - \langle \|\eta_1\|_2 \boldsymbol{\theta}_1 - \|\eta_2\|_2 \boldsymbol{\theta}_2, \kappa\boldsymbol{\theta}_2\rangle && \text{(B.22)}\\
&= -\kappa \frac{B'(0,\kappa)}{B(0,\kappa)} \left(\langle \boldsymbol{\theta}_1, \boldsymbol{\theta}_2\rangle - \|\boldsymbol{\theta}_2\|_2\right) && \text{(B.23)}\\
&= \kappa \frac{B'(0,\kappa)}{B(0,\kappa)} \left(1 - \langle \boldsymbol{\theta}_1, \boldsymbol{\theta}_2\rangle\right) && \text{(B.24)}\\
&= \kappa \frac{B'(0,\kappa)}{B(0,\kappa)} \left(1 - \cos(\theta_1 - \theta_2)\right) && \text{(B.25)}
\end{aligned}$$

B.4 Mixture of Gaussian and Von Mises distributions with fixed σ, κ

Based on independence assumption, Bregman divergence can combine two distributions, representing different types of samples:

$$f(x,\mathbf{y}|\beta) = f(x|\beta_\rho)\, f(\mathbf{y}|\beta_\theta) \tag{B.26}$$

$$f(x,\mathbf{y}|\eta) = \exp\{-(d_{F^*}(t(x),\eta_\rho) + d_{F^*}(t(\mathbf{y}),\eta_\theta))\}\; b_{F^*}(t(x))\; b_{F^*}(t(\mathbf{y})) \tag{B.27}$$

Bregman divergence expressed on expectation parameters with $p = 2$ and σ, κ fixed
The global Bregman divergence is obtained with the sum of the Bregman divergences. Then, for two distributions defined by $\eta_1 = (\rho_1, \theta_1)$ and $\eta_2 = (\rho_2, \theta_2)$, we can write the following:

$$d_{F^*}(\eta_1,\eta_2) = d_{F^*}((\rho_1,\theta_1),(\rho_2,\theta_2)) \tag{B.28}$$

$$= \frac{(\rho_1-\rho_2)^2}{2\sigma^2} + \kappa\frac{B'(0,\kappa)}{B(0,\kappa)}(1-\cos(\theta_1-\theta_2)) \tag{B.29}$$

During mean-shift algorithm, a point coordinate (ρ,θ) will be considered as a distribution, and the distance between two points will be computed with the Bregman divergence.

Bibliography

[1] Achanta, R., Shaji, A., Smith, K., Lucchi, A., Fua, P., and Süsstrunk, S. (2012). Slic superpixels compared to state-of-the-art superpixel methods. *IEEE transactions on pattern analysis and machine intelligence*, 34(11):2274–2282.

[2] Agrawal, A., Premachandran, V., and Kakarala, R. (2013). Rating image aesthetics using a crowd sourcing approach. In *Pacific-Rim Symposium on Image and Video Technology*, pages 24–32. Springer.

[3] Ahmed, N. U., Cvetkovic, S., Siddiqi, E. H., Nikiforov, A., and Nikiforov, I. (2017). Combining iris and periocular biometric for matching visible spectrum eye images. *Pattern Recognition Letters*, 91:11–16.

[4] Akaike, H. (1954). An approximation to the density function. *Annals of the Institute of Statistical Mathematics*, 6(2):127–132.

[5] Arbelaez, P., Maire, M., Fowlkes, C., and Malik, J. (2011). Contour detection and hierarchical image segmentation. *IEEE transactions on pattern analysis and machine intelligence*, 33(5):898–916.

[6] Arróspide, J. and Salgado, L. (2013). Log-gabor filters for image-based vehicle verification. *IEEE Transactions on Image Processing*, 22(6):2286–2295.

[7] Atadjanov, I. and Lee, S. (2015). Bilateral symmetry detection based on scale invariant structure feature. In *Image Processing (ICIP), 2015 IEEE International Conference on*, pages 3447–3451. IEEE.

[8] Atadjanov, I. R. and Lee, S. (2016). Reflection symmetry detection via appearance of structure descriptor. In *European Conference on Computer Vision*, pages 3–18. Springer.

[9] Atadjanov, I. R. and Lee, S. (2018). Robustness of reflection symmetry detection methods on visual stresses in human perception perspective. *IEEE Access*.

[10] Atallah, M. J. (1985). On symmetry detection. *Computers, IEEE Transactions on*, 100(7):663–666.

[11] Babenko, B., Dollár, P., Tu, Z., and Belongie, S. (2008). Simultaneous learning and alignment: Multi-instance and multi-pose learning. In *Workshop on Faces in'Real-Life'Images: Detection, Alignment, and Recognition*.

[12] Bandera, A., Pérez-Lorenzo, J. M., Bandera, J. P., and Sandoval, F. (2006). Mean shift based clustering of hough domain for fast line segment detection. *Pattern Recognition Letters*, 27(6):578–586.

[13] Banerjee, A., Merugu, S., Dhillon, I. S., and Ghosh, J. (2005). Clustering with bregman divergences. *Journal of machine learning research*, 6(Oct):1705–1749.

[14] Barnes, C., Shechtman, E., Finkelstein, A., and Goldman, D. B. (2009). Patchmatch: A randomized correspondence algorithm for structural image editing. *ACM Transactions on Graphics-TOG*, 28(3):24.

[15] Botev, Z. I., Grotowski, J. F., Kroese, D. P., et al. (2010). Kernel density estimation via diffusion. *The annals of Statistics*, 38(5):2916–2957.

[16] Bradley, P. S. and Mangasarian, O. L. (2000). K-plane clustering. *Journal of Global Optimization*, 16(1):23–32.

[17] Cai, D., Li, P., Su, F., and Zhao, Z. (2014). An adaptive symmetry detection algorithm based on local features. In *Visual Communications and Image Processing Conference, 2014 IEEE*, pages 478–481. IEEE.

[18] Canny, J. (1986). A computational approach to edge detection. *IEEE Transactions on pattern analysis and machine intelligence*, (6):679–698.

[19] Carreira-Perpinan, M. A. (2006). Acceleration strategies for gaussian mean-shift image segmentation. In *Computer vision and pattern recognition, 2006 IEEE Computer Society Conference on*, volume 1, pages 1160–1167. IEEE.

[20] Cerosaletti, C. D. and Loui, A. C. (2009). Measuring the perceived aesthetic quality of photographic images. In *Quality of Multimedia Experience, 2009. QoMEx 2009. International Workshop on*, pages 47–52. IEEE.

[21] Chacón, J. E. and Duong, T. (2012). Bandwidth selection for multivariate density derivative estimation, with applications to clustering and bump hunting. Technical report.

[22] Chang-Chien, S.-J., Hung, W.-L., and Yang, M.-S. (2012). On mean shift-based clustering for circular data. *Soft Computing*, 16(6):1043–1060.

[23] Chang-Chien, S.-J., Yang, M.-S., and Hung, W.-L. (2010). Mean shift-based clustering for directional data. In *Advanced Computational Intelligence (IWACI), 2010 Third International Workshop on*, pages 367–372. IEEE.

[24] Chen, L.-C., Yang, Y., Wang, J., Xu, W., and Yuille, A. L. (2016). Attention to scale: Scale-aware semantic image segmentation. In *Proceedings of the IEEE conference on computer vision and pattern recognition*, pages 3640–3649.

[25] Cheng, Y. (1995). Mean shift, mode seeking, and clustering. *IEEE transactions on pattern analysis and machine intelligence*, 17(8):790–799.

[26] Cho, M. and Lee, K. M. (2009). Bilateral symmetry detection via symmetry-growing. In *BMVC*, pages 1–11. Citeseer.

[27] Cicconet, M., Birodkar, V., Lund, M., Werman, M., and Geiger, D. (2017a). A convolutional approach to reflection symmetry. *Pattern Recognition Letters*.

[28] Cicconet, M., Geiger, D., Gunsalus, K. C., and Werman, M. (2014). Mirror symmetry histograms for capturing geometric properties in images. In *Computer Vision and Pattern Recognition (CVPR), 2014 IEEE Conference on*, pages 2981–2986. IEEE.

[29] Cicconet, M., Hildebrand, D. G., and Elliott, H. (2016). Finding mirror symmetry via registration. *arXiv preprint arXiv.1611.05971*.

[30] Cicconet, M., Hildebrand, D. G., and Elliott, H. (2017b). Finding mirror symmetry via registration and optimal symmetric pairwise assignment of curves. In *Proceedings, ICCV Workshop on Detecting Symmetry in the Wild, Venice*, volume 3, page 8.

[31] Cicconet, M., Hildebrand, D. G. C., and Elliott, H. (2017c). Finding mirror symmetry via registration and optimal symmetric pairwise assignment of curves: Algorithm and results. In *The IEEE International Conference on Computer Vision (ICCV)*.

[32] Cohen, E. and Zaidi, Q. (2007). Salience of mirror symmetry in natural patterns. *Journal of Vision*, 7(9):970–970.

[33] Collins, R. T. (2003). Mean-shift blob tracking through scale space. In *Computer Vision and Pattern Recognition, 2003. Proceedings. 2003 IEEE Computer Society Conference on*, volume 2, pages II–234. IEEE.

[34] Comaniciu, D. and Meer, P. (2002). Mean shift: A robust approach toward feature space analysis. *IEEE Transactions on pattern analysis and machine intelligence*, 24(5):603–619.

[35] Comaniciu, D., Ramesh, V., and Meer, P. (2000). Real-time tracking of non-rigid objects using mean shift. In *Computer Vision and Pattern Recognition, 2000. Proceedings. IEEE Conference on*, volume 2, pages 142–149. IEEE.

[36] Cremers, D., Osher, S. J., and Soatto, S. (2006). Kernel density estimation and intrinsic alignment for shape priors in level set segmentation. *International journal of computer vision*, 69(3):335–351.

[37] Dalal, N. and Triggs, B. (2005). Histograms of oriented gradients for human detection. In *Computer Vision and Pattern Recognition, 2005. CVPR 2005. IEEE Computer Society Conference on*, volume 1, pages 886–893. IEEE.

[38] Derpanis, K. G. (2005). Mean shift clustering. *Lecture Notes*.

[39] Dollár, P. and Zitnick, C. L. (2015). Fast edge detection using structured forests. *IEEE transactions on pattern analysis and machine intelligence*, 37(8):1558–1570.

[40] Dong, Z. and Tian, X. (2014). Effective and efficient photo quality assessment. In *Systems, Man and Cybernetics (SMC), 2014 IEEE International Conference on*, pages 2859–2864. IEEE.

[41] Dong, Z. and Tian, X. (2015). Multi-level photo quality assessment with multi-view features. *Neurocomputing*, 168:308–319.

[42] Dulai, A. and Stathaki, T. (2012). Mean shift tracking through scale and occlusion. *IET signal processing*, 6(5):534–540.

[43] Elawady, M., Alata, O., Ducottet, C., Barat, C., and Colantoni, P. (2017a). Multiple reflection symmetry detection via linear-directional kernel density estimation. In *International Conference on Computer Analysis of Images and Patterns*, pages 344–355. Springer.

[44] Elawady, M., Barat, C., Ducottet, C., and Colantoni, P. (2016). Global bilateral symmetry detection using multiscale mirror histograms. In *International Conference on Advanced Concepts for Intelligent Vision Systems*, pages 14–24. Springer.

[45] Elawady, M., Ducottet, C., Alata, O., Barat, C., and Colantoni, P. (2017b). Wavelet-based reflection symmetry detection via textural and color histograms. In *Proceedings, ICCV Workshop on Detecting Symmetry in the Wild*.

[46] Elawady, M., Ducottet, C., Alata, O., Barat, C., and Colantoni, P. (2017c). Wavelet-based reflection symmetry detection via textural and color histograms: Algorithm and results. In *The IEEE International Conference on Computer Vision (ICCV)*.

[47] Elgammal, A., Duraiswami, R., Harwood, D., and Davis, L. S. (2002). Background and foreground modeling using nonparametric kernel density estimation for visual surveillance. *Proceedings of the IEEE*, 90(7):1151–1163.

[48] Fashing, M. and Tomasi, C. (2005). Mean shift is a bound optimization. *IEEE Transactions on Pattern Analysis and Machine Intelligence*, 27(3):471–474.

[49] Field, D. J. (1987). Relations between the statistics of natural images and the response properties of cortical cells. *Josa a*, 4(12):2379–2394.

[50] Fischler, M. A. and Bolles, R. C. (1987). Random sample consensus: a paradigm for model fitting with applications to image analysis and automated cartography. In *Readings in computer vision*, pages 726–740. Elsevier.

[51] Freeman, M. (2010). The photographer's mind: Creative thinking for better digital photos.

[52] Fukunaga, K. and Hostetler, L. (1975). The estimation of the gradient of a density function, with applications in pattern recognition. *IEEE Transactions on information theory*, 21(1):32–40.

[53] Funk, C., Lee, S., Oswald, M. R., Tsogkas, S., Shen, W., Cohen, A., Dickinson, S., and Liu, Y. (2017). 2017 iccv challenge: Detecting symmetry in the wild. In *The IEEE International Conference on Computer Vision (ICCV)*.

[54] Funk, C. and Liu, Y. (2017). Beyond planar symmetry: Modeling human perception of reflection and rotation symmetries in the wild. *arXiv preprint arXiv:1704.03568*.

[55] Gabor, D. (1946). Theory of communication. part 1: The analysis of information. *Journal of the Institution of Electrical Engineers-Part III: Radio and Communication Engineering*, 93(26):429–441.

[56] Gao, F., Tao, D., Gao, X., and Li, X. (2015). Learning to rank for blind image quality assessment. *IEEE transactions on neural networks and learning systems*, 26(10):2275–2290.

[57] Gao, X., Sattar, F., and Venkateswarlu, R. (2007). Multiscale corner detection of gray level images based on log-gabor wavelet transform. *IEEE Transactions on Circuits and Systems for Video Technology*, 17(7):868–875.

[58] García-Portugués, E., Crujeiras, R. M., and González-Manteiga, W. (2013a). Kernel density estimation for directional–linear data. *Journal of Multivariate Analysis*, 121:152–175.

[59] García-Portugués, E. et al. (2013b). Exact risk improvement of bandwidth selectors for kernel density estimation with directional data. *Electronic Journal of Statistics*, 7:1655–1685.

[60] Georgescu, B., Shimshoni, I., and Meer, P. (2003). Mean shift based clustering in high dimensions: A texture classification example. In *ICCV*, volume 3, page 456.

[61] Gnutti, A., Guerrini, F., and Leonardi, R. (2017a). A normalized mirrored correlation measure for data symmetry detection. *Proceedings of the 25th European Signal Processing Conference (EUSIPCO)*, page 5.

[62] Gnutti, A., Guerrini, F., and Leonardi, R. (2017b). On reflection symmetry in natural images. In *Proceedings of the 15th International Workshop on Content-Based Multimedia Indexing*, page 29. ACM.

[63] Gong, Y., Wang, Q., Yang, C., Gao, Y., and Li, C. (2009). Symmetry detection for multi-object using local polar coordinate. In *Computer Analysis of Images and Patterns*, pages 277–284. Springer.

[64] Gong, Y., Yang, C., Wang, Q., and Gao, Y. (2008). A novel symmetry detection method for images and its application for motion deblurring. In *MultiMedia and Information Technology, 2008. MMIT'08. International Conference on*, pages 334–337. IEEE.

[65] Grigorescu, C., Petkov, N., and Westenberg, M. A. (2003). Contour detection based on nonclassical receptive field inhibition. *IEEE Transactions on Image Processing*, 12(7):729–739.

[66] Guerrini, F., Gnutti, A., and Leonardi, R. (2017a). Image symmetries: The right balance between evenness and perception. In *Systems, Signals and Image Processing (IWSSIP), 2017 International Conference on*, pages 1–5. IEEE.

[67] Guerrini, F., Gnutti, A., and Leonardi, R. (2017b). Innerspec: Technical report. In *The IEEE International Conference on Computer Vision (ICCV)*.

[68] Guo, X. and Cao, X. (2012). Mift: A framework for feature descriptors to be mirror reflection invariant. *Image and Vision Computing*, 30(8):546–556.

[69] Hager, G. D., Dewan, M., and Stewart, C. V. (2004). Multiple kernel tracking with ssd. In *Computer Vision and Pattern Recognition, 2004. CVPR 2004. Proceedings of the 2004 IEEE Computer Society Conference on*, volume 1, pages I–I. IEEE.

[70] Hall, P., Watson, G., and Cabrera, J. (1987). Kernel density estimation with spherical data. *Biometrika*, 74(4):751–762.

[71] Hasnat, M. A. (2014). *Unsupervised 3D image clustering and extension to joint color and depth segmentation*. PhD thesis, Université Jean Monnet-Saint-Etienne.

[72] Hasnat, M. A., Alata, O., and Tremeau, A. (2016). Joint color-spatial-directional clustering and region merging (jcsd-rm) for unsupervised rgb-d image segmentation. *IEEE transactions on pattern analysis and machine intelligence*, 38(11):2255–2268.

[73] Hauagge, D. C. and Snavely, N. (2012). Image matching using local symmetry features. In *Computer Vision and Pattern Recognition (CVPR), 2012 IEEE Conference on*, pages 206–213. IEEE.

[74] Heitger, F., von der Heydt, R., Peterhans, E., Rosenthaler, L., and Kübler, O. (1998). Simulation of neural contour mechanisms: representing anomalous contours. *Image and Vision Computing*, 16(6-7):407–421.

[75] Hobbs, J. A., Salome, R., and Vieth, K. (1995). *The visual experience*. Davis Publications.

[76] Horová, I., Koláček, J., and Vopatová, K. (2013). Full bandwidth matrix selectors for gradient kernel density estimate. *Computational Statistics & Data Analysis*, 57(1):364–376.

[77] Jahanian, A., Vishwanathan, S., and Allebach, J. P. (2015). Learning visual balance from large-scale datasets of aesthetically highly rated images. In *Human Vision and Electronic Imaging*, page 93940Y.

[78] Jesorsky, O., Kirchberg, K. J., and Frischholz, R. W. (2001). Robust face detection using the hausdorff distance. In *International conference on audio-and video-based biometric person authentication*, pages 90–95. Springer.

[79] Jiang, W., Lam, K.-M., and Shen, T.-Z. (2009). Efficient edge detection using simplified gabor wavelets. *IEEE Transactions on Systems, Man, and Cybernetics, Part B (Cybernetics)*, 39(4):1036–1047.

[80] Kaftan, J. N., Bell, A. A., and Aach, T. (2008). Mean shift segmentation-evaluation of optimization techniques. In *VISAPP (1)*, pages 365–374.

[81] Kaur, H. and Khanna, P. (2017). Cancelable features using log-gabor filters for biometric authentication. *Multimedia Tools and Applications*, 76(4):4673–4694.

[82] Keller, Y. and Shkolnisky, Y. (2004). An algebraic approach to symmetry detection. In *ICPR (3)*, pages 186–189.

[83] Keller, Y. and Shkolnisky, Y. (2006). A signal processing approach to symmetry detection. *Image Processing, IEEE Transactions on*, 15(8):2198–2207.

[84] Kiryati, N. and Gofman, Y. (1998). Detecting symmetry in grey level images: The global optimization approach. *International Journal of Computer Vision*, 29(1):29–45.

[85] Kobayashi, T. and Otsu, N. (2010). Von mises-fisher mean shift for clustering on a hypersphere. In *Pattern Recognition (ICPR), 2010 20th International Conference on*, pages 2130–2133. IEEE.

[86] Kondra, S., Petrosino, A., and Iodice, S. (2013). Multi-scale kernel operators for reflection and rotation symmetry: further achievements. In *Computer Vision and Pattern Recognition Workshops (CVPRW), 2013 IEEE Conference on*, pages 217–222. IEEE.

[87] Kovesi, P. (1999). Image features from phase congruency. *Videre: Journal of computer vision research*, 1(3):1–26.

[88] Kovesi, P. (2003). Phase congruency detects corners and edges. In *The australian pattern recognition society conference: DICTA*, volume 2003.

[89] Lewis, J. P. (1995). Fast template matching. In *Vision interface*, volume 95, pages 15–19.

[90] Lezama, J., Grompone von Gioi, R., Randall, G., and Morel, J.-M. (2014). Finding vanishing points via point alignments in image primal and dual domains. In *Proceedings of the IEEE Conference on Computer Vision and Pattern Recognition*, pages 509–515.

[91] Li, E. and Li, H. (2017). Reflection invariant and symmetry detection. *arXiv preprint arXiv:1705.10768*.

[92] Li, J., Sang, N., and Gao, C. (2015). Log-gabor weber descriptor for face recognition. *Journal of Electronic Imaging*, 24(5):053014–053014.

[93] Li, W. H. and Kleeman, L. (2006). Real time object tracking using reflectional symmetry and motion. In *Intelligent Robots and Systems, 2006 IEEE/RSJ International Conference on*, pages 2798–2803. IEEE.

[94] Lin, T.-Y., Maire, M., Belongie, S., Hays, J., Perona, P., Ramanan, D., Dollár, P., and Zitnick, C. L. (2014). Microsoft coco: Common objects in context. In *European conference on computer vision*, pages 740–755. Springer.

[95] Liu, J., Slota, G., Zheng, G., Wu, Z., Park, M., Lee, S., Rauschert, I., and Liu, Y. (2013). Symmetry detection from realworld images competition 2013: Summary and results. In *Computer Vision and Pattern Recognition Workshops (CVPRW), 2013 IEEE Conference on*, pages 200–205. IEEE.

[96] Liu, M., Vemuri, B. C., Amari, S.-i., and Nielsen, F. (2012a). Shape retrieval using hierarchical total bregman soft clustering. *IEEE transactions on pattern analysis and machine intelligence*, 34(12):2407–2419.

[97] Liu, Y., Hel-Or, H., and Kaplan, C. S. (2010). *Computational symmetry in computer vision and computer graphics*. Now publishers Inc.

[98] Liu, Z., Shi, R., Shen, L., Xue, Y., Ngan, K. N., and Zhang, Z. (2012b). Unsupervised salient object segmentation based on kernel density estimation and two-phase graph cut. *IEEE Transactions on Multimedia*, 14(4):1275–1289.

[99] Lockwood, E. H. and Macmillan, R. H. (1978). *Geometric symmetry*. CUP Archive.

[100] Lowe, D. G. (2004). Distinctive image features from scale-invariant keypoints. *International journal of computer vision*, 60(2):91–110.

[101] Loy, G. and Eklundh, J.-O. (2006). Detecting symmetry and symmetric constellations of features. In *Computer Vision–ECCV 2006*, pages 508–521. Springer.

[102] Lu, P., Kuang, Z., Peng, X., and Li, R. (2014). Discovering harmony: A hierarchical colour harmony model for aesthetics assessment. In *Asian Conference on Computer Vision*, pages 452–467. Springer.

[103] Mahmood, Q., Chodorowski, A., Mehnert, A., and Persson, M. (2012). A novel bayesian approach to adaptive mean shift segmentation of brain images. In *Computer-Based Medical Systems (CBMS), 2012 25th International Symposium on*, pages 1–6. IEEE.

[104] Malu, G., Bapi, R. S., and Indurkhya, B. (2017). Learning photography aesthetics with deep cnns. *arXiv preprint arXiv:1707.03981*.

[105] Mancas-Thillou, C. and Gosselin, B. (2006). Character segmentation-by-recognition using log-gabor filters. In *Pattern Recognition, 2006. ICPR 2006. 18th International Conference on*, volume 2, pages 901–904. IEEE.

[106] Manjunath, B. S., Ohm, J.-R., Vasudevan, V. V., and Yamada, A. (2001). Color and texture descriptors. *IEEE Transactions on circuits and systems for video technology*, 11(6):703–715.

[107] Mardia, K. V. and Jupp, P. E. (2009). *Directional statistics*, volume 494. John Wiley & Sons.

[108] Marola, G. (1989). On the detection of the axes of symmetry of symmetric and almost symmetric planar images. *Pattern Analysis and Machine Intelligence, IEEE Transactions on*, 11(1):104–108.

[109] Martin, D., Fowlkes, C., Tal, D., and Malik, J. (2001). A database of human segmented natural images and its application to evaluating segmentation algorithms and measuring ecological statistics. In *Computer Vision, 2001. ICCV 2001. Proceedings. Eighth IEEE International Conference on*, volume 2, pages 416–423. IEEE.

[110] Masuda, T., Yamamoto, K., and Yamada, H. (1993). Detection of partial symmetry using correlation with rotated-reflected images. *Pattern Recognition*, 26(8):1245–1253.

[111] Matas, J., Chum, O., Urban, M., and Pajdla, T. (2004). Robust wide-baseline stereo from maximally stable extremal regions. *Image and vision computing*, 22(10):761–767.

[112] Mayer, A. and Greenspan, H. (2009). An adaptive mean-shift framework for mri brain segmentation. *IEEE Transactions on Medical Imaging*, 28(8):1238–1250.

[113] Michaelsen, E. and Arens, M. (2017). Hierarchical grouping - the gestalt assessments method. In *The IEEE International Conference on Computer Vision (ICCV)*.

[114] Michaelsen, E., Muench, D., and Arens, M. (2013). Recognition of symmetry structure by use of gestalt algebra. In *Computer Vision and Pattern Recognition Workshops (CVPRW), 2013 IEEE Conference on*, pages 206–210. IEEE.

[115] Mikolajczyk, K. and Schmid, C. (2002). An affine invariant interest point detector. In *European conference on computer vision*, pages 128–142. Springer.

[116] Ming, Y., Li, H., and He, X. (2013). Symmetry detection via contour grouping. In *Image Processing (ICIP), 2013 20th IEEE International Conference on*, pages 4259–4263. IEEE.

[117] Mittal, A. and Paragios, N. (2004). Motion-based background subtraction using adaptive kernel density estimation. In *Computer Vision and Pattern Recognition, 2004. CVPR 2004. Proceedings of the 2004 IEEE Computer Society Conference on*, volume 2, pages II–II. Ieee.

[118] Mo, Q. and Draper, B. (2011). Detecting bilateral symmetry with feature mirroring. In *CVPR 2011 Workshop on Symmetry Detection from Real World Images*.

[119] Murray, N., Marchesotti, L., and Perronnin, F. (2012). Ava: A large-scale database for aesthetic visual analysis. In *Computer Vision and Pattern Recognition (CVPR), 2012 IEEE Conference on*, pages 2408–2415. IEEE.

[120] Nagar, R. and Raman, S. (2017a). Approximate reflection symmetry in a point set: theory and algorithm with an application. *arXiv preprint arXiv:1706.08801*.

[121] Nagar, R. and Raman, S. (2017b). Reflection symmetry axes detection using multiple model fitting. *IEEE Signal Processing Letters*, 24(10):1438–1442.

[122] Nagar, R. and Raman, S. (2017c). Symmmap: Estimation of the 2-d reflection symmetry map and its applications. In *The IEEE International Conference on Computer Vision (ICCV)*.

[123] Nagar, R. and Raman, S. (2017d). Symmslic: Symmetry aware superpixel segmentation. In *Proceedings, ICCV Workshop on Detecting Symmetry in the Wild, Venice*, volume 7.

[124] Nava, R., Escalante-Ramírez, B., and Cristóbal, G. (2011). A comparison study of gabor and log-gabor wavelets for texture segmentation. In *Image and Signal Processing and Analysis (ISPA), 2011 7th International Symposium on*, pages 189–194. IEEE.

[125] Nielsen, F. and Garcia, V. (2009). Statistical exponential families: A digest with flash cards. *arXiv preprint arXiv:0911.4863*.

[126] Oppenheim, A. V. and Schafer, R. W. (1983). Digital signal processing. 1975. *Englewood Cliffs, New York*.

[127] Pardo, A., Real, E., Krishnaswamy, V., López-Higuera, J. M., Pogue, B. W., and Conde, O. M. (2017). Directional kernel density estimation for classification of breast tissue spectra. *IEEE Transactions on Medical Imaging*, 36(1):64–73.

[128] Park, M., Lee, S., Chen, P.-C., Kashyap, S., Butt, A. A., and Liu, Y. (2008). Performance evaluation of state-of-the-art discrete symmetry detection algorithms. In *Computer Vision and Pattern Recognition, 2008. CVPR 2008. IEEE Conference on*, pages 1–8. IEEE.

[129] Parzen, E. (1962). On estimation of a probability density function and mode. *The annals of mathematical statistics*, 33(3):1065–1076.

[130] Patraucean, V., von Gioi, R. G., and Ovsjanikov, M. (2013). Detection of mirror-symmetric image patches. In *Computer Vision and Pattern Recognition Workshops (CVPRW), 2013 IEEE Conference on*, pages 211–216. IEEE.

[131] Penatti, O. A., Valle, E., and Torres, R. d. S. (2012). Comparative study of global color and texture descriptors for web image retrieval. *Journal of visual communication and image representation*, 23(2):359–380.

[132] Podolak, J., Shilane, P., Golovinskiy, A., Rusinkiewicz, S., and Funkhouser, T. (2006). A planar-reflective symmetry transform for 3d shapes. *ACM Transactions on Graphics (TOG)*, 25(3):549–559.

[133] Porat, B. (1996). *A course in digital signal processing*. John Wiley & Sons, Inc.

[134] Rauschert, I., Brocklehurst, K., Kashyap, S., Liu, J., and Liu, Y. (2011). First symmetry detection competition: Summary and results. Technical report, Technical Report CSE11-012, Department of Computer Science and Engineering, The Pennsylvania State University.

[135] Redies, C. (2015). Combining universal beauty and cultural context in a unifying model of visual aesthetic experience. *Frontiers in human neuroscience*, 9.

[136] Rosenblatt, M. et al. (1956). Remarks on some nonparametric estimates of a density function. *The Annals of Mathematical Statistics*, 27(3):832–837.

[137] Schifanella, R., Redi, M., and Aiello, L. M. (2015). An image is worth more than a thousand favorites: Surfacing the hidden beauty of flickr pictures. In *ICWSM*, pages 397–406.

[138] Scott, D. W. (2015). *Multivariate density estimation: theory, practice, and visualization*. John Wiley & Sons.

[139] Seckler, M., Opwis, K., and Tuch, A. N. (2015). Linking objective design factors with subjective aesthetics: An experimental study on how structure and color of websites affect the facets of users? visual aesthetic perception. *Computers in Human Behavior*, 49:375–389.

[140] Shan, C., Tan, T., and Wei, Y. (2007). Real-time hand tracking using a mean shift embedded particle filter. *Pattern recognition*, 40(7):1958–1970.

[141] Silverman, B. W. (2018). *Density estimation for statistics and data analysis*. Routledge.

[142] Stahl, J. S. and Wang, S. (2008). Globally optimal grouping for symmetric closed boundaries by combining boundary and region information. *IEEE transactions on pattern analysis and machine intelligence*, 30(3):395–411.

[143] Sun, C. (1995). Symmetry detection using gradient information. *Pattern Recognition Letters*, 16(9):987–996.

[144] Sun, C. and Si, D. (1999). Fast reflectional symmetry detection using orientation histograms. *Real-Time Imaging*, 5(1):63–74.

[145] Sun, Y. and Bhanu, B. (2012). Reflection symmetry-integrated image segmentation. *IEEE transactions on pattern analysis and machine intelligence*, 34(9):1827–1841.

[146] Svobodova, K., Sklenicka, P., Molnarova, K., and Vojar, J. (2014). Does the composition of landscape photographs affect visual preferences? the rule of the golden section and the position of the horizon. *Journal of environmental Psychology*, 38:143–152.

[147] Tang, X., Luo, W., and Wang, X. (2013). Content-based photo quality assessment. *IEEE Transactions on Multimedia*, 15(8):1930–1943.

[148] Tao, W., Jin, H., and Zhang, Y. (2007). Color image segmentation based on mean shift and normalized cuts. *IEEE Transactions on Systems, Man, and Cybernetics, Part B (Cybernetics)*, 37(5):1382–1389.

[149] Tardif, J.-P. (2009). Non-iterative approach for fast and accurate vanishing point detection. In *Computer Vision, 2009 IEEE 12th International Conference on*, pages 1250–1257. IEEE.

[150] Tavakoli, H. R., Rahtu, E., and Heikkilä, J. (2011). Fast and efficient saliency detection using sparse sampling and kernel density estimation. In *Scandinavian Conference on Image Analysis*, pages 666–675. Springer.

[151] Taylor, C. C. (2008). Automatic bandwidth selection for circular density estimation. *Computational Statistics & Data Analysis*, 52(7):3493–3500.

[152] Tsogkas, S. and Kokkinos, I. (2012). Learning-based symmetry detection in natural images. In *Computer Vision–ECCV 2012*, pages 41–54. Springer.

[153] Tuch, A. N., Bargas-Avila, J. A., and Opwis, K. (2010). Symmetry and aesthetics in website design. *Computers in Human Behavior*, 26(6):1831–1837.

[154] Van De Sande, K., Gevers, T., and Snoek, C. (2010). Evaluating color descriptors for object and scene recognition. *IEEE transactions on pattern analysis and machine intelligence*, 32(9):1582–1596.

[155] Vuollo, V., Holmström, L., Aarnivala, H., Harila, V., Heikkinen, T., Pirttiniemi, P., and Valkama, A. M. (2016). Analyzing infant head flatness and asymmetry using kernel density estimation of directional surface data from a craniofacial 3d model. *Statistics in Medicine*, 35(26):4891–4904.

[156] Walia, E. and Verma, V. (2016). Boosting local texture descriptors with log-gabor filters response for improved image retrieval. *International Journal of Multimedia Information Retrieval*, 5(3):173–184.

[157] Wang, J., Thiesson, B., Xu, Y., and Cohen, M. (2004). Image and video segmentation by anisotropic kernel mean shift. In *European conference on computer vision*, pages 238–249. Springer.

[158] Wang, M., Hua, X.-S., Mei, T., Hong, R., Qi, G., Song, Y., and Dai, L.-R. (2009). Semi-supervised kernel density estimation for video annotation. *Computer Vision and Image Understanding*, 113(3):384–396.

[159] Wang, W. and Carreira-Perpinán, M. A. (2010). Manifold blurring mean shift algorithms for manifold denoising. In *Computer Vision and Pattern Recognition (CVPR), 2010 IEEE Conference on*, pages 1759–1766. IEEE.

[160] Wang, W., Li, J., Huang, F., and Feng, H. (2008). Design and implementation of log-gabor filter in fingerprint image enhancement. *Pattern Recognition Letters*, 29(3):301–308.

[161] Wang, Z., Tang, Z., and Zhang, X. (2015). Reflection symmetry detection using locally affine invariant edge correspondence. *Image Processing, IEEE Transactions on*, 24(4):1297–1301.

[162] Welch, E. and Kobourov, S. (2017). Measuring symmetry in drawings of graphs. In *Computer Graphics Forum*, volume 36, pages 341–351. Wiley Online Library.

[163] Widynski, N., Moevus, A., and Mignotte, M. (2014). Local symmetry detection in natural images using a particle filtering approach. *IEEE Transactions on Image Processing*, 23(12):5309–5322.

[164] Wu, K.-L. and Yang, M.-S. (2007). Mean shift-based clustering. *Pattern Recognition*, 40(11):3035–3052.

[165] Yang, M.-S., Chang-Chien, S.-J., and Kuo, H.-C. (2014). On mean shift clustering for directional data on a hypersphere. In *International Conference on Artificial Intelligence and Soft Computing*, pages 809–818. Springer.

[166] Zabrodsky, H., Peleg, S., and Avnir, D. (1992). A measure of symmetry based on shape similarity. In *IEEE Conference on Computer Vision and Pattern Recognition*, pages 703–706.

[167] Zabrodsky, H., Peleg, S., and Avnir, D. (1995). Symmetry as a continuous feature. *Pattern Analysis and Machine Intelligence, IEEE Transactions on*, 17(12):1154–1166.

[168] Zakia, R. D. and Page, D. (2012). *Photographic Composition: A Visual Guide*. Focal Press.

[169] Zhang, H., Guo, X., and Cao, X. (2010). Water reflection detection using a flip invariant shape detector. In *Pattern Recognition (ICPR), 2010 20th International Conference on*, pages 633–636. IEEE.

[170] Zhao, M., Wang, L., and Han, J. (2013). An adaptive tracking window based on mean-shift target tracking algorithm. In *Chinese Automation Congress (CAC), 2013*, pages 348–352. IEEE.

[171] Zhao, S., Gao, Y., Jiang, X., Yao, H., Chua, T.-S., and Sun, X. (2014). Exploring principles-of-art features for image emotion recognition. In *Proceedings of the ACM International Conference on Multimedia*, pages 47–56. ACM.

[172] Zhou, H., Yuan, Y., and Shi, C. (2009). Object tracking using sift features and mean shift. *Computer vision and image understanding*, 113(3):345–352.